Forschungszentrum Karlsruhe
Technik und Umwelt

Wissenschaftliche Berichte
FZKA 6379
INV-CIT(99)-P029

UO_2 Dissolution by Molten Zircaloy. New Experimental Results and Modelling

P. J. Hayward*,
P. Hofmann, J. Stuckert,
A. V. Berdyshev, M. S. Veshchunov****

Institut für Materialforschung
Projekt Nukleare Sicherheitsforschung

*Atomic Energy of Canada Limited (AECL), Pinawa

**Nuclear Safety Institute (IBRAE), Russian Academy of Sciences, Moscow

Forschungszentrum Karlsruhe GmbH, Karlsruhe
1999

UO_2-Auflösung durch geschmolzenes Zircaloy. Neue experimentelle Ergebnisse und deren Modellierung

Zusammenfassung:

Dieser Bericht faßt die Aufgabe 2.3 des europäischen Projektes „Corium Interactions and Thermochemistry“ (CIT) zusammen, die im Rahmen des 4. Rahmenprogrammes „Nuclear Fission Safety“ der EG durchgeführt wurde. Der experimentelle Teil dieser Aufgabe wurde in der Zeit von 1997 bis 1999 in den Labors von AECL in Whiteshell (Kanada) im Auftrag des Forschungszentrums Karlsruhe durchgeführt. Der analytische Teil der Aufgabe 2.3 erfolgte am Institut für nukleare Sicherheit der Russischen Akademie der Wissenschaften (IBRAE).

Die Auflösung von UO_2 durch flüssiges Zry (≥1760°C) beeinflußt viele physikalisch-chemische Prozesse während der Kernzerstörung: (i) Verflüssigung von UO_2 ungefähr 1000°C unterhalb seines Schmelzpunkts, (ii) Verlagerung von (U, Zr, O) Schmelzen nach dem Versagen der äußeren ZrO_2-Schicht auf den Zircaloy-Hüllrohren und (iii) die Spaltproduktfreisetzung.

Um die widersprüchlichen Versuchsergebnisse in der Literatur zu verstehen, und die Ungenauigkeiten in den verschiedenen Brennstoff-Auflösungsmodellen zu verringern, wurden unterschiedliche UO_2-Auflösungsexperimente durchgeführt: (i) Isotherme UO_2-Auflösungstests bei 2100 und 2200°C und Reaktionszeiten bis zu 30 Min., (ii) zusätzliche Tests bei 2200°C, in denen der Tiegelboden durch eine chemisch stabile Y_2O_3 - Scheibe isoliert wurde und (iii) erste Versuche zur simultanen Auflösung von UO_2 und ZrO_2 durch flüssiges Zircaloy.

Die wesentlichen Versuchsergebnisse sind:

- Die Auflösung von UO_2 findet in zwei Phasen statt: eine erste kurze und schnelle Auflösungsgsphase bis zur Sauerstoffsättigung der Zircaloy-Schmelze und eine zweite Phase, in der die UO_2-Auflösung langsam fortschreitet und begleitet ist von einer Ausscheidung von keramischen $(U, Zr)O_{2-x}$ – Partikeln in der sauerstoffgesättigten (U,Zr,O)-Schmelze.
- Die Hauptursache für die Diskrepanz bei den früheren Versuchsergebnissen war die Verwendung von unterschiedlich großen UO_2-Tiegeln mit verschiedenen Wandstärken, verschiedenen UO_2/Zry-Massenverhältnissen und verschiedenen Verhältnissen zwischen der Schmelzoberfläche und dem Schmelzvolumen (S/V), die alle die Sauerstoffdiffusion von der UO_2-Tiegelwand zur Zircaloy-Schmelze und damit die UO_2-Auflösung beeinflussen.
- Die ersten Experimente zur simultanen Auflösung von UO_2 und ZrO_2 durch flüssiges Zircaloy wurden zum Vergleich zu den separaten UO_2- und ZrO_2-Auflösungsexperimenten durchgeführt. Die Ergebnisse zeigen eine größere ZrO_2-Auflösungsrate und ein größeres Ausmaß an UO_2- und ZrO_2-Auflösung als von den Ergebnissen der Einzeleffektexperimente zu erwarten war. Diese Versuchsergebnisse können einen großen Einfluß auf das ZrO_2-Versagenskriterium besitzen.

Das von IBRAE entwickelte analytische Modell ist in der Lage, den scheinbaren Widerspruch in den Ergebnissen zu erklären, der in den früheren Experimenten mit kleinen UO_2-Tiegeln beobachtet wurde, und ist außerdem in der Lage, die neuen Ergebnisse der AECL/FZK-Tests mit großen Tiegeln zu beschreiben:

- Das UO_2-Auflösungmodell bestätigt, daß die wesentliche Auflösung von UO_2 sehr schnell (~250/350s) in der sogenannten 1. Phase, der Sättigungsphase, stattfindet. Es kommt zu einer Sättigung der Schmelze, die durch die Liquiduslinie bei gegebener Temperatur bestimmt wird. Das bestätigt, dass durch die Liquiduslinie die UO_2-Auflösung in Codesystemen mit einer bestimmten Genauigkeit beschrieben werden kann. Eine geringere UO_2-Auflösung findet während der sogenannten 2. Phase, der Ausscheidungsphase, statt. Diese kann jedoch unter realistischeren Bedingungen der simultanen UO_2- und ZrO_2-Auflösung erheblich verstärkt werden.
- Die ersten Experimente zur simultanen Auflösung von UO_2 und ZrO_2 zeigen eine starke Zunahme der ZrO_2-Auflösungskinetik und eine verstärkte ZrO_2-Auflösung. Die Erklärung ist eine erhöhte Konvektion in der Schmelze in Gegenwart von gelöstem UO_2. Die Zunahme der UO_2-Auflösung erfolgt durch eine verstärkte Ausscheidungsphase in Gegenwart von ZrO_2.

ABSTRACT

This report summarises the task 2.3 of the European Project on "Corium Interactions and Thermochemistry (CIT)" conducted within the 4th Framework Programme on "Nuclear Fission Safety". The experimental part of this task was performed during 1997/99 at the Whiteshell Laboratories of AECL (Canada), with AECL acting as a subcontractor to Forschungszentrums Karlsruhe. The analytical part of the task 2.3 was performed at the Nuclear Safety Institute of the Russian Academy of Sciences (IBRAE).

The dissolution of UO_2 by molten Zry (≥ 1760°C) influences many physico-chemical processes during core degradation: liquefaction of UO_2 at about 1000°C below its melting point, relocation of resulting (U, Zr, O) melts after failure of the outer ZrO_2 layer on Zircaloy cladding tubes and fission product release rates. In order to understand apparent inconsistencies in the experimental results published in the literature and to reduce uncertainties in the modelling of the fuel dissolution processes, different types of tests were carried out:

(i) isothermal UO_2 crucible dissolution tests at 2100 and 2200°C and reaction times up to 30 min., (ii) additional tests at 2200°C where the crucible-cavity bottom was isolated from the reaction by an yttria disc, and (iii) preliminary scoping tests involving the simultaneous dissolution of UO_2 and ZrO_2.

The main test results are:

- The dissolution of UO_2 takes place in two stages: a first short saturation period with a rapid dissolution of the UO_2 and a second period during which there is a slower UO_2 dissolution accompanied by precipitation of a ceramic (U, Zr)O_{2-x} phase in the oxygen-saturated melt.
- The main cause of the discrepancy amongst the previous results was connected with different UO_2 crucible sizes (wall thickness), UO_2/Zry mass ratios and melt surface to volume ratios (S/V) which influence the oxygen diffusion from crucible walls to the Zircaloy melt.
- First scoping tests on the simultaneous UO_2/ZrO_2 dissolution by molten Zry were carried out for comparison with separate UO_2 and ZrO_2 dissolution tests. They show a faster ZrO_2 dissolution rate and a larger extent of UO_2 and ZrO_2 dissolution than expected from separate dissolution tests. This could have an important bearing on the ZrO_2 failure criteria on Zircaloy cladding tubes.

The developed analytical model by IBRAE explains the disagreement observed in previous UO_2 dissolution tests with small UO_2 crucibles and reproduces correctly the new AECL/FZKA tests with large UO_2 crucibles:

- The UO_2 dissolution model confirms that most of the UO_2 liquefaction occurs rapidly (~250/350s) in the 1st saturation phase up to the oxygen saturation of the melt given by the liquidus line at a given temperature. This confirms that this liquidus line can limit with a certain accuracy the UO_2 dissolution in severe accident codes. Minor dissolution occurs during the 2nd precipitation phase, however, it can significantly increase under more realistic conditions of simultaneous UO_2 and ZrO_2 dissolution.
- First tests on the simultaneous UO_2 and ZrO_2 dissolution show a large increase of ZrO_2 dissolution rate and extent due to enhanced convective stirring of the melt in the presence of UO_2. A large increase of the UO_2 dissolution occurs due to a well pronounced precipitation stage in the presence of ZrO_2.

CONTENTS

1. Introduction

This report summarises the Task 2.3 of the Corium Interactions and Thermochemistry (CIT) programme. The experimental part of this Task was performed during 1997/9 at the Whiteshell Laboratories of AECL, with AECL acting as a subcontractor to FZKA. Funding for the AECL work was provided on a cost-shared basis by FZKA and COG. The analytical part of the Task 2.3 was performed at the Nuclear Safety Institute (IBRAE) of Russian Academy of Sciences (RAS), with IBRAE acting as a subcontractor to the FZK. Final interpretation of the experimental results were performed by FZKA, AECL and IBRAE.

The original objective of Task 2.3 was to repeat the original UO_2-dissolution tests of Hofmann et al. [1] using UO_2 crucibles containing molten Zircaloy - 4 (Zry) charges, and direct methods for chemical analysis of the melts. The intention was to reconcile the differences in previously published data and models for fuel dissolution in molten cladding. As the work progressed, however, the focus expanded to include (i) tests where the crucible-cavity bottom was isolated from the reaction by an yttria disc, and (ii) tests involving simultaneous dissolution of UO_2 and ZrO_2.

1.1. Review of the existing tests

The first molten Zry/UO_2 - crucible experiments up to 2000°C were reported by Dienst, Hofmann and Kerwin-Peck [1]. From their observations of cooled specimens from dissolution tests at 2000°C, Dienst et al. postulated that, after the short time interval required from crucible wetting, rapid crucible dissolution occurs to form a homogeneous (U,Zr,O) melt. This melt subsequently decomposes during cooling into α-Zr(O), a (U,Zr) alloy and, with higher oxygen concentrations in the melt, a ceramic (U,Zr)O_2 phase.

In subsequent work [2,3], Hofmann and co-workers performed a series of crucible dissolution tests at 100°C intervals within the temperature range 1950-2250°C, using an argon atmosphere and an outer tungsten crucible as the susceptor. They used large UO_2 crucibles (in comparison with subsequent experiments) with Zry charge, which after rapid cooling in the end of the tests were sectioned and analysed metallographically. The melts were analysed by an indirect method, by correlating the measured area fraction of the (U,Zr)O_2 phase in the melt with (U,Zr)O_2 area fraction in control samples of known chemical composition.

Based on the melt analyses and metallographic observations, Hofmann stated that up to ~30 wt.% UO_2 can be dissolved in the melt before the ceramic (U,Zr)O_2 phase is seen in the cooled specimen. He postulated that very rapid crucible dissolution during the first ~100 s at 1950 and 2050°C (the incubation, or saturation period) forms a homogeneous (U,Zr,O) melt that decomposes during cooling into α-Zr(O) and a (U,Zr) alloy. After this time (during the post-incubation, or precipitation period), continuous increase of the ceramic phase (U,Zr)O_2 portion in the refrozen melt was observed which was interpreted as increase of the melt UO_2 content. The dissolution rate at each temperature during this period calculated within the above mentioned methods (by measured correlation between the ceramic phase fraction and the melt UO_2 content), followed a parabolic time law (see Fig. 1.1). The most important confirmation of the continuation of the dissolution process during the precipitation stage were visual observations of the UO_2 crucible wall thinning at this stage detected in the post-test photographs of the samples.

Later Kim and Olander published the results of two sets of crucible-based experiments [4,5]. In the first set, the reaction between UO_2 and molten Zry was investigated at temperatures between 1900 and 2200°C using yttria-washed thoria crucibles to contain the molten Zry charge, and with a thin disk of either single-crystal or polycrystalline UO_2 covering each crucible floor. Polished sections of the post-test specimens were examined by optical microscopy, scanning electron microscopy, Auger electron spectroscopy and electron microprobe analysis. The complicated structure observed in the quenched specimens contained a two-phase region at the interface between solid and molten phases. Growth of the two-phase layer followed the parabolic rate law, as did the thickness decrease of the UO_2 disk. Average concentration distributions in the direction normal to the reacting surface revealed diffusion mass transfer in the melt.

Although these experiments provided important insights into many aspects of the UO_2/molten Zry reaction, the melts were essentially quiescent because of the absence of gravity-driven convective stirring. For this reason, Kim and Olander performed a second set of experiments to investigate convection-controlled UO_2 dissolution. These tests were performed in crucible machined from LWR fuel pellets (and for this reason with smaller dimensions in comparison with Hofmann's tests), each containing a charge of either as-received Zry or a prefabricated oxygen containing Zry (6 wt.% O) alloy. Other test details were identical to those for diffusion-controlled dissolution tests of the first series.

Kim and Olander observed that after the termination of the rapid first, saturation stage, a two-phase region appeared in the microstructure. Simultaneously with the appearance of this region, the bulk of the refrozen melt did not show anymore a (U,Zr) alloy, and chunks (precipitates) of $(U,Zr)O_{2-x}$ appeared (qualitatively the same behaviour as observed in the experiments of Hofmann et al. [1-3]). The dissolution kinetics were unambiguously characterised in Kim's thesis [5] by the parabolic time dependence of the uranium content in the liquid phase (during the second, precipitation stage) and described by an Arrhenius equation (see Fig. 1.2). However, in the paper of Kim and Olander [4] a less definite conclusion about the obtained results was deduced: the precipitation stage data in Fig. 1.2 «could be fairly well represented by straight lines» (i.e. parabolic kinetics), and they further attempted the description of the U content in the molten phase by another function of time (see below). Nevertheless, the fact of the increase of the uranium uptake by the melt at this stage was never doubted also in [4]; it was only noticed that «the rates of this uptake were considerably greater during the saturation periods than at subsequent times».

Additional confirmations of the continuation of the UO_2 dissolution during the precipitation stage were the direct measurements of the UO_2 crucible wall thinning at this stage. From figures presented in [4,5] it was clearly seen that the UO_2 wall dissolution rates during the precipitation (post-incubation) stage, being rather small at 2000°C, significantly increased at higher temperatures (2100 and 2200°C).

A serious qualitative disagreement exists between the data presented above, of the two groups and the results of Hayward and George [6,7] who observed none of the above-described phenomena after the termination of the saturation stage: a) increase of the U atom concentration in the molten zone; b) increase of the ceramic phase portion in the refrozen melt; c) reduction of the UO_2 crucible wall thickness. On this basis Hayward and George deduced a logical conclusion about the cessation of the dissolution process after saturation of the liquid phase during the first, saturation stage in their tests.

1.2. Review of the existing models

The original work of Hofmann et al. [2] led to development of the LISI numerical code [8]. This code involved an assumption that oxygen diffusion was the main parameter controlling UO_2 /molten Zry interaction and ignored the influence of melt convection on fuel dissolution in the UO_2 crucible tests.

Kim and Olander subsequently demonstrated in [4,5] that gravity-driven convection in such tests with vertical crucible walls was the controlling parameter for dissolution rates. They used the well-known analogy between heat and mass transfer to derive an expression for the mass transfer coefficient in the melt. However, in their model [4] Kim and Olander did not consider an important influence of the oxygen diffusion from the interior of the UO_2 into the melt and, for this reason, their model predicted very a slow approach of the U content in the melt to the saturation point at a late stage of the dissolution process. In order to fit this model prediction to their measurements in the second, precipitation stage (initially interpreted in [5] as continuous UO_2 dissolution obeyed parabolic time law, see Fig. 1.2), further in the paper [4] they attempted the description of the U content in the molten phase approaching saturation composition by another function of time, $\propto (1+\alpha t)^{-4}$.

For modelling of the first series of Kim and Olander tests with dissolution of UO_2 disk (without convective stirring of the melt), an O-diffusion-based theoretical model describing mass transport through the two-phase region at the UO_2/molten Zry interface was proposed by Veshchunov and Volchek [9]. Being based on the self-consistent consideration of the oxygen diffusion in the three regions (solid, liquid and two-phase zones) the model allowed description of the two-phase layer growth (as well as the thickness decrease of the UO_2 disk) followed the parabolic rate law, in fair agreement with observations [4,5].

An attempt of self-consistent consideration of the oxygen diffusion mass transport in the solid phase and convective mass transport in the liquid phase for modelling of fuel dissolution in the UO_2 crucible test series was made in the paper of Olander [10]. However, being qualitatively correct for description of initial stage of the dissolution process, the model predicted very slow approach of the melt bulk composition to the final saturation value (during ~ 10^4 s). The onset of the ceramic phase $(U,Z)O_{2-x}$ chunks after initial time period (~ 50-100 s) observed in the tests [4] was assigned to the interface disintegration during continuous approach of the melt to the final saturation composition.

Qualitatively similar behaviour (continuous approach to the saturation composition of the melt during all the dissolution process) was proposed by Hayward and George [6] who considered solid/liquid interface kinetics as a rate-controlling step, thus, neglecting mass transfer mechanisms in both the solid and liquid phases.

In the model of Veshchunov and Hofmann [11] it was demonstrated for the first time that in the crucible tests the bulk melt composition attains its saturation value during a short time interval of the first, saturation period. In the subsequent time interval (precipitation period) the continued oxygen supply to the interface by diffusion from fuel interior leads to an oversaturation of the melt, resulting in precipitation of the ceramic $(U,Zr)O_{2-x}$ phase in the melt. Simultaneously, dissolution of solid UO_2 can be continued (and can be accompanied by disintegration of the solid phase boundary with the same composition $(U,Zr)O_{2-x}$ as precipitated particles). Therefore, the oxygen diffusion in the solid UO_2 phase determines the kinetics of both processes of the UO_2 dissolution and the formation of $(U,Zr)O_{2-x}$ precipitates after completion of the saturation stage, and for this reason these kinetics have to obey a parabolic time

law ($\propto t^{1/2}$) in the precipitation stage. This allows a natural explanation of the apparent contradictions between observations of various groups since various wall thickness d_w of the crucibles in different tests lead to different diffusion times determining cessation of the dissolution process. Hence, in the tests of Hayward and George the duration of the diffusion time from the crucible walls ($\tau_{dif} \propto d_w^2/D_{ox}$) was similar to that in the tests of Kim and Olander ($\tau_{dif} \approx$ 100 - 150 s), however, the duration of the saturation stage ($\tau_{sat} \propto (S/V)^{-1}$) was larger than in the Kim and Olander's tests (owing to a smaller interface surface to melt volume ratio S/V) and practically coincided with the diffusion time τ_{dif}. For this reason, only the first, saturation stage was observed in these tests. In the tests of Hofmann et al. the crucible walls had the largest value and for this reason, the precipitation stage was the most pronounced.

The model further developed by Veshchunov and Hofmann in cooperation with Berdyshev [12] self-consistently describes various saturation melt compositions attained during the saturation stage in all the three test series (Hofmann et al., Kim and Olander, Hayward and George) (Fig. 1.3) with various oxygen contents (zero and non-zero) of the initial Zr melt (see Section 7.2.3).

For the description of the second, precipitation period a general approach was formulated in [11,12]. However, in the absence of all necessary data for the solution of the obtained complete system of equations of the general model, a simplified approach for searching for the model solution was proposed in [11]. By this approach an additional assumption about invariable composition of the forming precipitates (satisfactorily corresponding to the independent observations of Hofmann et al. and Kim and Olander) was made. This assumption allowed to avoid a complicated consideration of the mass transfer in the two-phase zone of the melt during precipitation period. As a result, the model self-consistently described (at least, qualitatively) all the observations of the different experiments [2,4,6] at different temperatures.

In the subsequent paper [13], for the explanation of the Hayward and George's data [6,7] Olander searched for another particular solution of the general model formulated in the paper [11], using different additional assumption. Namely, it was postulated that the dissolution rate is equal to zero in the precipitation period at 2000°C. However, this solution was valid only for the partial description of the particular case of the dissolution process at 2000°C in the tests [4], being in direct contradiction with observations either of Hofmann or of Kim and Olander at higher temperatures 2100-2200°C. For this reason, the model was not applied for the description of high temperature tests of Kim and Olander [4].

The new AECL tests performed with the thick wall crucibles originally used in the Hofmann's tests should resolve the contradiction amongst previous experimental results and/or their interpretations and specify a particular solution of the developed general model in [11,12] corresponding to the new observations. Among the earlier found solutions for the precipitation stage corresponding to: (i) continuous dissolution of the crucible walls and roughly invariable composition of growing precipitates ([11,12]), and (ii) zero dissolution rates and varying precipitate composition ([13]); a more general solution of the model [11,12] corresponding to continuous dissolution and varying precipitate composition was also searched.

2. Experimental

This report describes the procedures and results from the following isothermal heating tests:

- 12 tests at 2100^{o}C using crucibles with no bottom isolation;
- 6 test at 2200^{o}C using crucibles with bottom isolation;
- 7 test at 2200^{o}C using crucibles with no bottom isolation; and
- 6 scoping tests to study simultaneous UO_2/ZrO_2 dissolution at 2100^{o}C

The following section gives brief generalised descriptions of the test facility and of the test and analytical procedures used for the UO_2-dissolution tests. The somewhat different procedures for the simultaneous dissolution tests are described in Section 6. Full details are provided in the four AECL interim reports that have been sent previously to FZK [11-14]. The results from each test series are documented in Sections 3 - 6 of the report. No attempt has been made in these Sections at a full interpretation of the results, however, apart from noting the more obvious trends in the data.

2.1. Materials

The crucibles, supplied by FZKA, were from the same batch as used by Hofmann et al. in their original dissolution tests [1]. Before use, each crucible was thoroughly cleaned and dried to remove any loose UO_2 powder, and the pre-test crucible dimensions and weights were recorded. The Zircaloy charges were cylinders machined from as-received Teledyne Wah Chang bar stock (nominal O content 1000 ppm). Each test series was performed with a constant UO_2/Zry mass ratio (MR) of ~12.8 for the 2100^{o}C tests, or ~18.0 for the 2200^{o}C tests.

In tests with crucible-bottom isolation, a 2.5-mm-thick yttria disc was placed on the bottom of each crucible cavity (i.e., beneath the Zircaloy charge) to confine any UO_2/Zircaloy reaction to the crucible sidewalls. These discs were either supplied by FZKA or prepared in AECL laboratories by pressing and sintering compacts of Y_2O_3.

2.2. Test procedure

In each test, the crucible and Zircaloy charge were placed inside a zirconia or thoria catch-crucible to catch any melt spillage, and positioned in the hot zone of a Centorr tungsten resistance furnace. The furnace was coupled to a 3-term Honeywell programmable controller via a type C (W-5% Re/W-26% Re) control thermocouple. Sample temperatures were continuously recorded during each test using two Ircon dual-wavelength pyrometers that had been shown by prior calibration to be accurate to within ±1%. The first pyrometer, focussed on the Zircaloy charge through a fused quartz window in the furnace roof, was used to measure reaction temperatures. A second pyrometer, focused on the lip of the UO_2 crucible through a furnace side-wall window, was used to measure the thermal lag between the crucible outer walls and the Zircaloy charge. The output from both pyrometers was recorded at 1-s intervals by a computer-based data acquisition system

Before each experiment, the furnace was evacuated and back-filled with ultra-high-purity (UHP) argon. During the experiment, the furnace was continually purged with UHP argon at a flow rate of 0.5 l/min.

Each crucible and Zircaloy charge were pre-heated to ~1600°C and held at this temperature for about 5 min to allow temperature equilibration. The specimen was then heated to the test temperature as quickly as possible, and held for the required test duration. After this time, the furnace power was turned off, allowing the specimen to cool rapidly, with an initial rate of ~4°C/s. When the temperature had fallen to ~1450^{o}C, the power was turned on again to allow slow (~1 h) cooling of the specimen to room temperature.

The time/temperature trace for each Zircaloy charge during the ramp to temperature exhibited a thermal arrest or reversal, which was attributed to endothermic melting and/or a corresponding emissivity change. Because of thermal lag across the charge, the discontinuity occurred at temperatures significantly higher than the true Zircaloy melting temperature (1760^{o}C). In some cases, more than one discontinuity was observed. This was probably due to oxygenation of the molten Zircaloy by O-diffusion from the crucible. Oxygenation of the Zircaloy charge during heating would raise its melting temperature, causing the molten alloy to refreeze, and then immediately re-melt at a slightly higher temperature.

The time at which the first time/temperature discontinuity occurred in each experiment was considered to be the time of effective Zircaloy melting. We have arbitrarily taken this time as the start of isothermal heating to account for any UO_2 dissolution occurring during the subsequent time required to reach the isothermal heating temperature.

The time/temperature parameters for each test series are listed in subsequent sections. In each table, the 'total time molten' column refers to the elapsed time between melting and the end of each test, while the 'main part of isotherm' indicates the degree of temperature control achieved during the isothermal heating period.

2.3. Sectioning procedure

Each post-test specimen was weighed. The post-test specimen dimensions from later tests were also re-measured to account for crucible sintering while at the test temperature. Each specimen was then sectioned along its cylinder-axis plane to expose the solidified melt region. One half of each specimen was polished prior to examination by optical microscopy and scanning electron microscopy/ energy-dispersive x-ray analysis (SEM/EDX). The other half was cut up to obtain two or more samples of the melt region for inductively coupled plasma (ICP) spectrometry analysis, using the following sectioning method:

Two ~1-mm slices were cut parallel to the plane of original sectioning and mounted on a glass microscope slide with thermoplastic cement. The melt region from each slice was then carefully cut out, using a diamond wafer saw and diamond grinder, and removed from the glass slide by soaking and washing in isopropyl alcohol to dissolve the cement.

In specimens from some early tests, the melt regions were cut further into top- and bottom- sections to look for possible composition gradients between the top and bottom regions. The ICP analyses for these sections were identical (within the ICP error limits), however. Hence, this additional sectioning procedure was discontinued in the later experiments.

2.4. ICP analyses of melt samples

Each sample was placed in 50 ml of a 17% HNO_3, 7% HF acid mixture in a sealed PTFE container and heated at 75^{o}C until it had dissolved. 26 ml of 2M $AlCl_3$ was then added to the solution to complex any unreacted HF and the solution was made up to 250 ml volume. ICP analysis was performed for U, Zr, Sn, Fe and Cr.

2.5. Optical microscopy

All specimen sections used for optical microscopy and SEM were ground and polished to 1-μm finishes. Reflected light microscopy was used to obtain 200-mm× 250-mm photographs of the sectioned specimens. The photographs were then sent to FZKA for computer-based image measurements of the extent of crucible dissolution.

2.6. Image processing method

Photographs showing the molten Zircaloy attack of UO_2 crucibles after various reaction times, were digitised and then analysed. The initial (before the dissolution process) geometry configuration of the crucibles was restored in the crucible cross-section images by means of graphic software Adobe Photoshop. By this method the dissolution area was determined. Under the assumption of a cylindrical symmetry of the dissolution process the dissolved volume of each crucible was calculated by means of the OPTIMAS-Software in accordance with the formula:

$$V = v \times \pi \times \sum_i r_i \ ,$$

where v is the volume of one pixel; i numerates pixels in the dissolved area; r_i is a pixel distance from the cylindrical axis.

This image analysis has allowed:

- to define separately the dissolution extent (volume and depth) of the crucible bottom and sidewalls;
- to estimate an amount of oxygen diffused from the undissolved crucible part to the melt, apart from oxygen dissolved along with the crucible walls.

2.7. SEM/EDX analyses

The specimens used for optical microscopy were re-polished to 1-μm finishes and then sputter-coated with carbon to prevent charging under the electron beam. A JEOL JSM-6300V microscope was used for SEM examinations. For most observations, backscattered electron (BSE) images were used to allow the melt phases to be easily distinguished. The tone contrast for each phase in a BSE image is a function of the mean atomic number of the component elements. Thus, U-rich alloy phases generally appear white or very light grey, (U, Zr)O_{2-x} ceramic phases appear grey, Zr-rich alloy phases appear very dark grey and voids appear black. Occasionally, however, secondary electron (SE) images were also recorded to look for topographic features in a specimen.

The EDX facility associated with the JEOL JSM-6300V microscope was a Link-Isis system. There were some initial problems with this system, and the EDX analyses

for the 2100°C test-series specimens had to be made with an older ISI D-130 microscope and a Tracor-Northern TN-2000 EDX system (see Section 3.4). After the problems with the Link–Isis system had been corrected, it was used to re-analyse selected samples from the 2100°C test series, and the two EDX facilities were shown to give virtually identical results. All subsequent EDX analyses were made with the JEOL JSM-6300V microscope/Link-Isis system.

Duplicate EDX analyses were made for the major phases in five regions located near the top-left, top-right, centre, bottom-left and bottom-right areas of each specimen. The EDX analytical standards used were pure U, Zr and Sn metal foils that were embedded in the epoxy mounting of each specimen. The Link-Isis EDX system features a so-called "windowless" detector, allowing direct analyses for O to be made using a quartz slice as the analytical standard. With the TN-2000 EDX system, the O analyses had to be obtained by difference. In practice, however, the accuracy of the direct O analyses was very much lower than that for U, Zr, or Sn, and was probably comparable to the accuracy obtained using the "by difference" method.

2.8. Phase-area analyses

Image analyses, using Link-Isis-IMquant software, were performed on × 500 BSE images recorded with the JEOL JSM-6300V instrument for the five regions in each specimen used for EDX analysis. In all specimens, there was a high area fraction of voids near the bottom of the melt, the voids being produced by melt contraction during cooling. In a few images, these voids could not be readily distinguished from the dark-toned Zr(O)-alloy phase. These images were, therefore, not used for phase-area analysis. In most cases, however, it was possible to adjust the tone-contrast threshold levels to allow the melt phases and the voids to be distinguished.

3. UO_2-crucible tests at 2100°C without bottom isolation

3.1. Tests parameters

Twelve isothermal heating experiments were performed at 2100°C, using a mass ratio (MR) value of ~12.8. The crucible density was 10.5 g/cm³ (95.5%TD). The ratio of the interaction surface to the initial melt volume (*S/V* ratio) was 370 m^{-1}. The pre-test material dimensions and weights are listed in Table 3.1. The test parameters are given in Table 3.2. Duplicate tests were performed with nominal times of 600, 1200 and 1800 s at 2100°C to check for reproducibility of the results. Fig. 3.1 and 3.2 show typical time/temperature traces recorded during Tests HF-13 and HF-1 (target times of 100 and 900 s, respectively).

3.2. ICP analyses of the melt

Table 3.3 shows the mean ICP results for the 2100°C test series in order of increasing test duration. The results are plotted as the U/(U+Zr) wt.% ratio versus $t^{0.5}$ in Fig. 3.3. Also shown is a visual best-fit curve, derived from the equation:

$$C_t = 55.8 \cdot [1 - \exp(0.0125t)],$$

where C_t is the U/(U+Zr) wt.% ratio after time t. This equation is used merely as a convenient way of summarising the data, and is not intended as a modelling equation.

3.3. Optical microscopy and image analysis of crucible cross sections

Fig. 3.4 shows the molten Zircaloy attack of UO_2 crucibles at 2100°C after 30 min reaction time. The whole image was classified into 6 different areas [19]: initial melt volumes in the crucible bore (1), solidified melt in the attacked bottom of the crucible (2), solidified melt in the dissolved interior wall of the crucible (3), transition zone between the solidified melt and the crucible basement (4), voids in the interior wall above the solidified melt (5) and the macroscopically unchanged material of the crucible (6) (Fig. 3.5). Borders of these areas were traced by computer, and the image coordinates were calibrated with the known vertical dimensions of the crucible. Fig. 3.6 shows classified areas for specimens with different reaction times at 2100°C. For all specimens the volume fractions were determined by means of the image analysis method and compared with the initial volume of liquid Zircaloy (Table 3.4; the bottom volume includes the transition zone). Table 3.4 contains also other results of the image analysis: 1) ratio of the melt height at the interaction boundary to the initial height of molten Zircaloy; 2) ratio of oxygen diffused to the melt from the undissolved crucible material, to the whole oxygen content in the melt (since this calculation is based on the indirect ("by difference") data on the oxygen content in the melt, these values are considered as qualitative estimations only).

3.4. SEM examinations

Detailed descriptions of the phase compositions and microstructures in each specimen are given in the 1st and 2nd interim AECL reports [11,12]. In general, the melt regions contained 3 major phases: a ceramic $(U,Zr)O_{2-x}$ phase with a dendritic microstructure, a Zr(O) alloy phase containing traces of U and Sn, and a U-rich U-Zr-O alloy phase that occurred as inclusions in the ceramic and Zr(O) alloy phases. These phases are seen in Fig. 3.7, a BSE micrograph from the top-left region of the HF-6 melt, although the dendritic microstructure is not readily apparent at this relatively high magnification. Similar phases and microstructures occurred uniformly throughout the melt, although the lower melt regions also contained a significant number of voids, formed during cooling.

The melt/crucible interfaces along the crucible sidewalls and base were generally sharply defined and often marked by a cooling crack. Transition zones [5,7] of up to 350-μm width had formed along the melt bottom and part way up the sidewalls in specimens from ≥ 900-s tests. Fig. 3.8 shows a typical transition zone from the right-hand corner of the HF-10 specimen. Although the phases within the transition zones were too small for EDX analysis, the atomic number contrast suggested that they consisted of a ceramic $(U,Zr)O_{2-x}$ phase and a Zr(O) alloy phase. In specimens from tests of < 900-s duration, the transition zones were either non-existent or were confined to the bottom corners of the melt.

In all specimens, U-metal precipitates and associated pores were distributed throughout the residual crucible except for within a 300- to 500-μm-wide zone immediately adjacent to the melt (the "U-metal-free zone"), which also exhibited a lower pore density. However, relatively large U-metal precipitates were observed at many locations at the melt/crucible interface, sometimes forming a thin U-metal layer at the interface. These features are illustrated in Fig. 3.9**,** a micrograph of the left sidewall in the HF-7 specimen. The origin of these features has been discussed previously [7].

In many cases, the U-metal precipitates at the interface were in sharp contact with Zr(O) alloy material in the central melt region, indicating that the precipitates must

have formed and/or migrated after the melt had solidified during specimen cooling. A typical example is shown in Fig. 3.10, a micrograph of the interface along the bottom of the HF-6 melt.

3.5. EDX analyses

For each specimen, duplicate analyses were made for the $(U,Zr)O_{2-x}$ ceramic phase and the Zr(O) alloy phase in the five melt regions used for SEM examination. The U-rich alloy phase generally occurred as <1-μm regions that were too small for EDX analysis. In the shorter-duration test specimens (HF-13, HF-6 and HF-12), however, this phase was more abundant and occurred as somewhat larger precipitates, so that some analyses could be made. Table 3.5 summarises the mean results for the three phases.

The EDX analysis results for the 2100°C-test specimens showed no statistically significant variation in the phase compositions at different locations within each melt region. In general, the Zr(O) phase composition approximates to that of O-saturated Zr containing minor quantities of Sn and U. The U/Zr ratio in the ceramic $(U,Zr)O_{2-x}$ phase appears to decrease with increasing time after ~360 s at the reaction temperature, as shown in Fig. 3.11. In each analysis, the accuracy of the value for O is significantly lower than that for U, Zr or Sn. Taken as a whole, however, the O analyses suggest that the ceramic phase in all specimens was significantly hypostoichiometric.

3.6. Phase-area analyses

Image analyses were performed on x 500 BSE micrographs of the areas used for EDX analysis. The mean results for the 2100°C specimens are listed in Table 3.6 and plotted against $t^{1/2}$ in Fig. 3.12.

3.7. Summary of the major data trends

1. The ICP analyses indicate that the 2100°C melts became saturated within ~360 s, and showed essentially no change in U/(U + Zr) wt.% ratio thereafter. The data could be adequately described by the equation:

$$C_t = 55.8 \cdot [1 - \exp(0.0125t)],$$

   where C_t is the U/(U+Zr) wt.% ratio after time t (s).

2. The frozen melts in each specimen contained 3 major phases: a dendritic ceramic $(U,Zr)O_{2-x}$ phase, a Zr(O) alloy matrix phase, and a U(O) phase that occurred in low concentrations as inclusions in the ceramic and Zr(O) alloy phases.

3. The EDX and phase-area analysis results showed no statistically significant variation in the phase compositions or distributions at different locations within each melt region, indicating that the melts were essentially homogeneous prior to cooling, i.e., that there had been good convective stirring of the melt during the test.

4. The U/Zr ratio in the ceramic $(U, Zr)O_{2-x}$ phase of the cooled specimens decreased with increasing time after ~360 s at 2100°C.

5. The area fraction of the (U,Zr)O_{2-x} phase became greater with increasing reaction time up to ~20 min, with a corresponding decrease in the area fraction of the Zr(O) alloy phase. After this time, the area fractions of these two phases remained approximately constant. The area fraction of the U(O) alloy phase was greatest (~5.8%) in the shortest duration (125-s) test specimen, but decreased by a factor of ~2 in specimens reacted for > 300 s.

4. UO_2-crucible tests at 2200°C with bottom isolation

4.1. Tests parameters

Six isothermal heating experiments with bottom isolation were performed at 2200°C, each with a ~2.5-mm-thick sintered yttria disc on the crucible floor to confine any UO_2/Zircaloy reaction to the crucible sidewalls. The crucible density was 10.5 g/cm³ (95.5%TD). The ratio of the interaction surface to the initial melt volume (*S/V* ratio) was 240 m^{-1}. The tests were performed with a MR value of ~18 (i.e., using less Zircaloy) to allow for (i) the increased UO_2 solubility at the higher temperature, and (ii) the reduction in crucible-cavity volume caused by inclusion of the yttria disc.

The pre-test material dimensions and weights are given in Table 4.1. The test parameters are given in Table 4.2. Fig. 4.1 and 4.2 show typical time/temperature traces recorded during Tests HF-19 and HF-15 (target times of 100 s and 400 s, respectively).

Test HF-26 and HF-30 both failed because of melt penetration through the sidewalls after 600-800 s. Nevertheless, there was sufficient melt remaining in each crucible for ICP and SEM/EDX analyses to be performed. Because crucible failure occurred at a late stage in these tests, each melt should have been close to its saturation composition at the time of failure. Hence, it is probably valid to use the melt analyses, together with data from shorter-time tests, to model fuel dissolution during the saturation stage.

4.2. ICP analyses

Table 4.3 shows the mean ICP results for the 2200°C test series in order of increasing test duration. The results are plotted as the U/(U+Zr) wt.% ratio versus $t^{0.5}$ in Fig. 4.3. Also shown is a visual best-fit curve, derived from the equation:

$$C_t = 74.0 \cdot [1 - \exp(0.0105t)],$$

where C_t is the U/(U+Zr) wt.% ratio after time t. This equation is used merely as a convenient way of summarising the data, and is not intended as a modelling equation.

4.3. Optical microscopy and image analysis of crucible cross sections

Fig. 4.4 shows the molten Zircaloy attack of UO_2 crucibles at 2200°C after 7 min reaction time. The whole image was classified into 4 different areas (Fig. 4.5): initial melt volume in the crucible bore, solidified melt in the dissolved interior wall of the crucible, voids in the interior wall above the solidified melt and the macroscopically unchanged material of the crucible. Borders of these areas were traced and the

image coordinates were calibrated with the known vertical dimensions of the crucible. Fig. 4.6 shows the classified areas for specimens with different reaction times. For all specimens the volume fractions were determined by means of the image analysis method and compared with the initial volume of liquid Zircaloy (Table 4.4). Table 4.4 contains also other results of the image analysis: 1) ratio of the melt height at the interaction boundary to the initial height of molten Zircaloy; 2) ratio of oxygen diffused to the melt from the undissolved crucible material, to the whole oxygen content in the melt.

4.4. SEM examinations

Detailed descriptions of the phase compositions and microstructures in each specimen are given in the 2nd and 3rd interim AECL reports [12, 13]. The six 2200°C specimens exhibited microstructures that had not been observed previously in earlier specimens from the FZK/AECL experiments or from previous UO_2/molten Zircaloy dissolution tests [1-7]. In particular, the (U, Zr)O_{2-x} phase in the frozen melts was zoned, and contained a core of ceramic material with a relatively high Zr:U ratio, surrounded by further ceramic material of lower Zr:U ratio. The BSE micrographs show the zones as dark-toned material at the centre of each ceramic region, with lighter-toned material at the periphery. Based on the tone contrast, the degree of composition variation between the ceramic zones appeared to decrease with longer times at 2200°C. This observation was confirmed by the EDX results (see Section 4.4).

The yttria discs were generally very successful in preventing access of the melt to the crucible floor. In some specimens, a small amount of melt penetrated down the disc sides, but this amount was insignificant in determining the course of melt/crucible reaction. The discs showed no signs of dissolution, as also confirmed by the ICP analyses for Y. The only evidence for yttria reaction was that each post-test disc was black. By analogy with the black colour of hypostoichiometric ZrO_2, we assume that this indicates loss of oxygen to form Y_2O_{3-x}.

The microstructures observed throughout each frozen melt were remarkably uniform, although the lower melt regions contained voids formed by melt contraction during cooling. This uniform microstructure indicates good convective stirring at the test temperature. No transition zones were observed in any of the specimens from this test series.

In general, 3 major phases were present in the frozen melts: (i) a zoned ceramic (U,Zr)O_{2-x} phase with a dendritic microstructure; (ii) a Zr(O) alloy phase containing traces of U and Sn; and (iii) a U(O) alloy phase containing traces of Zr, which occurred as distinct regions in contact with the ceramic phase, or as inclusions in the ceramic and Zr(O) alloy phases. Typical ceramic dendrites are seen in Fig. 4.7, a BSE micrograph of the bottom right corner of the HF-17 specimen. The micrograph also shows part of the yttria disc. The apparent curvature in the yttria disc is produced by slight image distortion at low magnification.

The zoned ceramic phase consisted of a central (U,Zr)O_{2-x} region that was relatively Zr-rich, surrounded by further (U,Zr)O_{2-x} material of lower Zr content. Numerous sub-micron-sized inclusions of dark-toned material, too small for EDX analysis, were also present in the ceramic zones, and were especially concentrated at the interface between the ceramic zones. Secondary electron (SE) images confirmed that the majority of these inclusions were not pores, although some pores were also present. Based on their dark tone in the BSE images, the inclusions were probably Zr(O) alloy material.

The difference in composition between the ceramic zones, which was indicated by the degree of tone contrast in the BSE-images, did not vary systematically with reaction time. The greatest difference occurred in the zoned ceramic phases from the shortest-duration test specimens (HF-19 and HF-17), but was less evident in the other specimens. This is seen by comparing Fig. 4.8 and Fig. 4.9**,** which are BSE micrographs of the central regions in the HF-19 (138 s at 2200^{o}C) and the HF-15 (428 s at 2200^{o}C) specimens, respectively. The tone contrast between the zones is very evident in the HF-19 micrograph but scarcely visible in the HF-15 micrograph.

In all cases, the melt/crucible interfaces along the crucible sidewalls were sharply defined and marked by a cooling crack. A 250- to 350-μm-wide U-metal-free zone of low porosity occurred immediately adjacent to each melt. Relatively large U-metal precipitates were often seen at the melt/crucible interfaces, however, sometimes forming thin layers of U-metal. In other regions of the residual crucibles, U-metal precipitates had formed at the grain boundaries, together with associated pores. These features are illustrated in Fig. 4.10, which shows part of the melt/crucible interface from the right sidewall of the HF-26 specimen.

4.5. EDX analyses

Duplicate EDX analyses were performed on the phases in the five melt regions used for SEM examination of the HF-15, HF-17, HF-18 and HF-19 specimens. Spot-EDX analyses were made for the inner and outer zones of the $(U,Zr)O_{2-x}$ ceramic phase, the Zr(O) alloy matrix phase and the U(O) alloy phase. In the specimens from failed tests HF-26 and HF-30, however, each melt had partially drained out of the crucible, so that EDX analyses could only be made in three horizontal regions: A, left side; B, right side; and C, centre. The spot-EDX results are listed in Table 4.5.

In general, the Zr(O) phase composition approximates to that of O-saturated Zr containing minor quantities of Sn and U. The ceramic-zone compositions varied with reaction time in a complex way. The outer (U-rich) zone composition remained fairly constant with time, while the inner (Zr-rich) zone composition varied in a non-linear way, as shown in Fig. 4.11.

EDX analyses were also performed on large (6-mm tall by 4-mm wide) areas from the left, centre and right melt regions of the HF-15, HF-17, HF-18 and HF-19 specimens. These analyses were made at FZKA's request to check for composition gradients across each specimen. The large-area analysis results are shown in Table 4.6.

The large-area analyses consistently gave higher O concentrations for the centre region than for the outer regions. This may, in part, be due to the fact that the central region usually contained a higher area fraction of voids, formed during cooling. These voids became infilled with epoxy resin during specimen preparation, so that the EDX analyses for O also included oxygen within the resin. However, the U/(U + Zr) ratios in all three areas were remarkably consistent.

There was approximate agreement between the ICP and large-area EDX results, although the U/(U + Zr) ratios calculated from the large-area EDX results were generally slightly lower. Both methods seem to confirm that the frozen melts were macroscopically homogeneous, indicating good convective circulation during each test. We believe, however, that the ICP results are generally more reliable.

4.6. Phase-area analyses

Image analysis was performed on x 500 BSE micrographs of the areas used for spot-EDX analyses. The results are listed in Table 4.7 and plotted against $t^{1/2}$ in Fig. 4.12. The trends for each phase were similar to those from the 2100°C tests without bottom isolation. Thus, the *total* ceramic phase area showed an overall increase with time, with a corresponding decrease in the area fraction of the Zr(O) alloy phase. The area fraction of the U(O) alloy phase also decreased with time by a factor of ~3 within the timeframe of the tests.

4.7. Summary of the major data trends

Interpretation of the data is made more complex by the fact that the final two tests in this series failed. Nevertheless, if it is assumed that no significant changes in melt composition occurred after the melts penetrated the crucible sidewalls in these tests, the following conclusions can be drawn:

1. The melts in this test series became saturated after ~ 400 s and subsequently showed no significant change in U/(U + Zr) wt.% ratio for times up to ~ 850 s. The ICP results gave a good visual fit to the equation:

$$C_t = 74.0 \cdot [1 - \exp(0.0105t)],$$

   where C_t is the U/(U+Zr) wt.% ratio after time t (s).

2. The frozen melts in each specimen contained 3 major phases: a dendritic ceramic $(U,Zr)O_{2-x}$ phase with a zoned microstructure, a Zr(O) alloy matrix phase that also occurred as inclusions between the ceramic zones, and a U(O) phase that occurred in low concentrations as inclusions in the ceramic and Zr(O)-matrix phases.

3. The zoned ceramic phase in the frozen melts was unlike anything observed in previous Canadian, German or American test specimens. It is not clear from the micrographs whether the zoning was formed at temperature or during specimen cooling. The composition difference between the ceramic zones did not follow a simple trend. Although the composition of the outer zone remained fairly constant with reaction time, the inner zone composition varied with time in a non-linear way.

4. The spot-EDX, large-area-EDX and phase-area analyses showed no statistically significant variation in the phase compositions or distributions at different locations within each specimen, indicating that the melts were reasonably homogeneous at the test temperature.

7. The combined area fractions of the two $(U,Zr)O_{2-x}$ phases showed an overall increase with time, with a corresponding decrease in the area fraction of the Zr(O) alloy phase. The area fraction of the U(O) phase decreased with time by a factor of ~3 within the timescale 138 - 854 s.

5. UO_2-crucible tests at 2200°C without bottom isolation

5.1. Test parameters

Seven isothermal heating experiments without bottom isolation (i.e., with no yttria discs on the crucible floors) were performed at 2200°C, MR = ~18, to provide data for comparison with the bottom-isolation test series (Section 4). The crucible density was 10.0 g/cm³ (91.1%TD). The ratio of the interaction surface to the initial melt volume (S/V ratio) was 400 m^{-1}. The UO_2 crucibles used in these tests, also supplied by FZK, were more porous than those employed in previous tests, although they were perfectly adequate for performing the dissolution tests. The target times at temperature were 100, 200, 300, 400 and 600 s.

The pre-test material dimensions and weights are listed in Table 5.1. The test parameters are given in Table 5.2. Test HF-21 was a duplicate of HF-20, except that the furnace control parameters were adjusted to give a faster ramp rate. The time/temperature trace for test HF-24 contained artifacts caused by bubbles at the melt surface. Hence, this test was repeated, and test HF-28 is essentially a duplicate of HF-24. Fig. 5.1 and 5.2 show typical time/temperature traces recorded during Tests HF-28 (150 s) and HF-20 (613 s), respectively.

5.2. ICP analyses

Table 5.3 lists the mean ICP results for the 2200°C test series in order of increasing test duration. The results are plotted as the U/(U+Zr) wt.% ratio versus $t^{1/2}$ in Fig. 5.3. Also shown is a visual best-fit curve, derived from the equation:

$$C_t = 74.0 \cdot [1 - \exp(0.014t)],$$

where C_t is the U/(U+Zr) wt.% ratio after time t. As before, this equation is used merely as a convenient way of summarising the data, and is not intended as a modelling equation.

5.3. Optical microscopy and image analysis of crucible cross sections

Fig. 5.4 show the molten Zircaloy attack of UO_2 crucibles at 2200°C after 7 min. reaction times. The whole image was classified into 5 different areas (Fig. 5.5): initial melt volumes in the crucible bore, solidified melt in the attacked bottom of the crucible, solidified melt in the dissolved interior wall of the crucible, the voided of the interior wall above the melt and the macroscopically unchanged material of the crucible. Fig. 5.6 shows classified areas for specimens with different interaction times. For all specimens the volume fractions were determined by means of image analysis method and compared with the initial volume of liquid Zircaloy (Table 5.4).

The comparison between the image analysis results of the element content in the melt with the exact results of the chemical analysis allows an estimation of the precision of the image analysis method. Fig. 5.7 illustrates a good correlation between the results of image analysis (performed by FZKA) and chemical analysis (performed by AECL). A comparison between the UO_2 dissolution results obtained at two temperatures 2100 and 2200°C shows that the rates and extents of UO_2 dissolution are greater at higher temperatures (Fig. 5.8).

5.4. SEM examinations

Specimens from tests HF-28, HF-27, HF-29, HF-22 and HF-21, covering the full range of test times at 2200°C, were used for SEM/EDX analysis. Detailed descriptions of the phase compositions and microstructures in each specimen are given in the 3rd interim AECL report [13].

In general, the melt regions contained 3 major phases: a ceramic $(U,Zr)O_{2-x}$ phase with a dendritic microstructure, a Zr(O) alloy phase containing traces of U and Sn, and a U-rich U-Zr-O alloy phase that occurred as inclusions in the ceramic and Zr(O) alloy phases. The ceramic phase showed no evidence of zoning. The ceramic dendrites are shown in Fig. 5.9, a low-magnification micrograph of the bottom-centre melt region in the HF-28 specimen. The relatively large void regions in the micrograph were caused by melt contraction during cooling. The major phases are more clearly seen in Fig. 5.10**,** which is a higher magnification BSE micrograph of the top-right region in the HF-28 specimen.

Transition zones had formed at the melt/crucible interfaces along the base, with the greatest thickness occurring in specimens from the longer-time tests. The transition zone thickness ranged from ~75 μm in the HF-28 (150-s) specimen to ~400 μm in the HF-21 (612-s) specimen. The phases within the transition zones were generally too small for EDX analysis. Based on the atomic number contrast in the BSE images, however, the zones appeared to contain a major $(U,Zr)O_{2-x}$ ceramic phase with inclusions of Zr(O). Fig. 5.11 shows the transition zone at the bottom centre region of the HF-21 specimen. No transition zones were observed at the melt/crucible interfaces along the sidewalls.

The residual crucibles contained large pores that were almost certainly present in the pre-test crucibles, which were more porous than the better-quality crucibles used in other test series. U-metal precipitates occurred throughout each residual crucible and were associated with fine pores that were likely created at the same time as the U-metal precipitates. However, a 300- to 400-μm-wide U-metal-free zone, in which these fine pores were absent, was present adjacent to each melt. Some U-metal precipitates were also seen at the crucible/melt interface. These features are illustrated in Fig. 5.12, which shows the melt/crucible interface at the left sidewall of the HF-22 specimen.

5.5. EDX analyses

Duplicate EDX analyses of the ceramic and Zr(O) alloy phases were made at five regions within each melt region. A few EDX analyses were also made for the U(O) phase in the HF-28 specimen, giving the following mean at.% composition (±2SD): U, 51.7 ± 4.7; Zr, 1.3 ± 0.7; Sn, 0.1 ± 0.1; O, 46.9 ± 4.9.

The EDX analyses for the ceramic and Zr(O) alloy phases within each melt region were in excellent agreement, confirming that the melts had been essentially homogeneous before cooling. The mean analyses are summarized in Table 5.5. Fig. 5.13 is a plot of the U/(U+Zr) atom fraction in the ceramic phase versus $t^{0.5}$, and shows a continual decrease in the U/(U+Zr) fraction with increasing test time.

5.6. Phase-area analyses

Image analyses were performed on ×500 BSE micrographs of the areas used for EDX analysis. The results are shown in Table 5.6 and plotted in Fig. 5.14.

5.7. Summary of the major data trends

1. The ICP analyses indicate that the 2200°C melts became saturated within ~320 s, and subsequently showed no significant change in U/(U + Zr) wt.% ratio for times up to ~610 s. The ICP results were adequately described by the relationship:

$$C_t = 74.0 \cdot [1 - \exp(0.014t)],$$

where C_t is the U/(U+Zr) wt.% ratio after time t (s). For comparison, the corresponding equation for the data from 2200°C tests with bottom isolation (Section 4) was:

$$C_t = 74.0 \cdot [1 - \exp(0.0105t)].$$

Hence, the presence of the yttria disc influenced the rate of saturation, but not the final saturation concentration.

2. The spot-EDX and phase-area analysis results showed no significant variation in the phase compositions or distributions at different locations within each melt region, indicating that the melts were essentially homogeneous before cooling.
3. The U/Zr ratio in the ceramic (U, Zr)O_{2-x} phase of the cooled specimens decreased with increasing time after ~320 s at 2200°C.
4. The area fraction of the (U,Zr)O_{2-x} phase increased at longer reaction times (up to ~ 610 s) at 2200°C, with a corresponding decrease in the area fraction of the Zr(O) alloy. The area fraction of the U(O) alloy phase also decreased at longer times by a factor of ~ 4.

6. Simultaneous UO_2-ZrO_2-molten Zircaloy tests at 2100°C

This section describes six scoping tests that were performed at 2100°C to study the simultaneous dissolution of UO_2 and ZrO_2 in molten Zircaloy. The test and analysis procedures, which were broadly similar to those used for the UO_2-dissolution tests, are fully described in the 4th interim AECL report [13]. The important differences in procedure are described below.

6.1. Materials

The UO_2 crucibles used for these tests were the last of a batch of high-density crucibles supplied by FZKA. In each crucible, a 6.45-mm diameter central rod of Ca-stabilised ZrO_2 was located along the cylinder axis by a hole in the centre of the crucible floor. A ~2-mm thick yttria disc, with a central hole to allow the rod to pass through, was placed on the cavity floor. Thus, any reaction with UO_2 was confined to the crucible sidewalls.

The Zircaloy charge was machined to fit the UO_2 crucible, with a central hole to accommodate the ZrO_2 rod. The target UO_2/Zircaloy mass ratio was 12.8, as used in the UO_2/molten Zircaloy dissolution test series at 2100°C (Section 3). The crucible

configuration is shown in Fig. 6.1. The pre-test dimensions and weights of the specimen components are given in Table 6.1.

A thick-walled thoria catch crucible, supplied by FZK, was used in all tests. The crucible sidewalls stood clear of the catch crucible, and were, therefore, not shielded from the furnace element.

6.2. Test procedure

The six 2100^{o}C tests (HF-31 to HF-36) were performed using the same tungsten resistance furnace, pyrometers and data-logging equipment as before. Molten Zircaloy temperatures were measured by sighting the upper pyrometer onto the melt-filled gap between the outer UO_2 crucible and the inner ZrO_2 rod. The crucible had to be offset ~7-mm from the centre of the furnace stage to sight the pyrometer down this gap, so that specimen heating was, unavoidably, not completely uniform.

Table 6.2 lists the time/temperature parameters for each test. After the initial two tests (HF-31 and HF-32), the furnace-control parameters were adjusted to give a faster ramp to 2100^{o}C. Fig. 6.2 and 6.3 show representative time/temperature traces for the HF-31 and HF-34 tests. The post-test cross-sections of crucibles are shown in Fig. 6.4. Fig. 6.5 clarifies the interaction zones.

Test HF-36 (target 2100^{o}C for 500 s) failed because the melt penetrated the crucible sidewall after ~423 s (estimated from the time/temperature trace) and drained into the catch crucible. During the test time, the ZrO_2 rod had fully dissolved. Melt samples were retrieved from the catch crucible for ICP analysis, but no SEM/EDX analyses were made with this sample.

Each post-test specimen was sectioned along its cylinder-axis plane to expose the solidified melt region. One half was polished to a 1-μm finish and examined by optical microscopy and SEM/EDX. The other half was cut into slices to obtain four representative samples of the melt region for ICP analysis, using a similar sectioning method as described in Section 2.3, but excluding any undissolved ZrO_2 rod from the analysis sample.

6.3. ICP analyses

All four samples from each specimen were dissolved as described in Section 2.4. Five samples of the ZrO_2 rod were also crushed and dissolved in the same way. ICP analyses were performed for U, Zr, Hf, Ca, Mg, Sn, Fe and Cr.

The Hf/Zr ratio in the rod material was used, in conjunction with the ICP melt analyses for Hf, to calculate the amount of dissolved rod in each melt. The calculation relied on the assumption that Hf dissolves congruently with Zr, based on their similar chemical properties and almost identical ionic radii (0.144 nm and 0.145 nm, respectively, for Hf^{4+} and Zr^{4+}). The mean Hf/Zr ratio (wt.%) in the central ZrO_2 rod, based on five ICP analyses, was $(23.28 \pm 1.08)\times10^{-3}$. The mean Hf/Zr ratio (wt.%) in the original Zry was $\sim0.05\times10^{-3}$. Thus, the initial Hf content of the Zircaloy charge could be safely ignored in the calculations.

The mean ICP results are shown in Tables 6.3 and 6.4. Fig. 6.6 shows $Zr_{crucible}/Zr_{total}$, the weight ratio of crucible-derived Zr in the melt to the total melt Zr content, plotted against $t^{1/2}$. Fig. 6.7 shows the U/(U+Zr) wt.% ratio of the melts plotted against $t^{1/2}$.

6.4. SEM examinations

Specimens from tests HF-31 to HF-35 were polished to a 1-μm finish. Reflected-light micrographs were taken and forwarded to FZKA for computer-based image measurements of the extent of crucible and rod dissolution. The specimens were then re-polished, carbon coated and used for SEM/EDX analysis.

The amount of dissolution in the central zirconia rod in each specimen may be summarised as follows:

HF-33 (108 s): Significant dissolution had occurred, being greatest at the mid-height level in the exposed rod section (i.e., above the yttria disc).

HF-32 (206 s): The rod had almost completely dissolved, leaving only a thin vertical «neck» connecting the top and bottom parts above the yttria disc.

HF-34 (216 s): The exposed rod section had almost completely dissolved, leaving only a stub of ZrO_2 above the yttria disc at the bottom of the crucible.

HF-35 (315 s): The entire rod section exposed to the melt had dissolved, and some of the rod section below the level of the yttria disc had also disappeared.

HF-31 (554 s): The entire rod section exposed to the melt had dissolved. Most of the rod section below the yttria had also disappeared, leaving only a stub in the bottom of the cavity in the crucible floor.

In other respects, however, the specimen microstructures were fairly similar. The melts all contained three major phases: (i) a ceramic $(U,Zr)O_{2-x}$ dendritic phase; (ii) a Zr(O) alloy phase containing traces of U and Sn; and (iii) a U(O) alloy phase, which occurred as inclusions in the ceramic and Zr(O) alloy phases. Occasional traces of a Zr-Sn-O phase were also observed in some specimens. The ceramic dendrites are seen in Fig. 6.8, a BSE micrograph from the centre of the HF-33 specimen that also shows the remaining undissolved zirconia rod.

The ceramic phase was quite strongly zoned, and resembled the ceramic phase seen in specimens from the 2200°C UO_2-dissolution tests with bottom isolation (see Section 4). Thus, the central $(U,Zr)O_{2-x}$ zone was relatively Zr-rich, while the outer zone was richer in U. Numerous sub-micron-sized inclusions of Zr(O) material occurred in the central ceramic zone and especially at the interface between the two zones. Fig. 6.9 shows the phases from the bottom-left region of the HF-32 specimen, in which the ceramic-phase zoning was quite pronounced.

In general, the melt/crucible interfaces along the crucible sidewalls and base were sharply defined, and no transition zones were observed in any specimens. U-metal precipitates and associated fine pores occurred throughout the residual crucible, except for within the 250- to 600-μm U-free zone adjacent to the melt. Some U-metal precipitates were also seen at the crucible/melt interface, particularly in the HF-31 specimen. These features were very similar to those observed in the residual crucibles of all previous test specimens, and are illustrated in Fig. 6.10, a BSE micrograph of the left sidewall from the HF-31 specimen.

The interface between the melt and any undissolved ZrO_2 rod in a specimen was also fairly sharp. This is illustrated in Fig. 6.11, a BSE micrograph of the bottom-centre region of the HF-32 specimen that also shows the conical remnants of the zirconia rod. The yttria disc at the bottom of each melt showed no evidence of dissolution.

6.5. EDX melt analyses

Duplicate analyses of the ceramic and Zr(O) alloy phases in the melt regions of the HF-31, HF-34 and HF-35 specimens were made at five regions, located in the top-left, top-right, centre, bottom-left and bottom-right of each melt. For the remaining specimens, duplicate analyses of these phases were made at six regions, located in the top-left, top-right, centre-left, centre-right, bottom-left and bottom-right of each melt. A few analyses of the U(O)-rich alloy inclusions in the HF-33 and HF-32 specimens were also made.

The EDX analyses for each phase within a specimen were in generally good agreement. The mean analyses are summarised in Table 6.5. The Zr(O) alloy approximated to O-saturated Zr containing minor amounts of U and Sn. The variation in the compositions of the inner and outer ceramic zones with time is shown in Fig. 6.12. In general, the composition of the outer zone remained constant with increasing time, while the inner zone became progressively more U-rich.

6.6. Phase-area analyses

Image analyses were performed on x 500 BSE micrographs of the areas used for EDX analysis. The results are listed in Table 6.6 and plotted versus $t^{0.5}$ in Fig. 6.13 and 6.14. There is a trend for the area fractions of the Zr(O) and U(O) alloy phases to decrease with time. Conversely, the area fraction of the outer U-rich ceramic zone increases with time, while that of the inner zone remains more or less constant.

6.7. Summary of the major data trends

1. The reproducibility of the Hf/Zr ratios in the ZrO_2 rod samples supports the use of the Hf/Zr melt ratios to calculate the amount of dissolved ZrO_2 in the melt.
2. The $Zr_{dissolved}/Zr_{total}$ melt ratios indicate that ZrO_2 dissolution was fairly rapid. After ~225 s, the rod in the melt had completely dissolved, so that the $Zr_{dissolved}/Zr_{total}$ ratio remained approximately constant at longer times. Any subsequent slight increase was probably due to dissolution of the rod stub in the within the crucible-floor cavity. It should be noted, however, that the $Zr_{dissolved}/Zr_{total}$ result for HF-32 is anomalously low.
3. The U/(U + Zr) wt.% ratios in the simultaneous-dissolution tests with bottom isolation reached their saturation value of ~63% after ~400 s. For comparison, the saturation value from previous 2100°C UO_2-dissolution tests without bottom isolation (and with no ZrO_2 rod present) was ~56% after ~400 s (see Section 3). It is known from previous work [2,4,6] that oxygenation of molten Zircaloy reduces the UO_2 solubility, i.e., produces lower U/(U + Zr) wt.% ratios at saturation. The extent of melt oxygenation in these two test series involves the following factors:

(a) The absence of bottom isolation, as in the UO_2-dissolution tests, would allow more O to diffuse into the melt, thereby lowering the U/(U + Zr) wt.% saturation value. On this basis, the result for the UO_2-dissolution tests should be lower than that from the simultaneous-dissolution tests, in agreement with the present data.

(b) Dissolution of the zirconia rod would have enriched the melt in two atoms of O for every atom of Zr. Thus, the rapid ZrO_2 dissolution observed in the simultaneous-dissolution tests should, in theory, have increased the melt oxygen content and, hence, reduced the U/(U+Zr) wt.% saturation level. This prediction is not supported by the present data, however.

It may be possible to reconcile these opposing predictions with the saturation data by postulating that the two test series were performed at slightly different temperatures. The uniformity of heating in the simultaneous dissolution tests was not as satisfactory as in the UO_2-dissolution tests, because each crucible had to be positioned slightly off-centre in the furnace to allow the upper pyrometer to focus on the melt (see Section 6.2). Future simultaneous dissolution tests should be designed to avoid this problem. Furthermore, the temperature control achieved in the simultaneous dissolution tests was generally poorer than in the UO_2-dissolution tests.

4. The spot-EDX and phase-area analysis results showed no significant variation in the phase compositions or distributions at different locations within each melt region, indicating that the melts were essentially homogeneous at 2100^{o}C.
5. The zoned ceramic phase was similar to that seen in the 2200^{o}C UO_2-dissolution tests with bottom isolation. It is not clear from the micrographs whether the zoning was formed at temperature or during specimen cooling. Fig. 6.12 indicates that the composition variation between the two ceramic zones diminished with increasing reaction time, probably as the melts approached saturation. The composition of the Zr(O) alloy phase did not change significantly with reaction time, however, and approximated to O-saturated Zr containing minor amounts of U and Sn.
6. The combined area fractions of the two $(U,Zr)O_{2-x}$ phases showed an overall increase with time, with a corresponding decrease in the area fraction of the Zr(O) alloy phase (see Figs. 6.13 and 6.14). The area fraction of the inner (Zr-rich) ceramic zone remained approximately constant in all specimens, whereas the area fraction of the outer (U-rich) ceramic zone increased with time. The area fraction of the U(O) alloy phase decreased with increasing time.

7. Modelling of UO_2 dissolution by molten Zircaloy

The following section gives brief generalised descriptions of the UO_2-dissolution tests modelling. Generalisation of the UO_2 dissolution model to description of the scoping tests on the simultaneous UO_2 and ZrO_2 dissolution, is presented in Section 8. Full details are provided in the five interim IBRAE reports that have been sent previously to FZKA [20-24].

7.1. Basic model

In accordance with the previously developed model [11,12], the bulk melt composition in the crucible tests attains its saturation value during the short time interval of the first, saturation period. In the subsequent time interval (precipitation period) the continued oxygen supply to the interface by diffusion from fuel interior leads to an oversaturation of the melt, resulting in precipitation of the ceramic $(U,Zr)O_{2-x}$ phase in the melt. Simultaneously, dissolution of solid UO_2 can be continued (and can be accompanied by disintegration of the solid phase boundary with the same composition $(U,Zr)O_{2-x}$ as precipitated particles). Therefore, the oxygen diffusion in the solid UO_2 phase determines the kinetics of both processes of the UO_2 dissolution and the formation of $(U,Zr)O_{2-x}$ precipitates after completion of the saturation stage, and for this reason these kinetics have to obey a parabolic time law ($\propto t^{1/2}$) in the precipitation stage.

It was demonstrated by Kim and Olander [4] that in the case of a vertical position of the solid/liquid interface a mass transfer in the liquid phase could be produced by

natural convection driven by the density differences in the melt (due to the large weight of U atoms in comparison with Zr atoms). A rather high value of the mass transfer coefficient estimated in [4] was re-evaluated and confirmed in the paper [11] by the analysis of the concentration profiles observed in the crucible melts. The values of the convective mass transfer coefficients estimated in [4]: $k_O \approx 10^{-2}$ cm/s, $k_U \approx 0.5\times10^{-2}$ cm/s, are also used in the present report for modelling of the new crucible tests. However, it was emphasised in [11] that for description of the material interactions in the real geometry of the fuel rods these values should be decreased by a corresponding factor (so called aspect ratio). A significant increase of the mass transfer coefficient under real conditions of severe accidents can also take place owing to the temperature gradient induced enforcement of the convective stirring of the melt.

The consideration of the UO_2 crucible interactions with the Zry melt in the previously developed model [11,12] was performed in the framework of the simplified one-dimensional (1-d) model with the cylindrical geometry and linear dimensions (radii) corresponding to the same *S/V* (surface to melt volume) ratio as in the crucibles at the beginning of interactions.

7.2. Development of two-dimensional model

In order to account for the observed continuous increase of the melt volume (see Table 3.4, 4.4 and 5.4) and interactions of the melt with fresh surfaces of the UO_2 crucible (see Fig. 7.1), a new two-dimensional (2-d) model was developed. The model generalises the simplified 1-d model, in which linear dimensions of the interaction system in the vertical direction was fixed and invariable with time. Such a consideration apparently does not correspond to the real geometry of the crucible tests in which melt dissolves crucible bottom simultaneously with the walls, on the one hand, and the upper level of the melt continuously increases in the course of dissolution process, on the other hand. As can be concluded from the comparison of the results of the present report and previous ones [20-22], the 1-d model allows satisfactory predictions of the variation of the uranium weight content in the melt, however, incorrectly describes the depth of the dissolved crucible walls.

The molar density of pure liquid U is ≈ 0.071 mol/cm^3 and of liquid Zr is ≈ 0.064 mol/cm^3, thus it was assumed that the molar density of the melt is independent of the U/Zr ratio:

$$c_U + c_{Zr} + \theta c_O = \text{const.} = c_M \approx 0.068 \text{ mol/cm}^3, \quad (1)$$

where $0\le\theta\le1$ (see [11,12]). In the limiting case $\theta=1$ the molar density of the melt is independent of its composition and is denoted by c_M. In the other limiting case $\theta=0$ the molar density of the melt is independent of the dissolved oxygen concentration and is denoted by c_M on an oxygen-free basis [10]. In order to verify what value of the parameter is more appropriate, the evaluation of the molar density of the melt ρ_L on the base of the full experimental data set in the test series 2200°C without bottom isolation (see Section 5), is performed in Appendix 1. Results of this evaluation show that the approximation $\theta=1$ fairly corresponds to the above presented assumption on the invariable melt concentration $c_M \approx 0.068$ mol/cm^3, whereas in the

case θ=0 one should propose a steep decrease of c_M from 0.064 mol/cm^3 (in the beginning) to ≈ 0.034 mol/cm^3 in the course of crucible dissolution. For these reasons, the approximation θ=1 is accepted in the model calculations as a more realistic one.

7.2.1. Saturation stage

During the first, saturation stage a rather quick dissolution of UO_2 and saturation of molten Zry with U and O atoms up to the limiting value (determined by the liquidus line of the equilibrium ternary U-Zr-O phase diagram, point P in Fig. 7.2) takes place. The description of this process within the 2-d model is based on the self-consistent consideration of the mass balance equations in the melt for each component (O, U, Zr) along with the flux matches at the vertical and horizontal interfaces.

Mass balances of the different components (O, U, Zr):

$$\frac{\partial\left[c_O(B)\pi R^2(h+H)\right]}{\partial t} = \rho_O(I)\left[2\pi R(h+H)\frac{\partial R}{\partial t} + \pi R^2\frac{\partial h}{\partial t}\right] + D_O^{UO_2}\frac{\partial \rho_O}{\partial r}\bigg|_I \left[2\pi R(h+H) + \pi R^2\right], \tag{2}$$

$$\frac{\partial\left[c_U(B)\pi R^2(h+H)\right]}{\partial t} = \rho_U(I)\left[2\pi R(h+H)\frac{\partial R}{\partial t} + \pi R^2\frac{\partial h}{\partial t}\right], \tag{3}$$

$$\frac{\partial\left[c_{Zr}(B)\pi R^2(h+H)\right]}{\partial t} = 0. \tag{4}$$

where $c_i(I)$, $c_i(B)$ are the molar densities (mol/cm^3) of the different components (i = O, U, Zr) at the interface boundary and in the bulk of the liquid phase, respectively; $\rho_i(I)$, $\rho_i(B)$ are the corresponding values in the solid phase; $D_O^{(s)}$ is the oxygen chemical diffusion coefficient in the solid phase; R, H and h denote liquid phase linear dimensions, presented in Fig. 7.2.

Vertical interface flux matches:

Oxygen:

$$\left[\rho_O(I_V) - c_O(I_V)\right]\frac{\partial R}{\partial t} = c_O(B)v_R(I_V) + k_O\left[c_O(I_V) - c_O(B)\right] - D_O^{UO_2}\frac{\partial \rho_O}{\partial r}\bigg|_{I_V}, \tag{5}$$

Uranium:

$$\left[\rho_U(B) - c_U(I_V)\right]\frac{\partial R}{\partial t} = c_U(B)v_R(I_V) + k_U\left[c_U(I_V) - c_U(B)\right], \tag{6}$$

Zirconium:

$$[-c_{Zr}(I_V)]\frac{\partial R}{\partial t} = c_{Zr}(B)v_R(I_V) + k_{Zr}[c_{Zr}(I_V) - c_{Zr}(B)] \ , \qquad (7)$$

where k_i is the convective mass transfer coefficients of different components (i = O, U, Zr) in the melt; I_V designates the vertical interface; v_R is the net velocity of the melt near the verical interface.

These equations should be completed by the Stefan-Maxwell equation in the transition layer:

$$k_O[c_O(I_V) - c_O(B)] + k_U[c_U(I_V) - c_U(B)] + k_{Zr}[c_{Zr}(I_V) - c_{Zr}(B)] = 0 \ . \qquad (8)$$

Superposition of Eqs. (5)-(8) yields:

$$\rho_L v_R(I_V) = (\rho_O(I) + \rho_U(B) - \rho_L)\frac{\partial R}{\partial t} + D_O^{UO_2}\frac{\partial \rho_O}{\partial r}\Big|_{I_V} \ . \qquad (9)$$

<u>Horizontal interface flux matches:</u>

Oxygen:

$$[\rho_O(I) - c_O(I_H)]\frac{\partial H}{\partial t} = c_O(B)v_H(I_H) + k_O[c_O(I_H) - c_O(B)] - D_O^{UO_2}\frac{\partial \rho_O}{\partial r}\Big|_{I_H} \ , \qquad (10)$$

Uranium:

$$[\rho_U(B) - c_U(I_H)]\frac{\partial H}{\partial t} = c_U(B)v_H(I_H) + k_U[c_U(I_H) - c_U(B)], \qquad (11)$$

and superposition relationship:

$$\rho_L v_H(I_H) = (\rho_O(I) + \rho_U(B) - \rho_L)\frac{\partial H}{\partial t} + D_O^{UO_2}\frac{\partial \rho_O}{\partial r}\Big|_{I_H} \ . \qquad (12)$$

where I_H designates the bottom (horizontal) interface; v_H is the net velocity of the

melt near the horizontal interface.

7.2.2. Precipitation stage

For the theoretical description of the precipitation stage the model self-consistently accounts for three simultaneous processes: (1) dissolution of UO_2 crucible by the liquid phase; (2) formation and growing of ceramic $(U,Zr)O_{2-x}$ precipitates; (3) diffusion transport of oxygen from UO_2 to the liquid. As demonstrated in [11,12], the last process is especially important since after completion of the saturation stage the oxygen diffusion in the solid UO_2 phase determines the kinetics of both processes of the UO_2 dissolution and the formation of $(U,Zr)O_{2-x}$ precipitates, which for this reason obey a parabolic time law ($\propto t^{1/2}$) in the precipitation stage.

The system of mass balance equations of different elements (O, U, Zr) in the homogeneously mixed liquid phase (containing ceramic precipitates) initially proposed in [11,12], has the general form:

$$-\partial/\partial t\,(\rho_U \alpha V) = \partial/\partial t\,[c_{Zr}(W-V+\Phi)], \tag{13}$$

$$-\partial/\partial t\,[\rho_U(1-\alpha)V] + \partial/\partial t\,(\rho_U W) = \partial/\partial t\,[c_U(W-V+\Phi)], \tag{14}$$

$$\partial/\partial t\,(\rho_0 W) - \partial/\partial t\,(\rho_0 V) - D_O^{(s)}\partial\rho_O/\partial x|_l\, S = \partial/\partial t\,[c_O(W-V+\Phi)], \tag{15}$$

where the parameter α describes the composition of the ceramic precipitates $(U_{1-\alpha}, Zr_\alpha)O_{2-x}$, V is defined as the integral volume of this precipitated phase, $(W+\Phi)$ is the integral volume occupied by the melt (containing the precipitates), Φ is the fraction of this volume connected with the expansion of the melt (see Fig. 6 in [11]).

The system of Eqs. (13)-(15) should be generally completed by the flux match conditions at the solid/liquid interface for the self-consistent description of the dissolution process. However, the formation of the two-phase zone (liquid + ceramic precipitates) near the interface makes this problem especially complicated. In [11,12] a general approach for the description of mass transfer through the two-phase zone was formulated. However, lacking additional experimental data necessary for the development of the complete model, the authors used a simplified approach. Instead of the flux match equations, it was proposed to use additional simple assumptions based on the experimental observations which allowed the solution of the incomplete system of mass balance equations (13)-(15). In [11] such an assumption was $\alpha \approx$ const., which corresponded to the invariable composition of the ceramic phase $(U_{1-\alpha}, Zr_\alpha)O_{2-x}$ formed during the precipitation stage. This assumption was in fair agreement with observations either of Hofmann et al. [3] or Kim [5].

As demonstrated in [12], for the description of the crucible tests [4] at 2000°C such a model predicts a rather slow rate of the UO_2 crucible walls dissolution (which was really observed at this temperature in [4]), thus, for this particular test series this additional condition $\alpha \approx$ const. can be substituted with a satisfactory accuracy by the condition $\partial W/\partial t \approx 0$. Namely this assumption was made in the paper of Olander [13]. However, this solution was in direct contradiction with observations at higher

temperatures 2100-2200°C either of Hofmann [3] or Kim and Olander [4,5], and for this reason, the model [13] was not applied for the description of high temperature tests of Kim and Olander [4].

An additional post-test EDX analysis of some of the samples obtained in the new test series at 2100°C (Section 3) revealed that among ceramic particles in the melt with the composition presented in Table 3.5 (and apparently formed on cool down), there exist also other particles with the composition corresponding to $\alpha \approx 0.25\text{-}0.35$. It was assumed that namely these particles were formed at temperature and, for this reason, the value of the model parameter α in this test series was searched in the vicinity of the above indicated interval. For the other tests this parameter was searched by fitting of the model calculations to the measured data.

7.2.3. Verification of the model parameters

Specification of the model parameters was performed on the base of the model validation against the previous AECL tests with smaller crucibles at T = 2373 K and 2473 K [9] (see Fig. 7.3). At temperature T=2000°C the model was verified against experiments performed by different groups [5,6,7] on dissolution of the UO_2 crucibles by molten Zircaloy. The uranium saturation concentration in the melt attained in the end of the saturation stage was different in these tests owing to the different dimensions of the UO_2 crucibles and Zry charges, and the model reproduced these data satisfactory (see Fig. 1.3). Further correlation was made between the numerical model and experimental results [6,7] at temperatures T=2100 °C and 2200 °C. In the tests [6,7] two sets of experimental data on UO_2/Zry and UO_2/(Zry/25at.%O) interactions under identical conditions were presented. These data give an opportunity, at first to choose the position of the liquidus line at T=2373K and 2473K (from the first set of the experiments, with pure Zry), and then to perform on this basis the validation of the numerical model for the pre-oxidised charge (Zry with 25at.%O) using derived parameters of the liquidus line in a small vicinity of the intersection point P in Fig. 7.2. Numerical results obtained in such a way were in a good agreement with the experimental data (Fig. 7.3).

Subsequent calculations and analyses of the new experimental data were carried out without any additional fitting of the parameters.

7.3. Model predictions

The calculation scheme and numerical algorithms of the simplified model [11,12] were generalised and applied for the solution of the present 2-d model.

Based on the above-described new 2-d model, the new results can be interpreted as follows:

In the new tests with large crucibles, the model predicts the same level of melt saturation during the initial 200-300 s (the saturation period) as in the small crucible tests [6]. These saturation levels are ≈ 50 wt.% U at 2100°C and ≈ 71 wt.% U at 2200°C. In the large crucible tests, however, dissolution of the crucible walls is predicted to continue during the subsequent 100 - 200 s (the precipitation period), until the oxygen diffusion flux from the crucible walls is sustained. In the tests without bottom isolation (i.e., with no yttria discs), the uranium melt concentration will increase during the precipitation period by 6-8 wt.% at 2100°C (Fig. 7.4) and by 3-4 wt.% at 2200°C (Fig. 7.5a), giving final concentrations of ≈ 57 wt.% U and ≈ 74 wt.% U, respectively.

In the new 2200°C test series with bottom isolation (i.e., with yttria discs), the maximum uranium melt concentration of 74 wt.% is predicted to occur after 300 - 400 s (Fig. 7.5b). However, this time is within the duration of the saturation period, because the time for saturation to occur is extended by the higher melt *S/V* (surface to volume) ratio used in these tests (and practically coincides with the characteristic time of oxygen diffusion from the crucible walls). For the same reason (higher *S/V* ratio), the saturation level reached in the tests with yttria discs would be ≈ 74 wt.% U, i.e., 3-4 wt.% higher than the saturation level reached in the tests without yttria discs (≈71 wt.%). This level would be very close to the maximum U content attained in tests without yttria discs at the end of the saturation + precipitation periods (Fig. 7.5a).

Calculation results for the wall dissolution depth in the various tests (Fig. 7.6) are in a reasonable agreement with the results of the post-test image analysis of the crucible cross-section photographs performed in the FZKA (see Tables 3.4, 4.4. and 5.4).

Since crucibles have rather thick UO_2 bottom (≈ 10 mm), oxygen diffusion from the bottom is continued after ≈ 400 s during the subsequent ≈ 1200 s. Being exhausted with oxygen, the crucible walls will not be dissolved during this time interval. However, owing to continuous oxygen supply from the interior of the bottom into the melt, precipitation process in the melt will be continued during this time interval (in accordance with observations).

After successful verification of the model against the new test data, it was applied to the prediction of the fuel pellet dissolution in the real fuel rod configuration with various melt thickness and melt oxygen concentrations. Results of the calculations are presented in Fig. 7.7.

7.4. Modelling conclusions

It can be generally concluded that, depending on the test conditions and the melt/crucible geometry, dissolution of the crucible walls can continue during one or two periods.

Dissolution of the UO_2 crucible by molten Zry in the new AECL tests continued during two stages and was satisfactory simulated by the new 2-d model (developed during the Programme).

The major part of a crucible was dissolved during the first, saturation stage. In this stage dissolution occurred with high rates until melt saturation was reached.

The minor part of a crucible was dissolved during the second, precipitation stage. In this stage dissolution occurred with slow rates and was accompanied with the ceramic phase precipitation. However, the amount of dissolution during the second period was not so significant as assumed in the beginning of the Programme.

These conclusions cannot be directly applied to the description of fuel dissolution under real accident conditions, because the influence of dissolved oxygen in the Zircaloy melt on the rate and saturation level of uranium has not been studied experimentally in the current Programme. Thus, the current model needs to be extended to include this phenomenon, as well as simultaneous dissolution phenomena.

8. Modelling of the scoping tests on simultaneous dissolution of UO_2 and ZrO_2 by molten Zircaloy

In the final period of the Project the six scoping tests were performed by AECL at 2100°C to study the simultaneous dissolution of UO_2 and ZrO_2 in molten Zircaloy. Results of the post-test analyses of the interaction system presented in Section 6, are theoretically analysed by the simplified 1-d model initially proposed in the authors' paper [27] .

8.1. Pre-test analysis

On the base of the UO_2 dissolution tests analysed in the previous Section 7, it was concluded that, depending on the test conditions and the melt/crucible geometry, dissolution of the crucible walls could continue during the second, precipitation period. However, the amount of dissolution during this period was not so significant (in comparison with the first, saturation period) as assumed in the beginning of the Programme. Moreover, on the base of the previously published AECL data [6,7] which demonstrated that the extent of fuel dissolution could be significantly lower in oxygenated Zircaloy melts (see Fig. 7.3), it was assumed that the final U melt content should be significantly lower in the new tests (with ZrO_2 cylinder inside the UO_2 crucible) in comparison with pure UO_2 crucible tests. On the other hand, it was also assumed that the crucible bottom isolation with the yttria disc can somewhat reduce the oxygen diffusion flux from the crucible and thus increase the final U content in the melt (see Section 6.7). However, as shown above in Section 7.3, this effect is rather small and can increase the U melt content only by a few percent (compare Figs. 7.5a and 7.5b). For the same reason (the increased amount of oxygen in the melt), it was expected that UO_2 dissolution in the second, precipitation period might be completely suppressed.

Therefore, results of the new tests on simultaneous dissolution of UO_2 crucible and ZrO_2 cylinder were rather surprising, since the final U melt content in these tests was significantly higher (≈ 63 wt.%) than in the previous tests without ziconia cylinder at the same temperature 2100°C (≈ 56 wt.%).

On the other hand, the amount of ZrO_2 dissolved in these new tests was also significantly higher in comparison with the previous AECL [25] and FZKA [26] tests on ZrO_2 crucible dissolution. Indeed, in the new tests a complete dissolution of the zirconia cylinder with 6.5 mm diameter was observed within the first ≈ 200 s, whereas only a very thin layer (less than 1 mm) of the ZrO_2 crucible was dissolved in the previous tests. Correspondingly, the ratio of crucible-derived Zr in the melt to the total melt Zr content, $Zr_{crucible}/Zr_{total}$, was ≈ 0.25 in the new tests and less than 0.1 in the previous AECL tests [25].

Therefore, one can conclude that dissolution rates and amounts of both ceramic materials UO_2 and ZrO_2 were significantly higher in the tests with simultaneous dissolution of UO_2 and ZrO_2, in comparison with the tests where these materials were dissolved separately. This conclusion is very important from the point of view of the model application to the real accident conditions.

8.2. Post-test analysis

Post-test calculations of the simultaneous dissolution by molten Zry of the UO_2 and ZrO_2 oxides observed at T=2100 °C in the new AECL/FZKA scoping tests (Section 6) are performed by the model developed in the authors' paper [27] and updated in

accordance with the new test data. Parameters of the UO_2 crucible and ZrO_2 cylinder are fixed in accordance with the AECL/FZKA test design.

A simplified 1-d model developed by generalisation of the two dissolution (UO_2 and ZrO_2) models, qualitatively correctly simulates the main features observed in the scoping tests on simultaneous dissolution of UO_2 and ZrO_2 by molten Zry.

The model predicts that the mass transfer mechanism in the liquid phase is afforded by the natural convection in the melt and, for this reason, the two problems of the UO_2 and ZrO_2 dissolution by the same melt cannot be separated from each other and described by the independent dissolution models.

In particular, the model predicts that a strong convective stirring induced by the heavy U atoms in the melt can significantly increase mass transfer from the ZrO_2 wall and, thus, its dissolution rate and depth. This qualitative conclusion was confirmed by the results of the scoping tests on simultaneous dissolution of UO_2 and ZrO_2. Indeed, model calculations with a small oxygen mass transfer coefficient from the ZrO_2 wall to the melt ($\sim 10^{-3}$ cm/s, typical for the ZrO_2 crucible dissolution tests, [20]) predict only partial dissolution of the ZrO_2 cylinder, whereas the increase of this coefficient to the value $\sim 10^{-2}$ cm/s (typical for the UO_2 crucible dissolution tests) allows correct prediction of complete dissolution of the ZrO_2 cylinder within $\approx$ 200 s, in agreement with observations (Fig. 8.1).

After completion of the ZrO_2 dissolution (during the first $\approx$ 200 s), a comparison of the model predictions with measurements becomes more straightforward, since a sole process of UO_2 dissolution (well studied in the previous test series and satisfactorily described by the developed model) should be considered in the subsequent period of time. It is interesting to note that this initial time period (200 s) practically coincides with the calculated duration of the first, saturation period when the melt attains its saturation limit. Owing to an excessive amount of oxygen in the melt (delivered by the dissolved ZrO_2 cylinder), the saturation limit of U melt content is calculated as $\approx$ 40 wt.% , i.e. significantly reduced in comparison with $\approx$ 50 wt.% attained during the saturation period in the UO_2 dissolution tests (without cylinder) at the same temperature 2100°C (Section 3). As mentioned above, before the test conductance it was expected that the UO_2 dissolution would be strongly suppressed during the second, precipitation stage and thus the value of $\approx$ 40 wt.% for the U melt content would be the final one. However, in reality a rather strong crucible wall dissolution was observed during the subsequent 200 s, resulting in a rather high U content $\approx$ 63 wt.% in the melt. This value is noticeably higher than $\approx$ 56 wt.% attained in the pure UO_2 dissolution tests and, thus, can be explained only in one way, assuming continuous vigorous wall dissolution during the second, precipitation stage.

In order to check this important statement, an additional calculation was performed under a conservative assumption that the real temperature was 50 K higher (i.e. 2423 K) than that measured in the experiment (note that the experimental estimation of the temperature measurement accuracy was within $\pm$ 30 K). Even in this case a new saturation limit $\approx$ 53 wt.% (Fig. 8.2) was too small in comparison with the measured value $\approx$ 63 wt.%, confirming the existence of a strong dissolution during the subsequent precipitation stage. Finally, it was checked that only the temperature measurement error of 100 K can explain the attainment of the saturation limit of $\approx$ 63 wt.% during the first, saturation period (Fig. 8.2), however, such an error

is too large (in comparison with the measurement accuracy ± 30 K) and thus non-realistic.

In order to describe the observed increase of the U melt content from 40 to 63 wt.% during the precipitation period, the value of the model default parameter α (determining the U/Zr ratio in the ceramic $(U_{1-\alpha},Zr_{\alpha})O_{2-x}$ precipitates formed at temperature) was fitted as 0.07, in a reasonable agreement with composition of the U-rich ceramic precipitates observed in the post-test examinations. However, such a coincidence might be occasional, since the precipitates formed at temperature are usually hardly detected (as in the previous tests) among precipitates formed on cool-down (and probably are changing their composition during cool-down of the melt). Results of the model calculations and their comparison with the measurements are presented in Fig. 8.3.

8.3. Modelling conclusions

Dissolution rates and amounts of both ceramic materials UO_2 and ZrO_2 are significantly higher in the tests with simultaneous dissolution of UO_2 and ZrO_2, in comparison with the previous tests where these materials were dissolved separately.

The increase of ZrO_2 dissolution is mainly connected with the enhanced convective stirring of the melt induced by the dissolved heavy U atoms, leading to the complete dissolution of a thick zirconia cylinder within 200 s.

The increase of UO_2 dissolution is connected with a well pronounced precipitation stage, which occurs during the subsequent 200 s and provides a substantial increase of the U melt content from 40 to 63 wt.%. An alternative explanation of such a high final U melt content might be associated with the temperature measurement error, which in this case, however, should attain 100 K (instead of experimentally estimated value of ±30 K), apparently making this explanation non-realistic.

The model of UO_2 dissolution developed within the 4th Framework Programme allows an exhaustive explanation and satisfactory description of the crucible wall dissolution observed after complete dissolution of the zirconia cylinder (i.e. during the second, precipitation period).

The first, saturation stage of the simultaneous dissolution process can be qualitatively correctly analysed by the simplified 1-d model developed by generalisation of the two dissolution (UO_2 and ZrO_2) models. However, a comprehensive quantitative description can be obtained only on the basis of detailed studies of the complicated phenomenon of simultaneous dissolution and development of a more realistic and advanced model (foreseen in the 5th Framework Programme).

9. General conclusions

This reports describes the procedures and results from different isothermal heating tests:

(i) UO_2 crucible dissolution tests at 2100 and 2200°C and reaction times up to 30 min.,

(ii) additional tests at 2200°C where the crucible-cavity bottom was isolated from the reaction by an yttria disc, and

(iii) scoping tests involving simultaneous dissolution of UO_2 and ZrO_2.

Each post-test specimen was sectioned and examined by various methods: ICP

spectrometry, SEM/EDX, optical microscopy and computer image analysis of microphotographs, which allowed qualitative and quantitative evaluation of the UO_2 dissolution phenomenon.

Main test results are:

- The dissolution of UO_2 takes place in two stages: a first short saturation period with a rapid dissolution and a second period during which there is a slower UO_2 dissolution accompanied by precipitation of a ceramic (U, Zr)O_{2-x} phase in the saturated melt.
- The main cause of the discrepancy amongst the previous results was connected with different UO_2 crucible sizes (wall thickness), UO_2/Zry mass ratios and melt surface to volume ratios (S/V) which influence the oxygen diffusion from crucible walls to the melt.
- Scoping tests on simultaneous UO_2/ZrO_2 dissolution by molten Zry were carried out for comparison with separate UO_2 and ZrO_2 dissolution tests. They show a faster ZrO_2 dissolution rate and a larger extent of UO_2 and ZrO_2 dissolution than expected from separate dissolution tests. This could have an important bearing on clad failure.

The newly developed 2-d model explains the disagreement observed in previous results with small crucibles and reproduces correctly the new AECL/FZKA tests with large crucibles:

- The UO_2 dissolution model confirms that most of the UO_2 liquefaction occurs rapidly (~250/350s) in the 1st saturation phase up to the saturation of the melt given by the liquidus line at given temperature. This confirms that this liquidus line can limit with a certain accuracy the UO_2 dissolution in SA codes. Minor dissolution occurs during the 2nd precipitation phase, however, it can significantly increase under more realistic conditions of simultaneous UO_2 and ZrO_2 dissolution.
- Tests on simultaneous UO_2 and ZrO_2 dissolution show a large increase of ZrO_2 dissolution rate and extent due to enhanced convective stirring of the melt in the presence of UO_2. A large increase of the UO_2 dissolution occurs due to a well pronounced precipitation stage in the presence of ZrO_2.

Acknowledgements

This report was prepared for the Commission of the European Communities within the 4th Framework Programme on Nuclear Fission Safety in part-fulfillment of Contract Number FI4S-CT96-0032 (Corium Interactions and Thermochemistry).

Financial support from the CANDU Owners Group, consisting of AECL, Ontario Hydro, Hydro-Quebec and NB Power, is gratefully acknowledged.

References:

1. W.Dienst, P.Hofmann and D.Kerwin-Peck, Nucl.Technol.65(1984)109.
2. P.Hofmann, H.Uetsuka, A.N.Wilhelm and E.A.Garcia, Proc.Int.Symp. on Severe Accidents in Nuclear Power Plants, Sorrento, Italy, March 21-25, 1988, IEAE-SM-296/1, p.3.
3. P.Hofmann, Ch.Adelhelm, H.Uetsuka, H.Zimmermann, J.Burbach, G.Gausmann, D.Kempf, K.Kurz, H.Metzger, G.Streib, Projekt Nukleare Sicherheit, Jahresbericht 1985, KfK 4000(1986)4200-56.
4. K.T.Kim and D.R.Olander, J.Nucl.Mater. 154(1988)85, 102.
5. K.T.Kim, UO_2 dissolution by molten Zircaloy, Thesis (University of California, Berkeley), 1988
6. P.J.Hayward and I.M.George, J.Nucl.Mater. 208(1994)35, 43.
7. P.J.Hayward and I.M.George, J.Nucl.Mater. 232(1996)1, 13.
8. A.Wilhelm and E.Garcia, J.Nucl.Mater. 158(1988)143.
9. M.S.Veshchunov and A.M.Volchek, J.Nucl.Mater. 188(1992)177.
10. D.R.Olander, Materials-Chemistry and Transport Modeling for Severe Accident Analysis in Light-Water Reactors, Lawrence Berkeley Laboratory Report LBL-32530 (1992).
11. M.S.Veshchunov and P.Hofmann, J.Nucl.Mater. 209(1994)27.
12. M.S.Veshchunov, P.Hofmann, A.V.Berdyshev, Critical evaluation of UO_2 dissolution by molten Zircaloy in different crucible tests, - J.Nucl.Mater., 1996, v.231, p.1-19.
13. D.R.Olander, J.Nucl.Mater. 224(1995)254.
14. P.J.Hayward, I.M.George, L.C.Brown and K.Wasney, 1st Interim Report, 1997 May, unpublished.
15. P.J.Hayward, I.M.George, L.C.Brown and K.Wasney, 2nd Interim Report, 1997 November, unpublished.
16. P.J.Hayward, I.M.George, L.C.Brown and K.Wasney, 3rd Interim Report, 1998 May, unpublished.
17. P.J.Hayward, I.M.George, L.C.Brown and R. Herman, 4rth Interim Report, 1998 December, unpublished.
18. P.J.Hayward, Final Report, 1999 March, unpublished.
19. P. Hofmann, J. Stuckert, Experimente zur UO_2 und ZrO_2-Auflösung durch geschmolzenes Zircaloy, Projekt Nukleare Sicherheit, Jahresbericht FZKA 5963, 1996, s.393-397
20. A.V.Berdyshev, M.S.Veshchunov, 1st Interim Report, 1997 May, unpublished.
21. A.V.Berdyshev, M.S.Veshchunov, 2nd Interim Report, 1997 December, unpublished.
22. A.V.Berdyshev, M.S.Veshchunov, 3rd Interim Report, 1998 June, unpublished.
23. A.V.Berdyshev, M.S.Veshchunov, 4th Interim Report, 1998 December, unpublished.
24. A.V.Berdyshev, A.V.Boldyrev and M.S.Veshchunov, 5th Interim Report, 1999 June, unpublished.

25. P.J. Hayward and I.M. George, Dissolution of ZrO_2 in Molten Zry-4, - J.Nucl.Mater., 265(1999)69.

26. P.Hofmann, J.Stuckert, Final Report, INV-CIT(98)-P026, 1999 June, unpublished.

27. M.S.Veshchunov, A.V.Berdyshev, Modeling of chemical interactions of fuel rod materials at high temperatures. Part 1: Simultaneous dissolution of UO_2 and ZrO_2 by molten Zircaloy in an oxidizing atmosphere, - J.Nucl.Mater., 252(1997)98.

Appendix 1

Evaluation of the molar density of the melt

Sample Number	time s	V_{Zr} cm^3	M_{Zr} mol	α =U/(U+Zr)	M_U mol	V_S cm^3	V_B+V_W cm^3	V_H cm^3	V_L $= V_S+V_H$	ρ_L (mol/cm^3) $\Theta = 1$	ρ_L (mol/cm^3) $\Theta = 0$
HF-24	150	1.343	0.086	0.448	0.069	1.86	1.26	2.43	4.29	0.068	0.036
HF-27	216	1.342	0.085	0.481	0.079	2.14	1.98	2.59	4.73	0.068	0.035
HF-29	324	1.346	0.086	0.527	0.096	2.59	2.83	2.81	5.4	0.069	0.034
HF-22	433	1.335	0.085	0.524	0.094	2.54	2.45	2.77	5.31	0.069	0.034
HF-21	612	1.354	0.086	0.509	0.090	2.43	2.35	2.62	5.05	0.070	0.035
HF-20	613	1.360	0.087	0.521	0.094	2.54	2.39	2.92	5.46	0.068	0.033

V_{Zr} *(cm^3),* - volume of the molten Zr sample.

M_{Zr} *(moles),* - number of Zr atoms in the melt: $M_{Zr} \approx \rho_{Zr}\,(mol/cm^3) \times V_{Zr}$

$\approx 0.064 \times V_{Zr}$.

α = U/(U+Zr) *mol.% ratio* (measured, see Table 5.3).

M_U *(moles),* - number of dissolved U atoms: $M_U = M_{Zr} \times \alpha/(1-\alpha)$.

V_S *(cm^3),* - volume of the dissolved crucible: $V_S = M_U/\rho_{UO2}\,(mol/cm^3)$

$\approx M_U/0.037$ (for the used crucibles with ≈ 80 % of theoretical density),

$V_S \approx V_B + V_W$ (Table 5.4).

V_H *(cm^3),* - melt volume without account of dissolved crucible space (measured, see Table 5.4).

$V_L = V_S + V_H$, - total volume of the melt.

$M_{U(O)}$ *(mol),* - number of dissolved atoms U(O):

$M_U \approx \rho_{UO2}\,(mol/cm^3) \times V_S \approx 0.037 \times V_S$,

$M_O \approx 2 \times \rho_{UO2}\,(mol/cm^3) \times V_S \approx 2 \times 0.037 \times V_S$.

ρ_L - molar density of the melt: $\rho_L = c_{U+}\,c_{Zr} + \Theta c_O \approx$ const.

$\rho_L \approx 0.064$ (mol/cm^3), for pure Zr melt;

$\rho_L \approx 0.071$ (mol/cm^3), for pure U melt.

$M_L = M_{Zr} + M_U + \Theta M_O$, - «effective» number of atoms in the melt.

$\rho_L\,(mol/cm^3) = M_L / V_L$.

Conclusion:

Θ =1, $\rho_L \approx const. \approx 0.068$ (mol/cm^3), is a reasonable approximation

TABLE 3.1

PRE-TEST MATERIAL DIMENSIONS AND WEIGHTS

Crucible, Test No.	[1]I.D. (mm)	[2]O.D. (mm)	Height mm	[3]Depth (mm)	Crucible Wt. (g)	Zircaloy Wt. (g)	Mass Ratio
HF-1	16.88	26.91	27.55	16.79	124.806	9.756	12.79
HF-2	16.70	26.87	27.46	16.79	124.834	9.770	12.77
HF-3	16.88	26.94	27.52	16.86	124.693	9.745	12.80
HF-4	16.88	26.86	27.53	16.75	124.542	9.735	12.79
HF-6	16.88	26.89	27.47	16.84	123.907	9.686	12.79
HF-7	16.80	26.87	27.44	16.66	123.467	9.652	12.79
HF-8	16.78	26.91	27.35	16.69	123.402	9.643	12.80
HF-9	16.81	26.86	27.49	16.93	123.311	9.641	12.79
HF-10	16.88	26.87	27.48	16.74	123.855	9.682	12.79
HF-11	16.80	26.87	27.50	16.80	124.737	9.740	12.81
HF-12	16.83	26.85	27.56	16.85	124.272	9.712	12.80
HF-13	16.85	26.85	27.45	16.80	124.434	9.728	12.79

[1]Inner diameter; [2]outer diameter; [3]cavity depth

TABLE 3.2

DISSOLUTION TEST PARAMETERS

Test No.	Target Time, (s)	[1] Discontinuity temp. (^{o}C)	Total time molten (s)	Main part of isotherm
HF-1	900	1919	916	2106 ± 8^{o}C for 795 s
HF-2	1800	1956	1833	2108 ± 20^{o}C for 1757 s
HF-3	1800	2030	1801	2108 ± 10^{o}C for 1685 s
HF-4	1200	1961	1217	2107 ± 11^{o}C for 1128 s
HF-6	120	1812	223	2097 ± 12^{o}C for 72 s
HF-7	360	1930	383	2100 ± 5^{o}C for 180 s
HF-8	600	1980	623	2102 ± 9^{o}C for 595 s
HF-9	600	1958	634	2098 ± 8^{o}C for 417 s
HF-10	1200	1993	1236	2103 ± 11^{o}C for 996 s
HF-11	400	1910	413	2104 ± 11^{o}C for 207 s
HF-12	300	1931	303	2101 ± 21^{o}C for 158 s
HF-13	100	1927	125	2100 ± 21^{o}C for 34 s

[1]Observed in the Zircaloy time/temperature curve from melting and/or emissivity change.

TABLE 3.3

MEAN ICP SPECTROMETRY ANALYSES (± 2SD) FOR THE 2100°C TEST SERIES

Test No.	Melt time (s)	U wt.%	Zr wt.%	Fe wt.%	Cr wt.%	Sn wt.%	*O wt.%	U/(U+Zr) wt.% ratio
HF-13	125	43.62 ± 0.89	47.12 ± 0.58	0.09 ± 0.00	0.05 ± 0.00	0.62 ± 0.02	8.50 ± 1.43	48.07 ± 0.25
HF-6	223	44.60 ± 0.46	48.69 ± 0.08	0.10 ± 0.00	0.05 ± 0.00	0.68 ± 0.06	5.87 ± 0.48	47.80 ± 0.28
HF-12	303	46.24 ± 0.54	43.79 ± 0.37	0.09 ± 0.00	0.04 ± 0.00	0.59 ± 0.01	9.25 ± 0.57	51.36 ± 0.41
HF-7	383	51.72 ± 1.09	39.76 ± 0.59	0.082 ± 0.00	0.043 ± 0.00	0.52 ± 0.03	8.00 ± 1.22	56.54 ± 0.81
HF-11	413	53.40 ± 0.61	36.82 ± 1.69	0.07 ± 0.00	0.03 ± 0.00	0.47 ± 0.02	9.20 ± 2.00	59.19 ± 1.04
HF-8	623	48.84 ± 0.74	42.68 ± 1.59	0.09 ± 0.00	0.05 ± 0.00	0.63 ± 0.03	7.72 ± 1.60	53.37 ± 1.08
HF-9	634	50.41 ± 0.63	40.44 ± 1.12	0.09 ± 0.02	0.05 ± 0.00	0.60 ± 0.15	8.42 ± 1.15	55.49 ± 0.76
HF-1	916	50.41 ± 2.02	40.96 ± 2.30	0.08 ± 0.03	0.04 ± 0.02	0.55 ± 0.14	7.96 ± 1.65	55.17 ± 2.23
HF-4	1217	51.07 ± 1.87	40.35 ± 1.21	0.08 ± 0.01	0.04 ± 0.01	0.55 ± 0.10	7.90 ± 1.43	55.86 ± 1.48
HF-10	1236	53.11 ± 1.22	37.82 ± 2.13	0.08 ± 0.00	0.04 ± 0.00	0.59 ± 0.08	8.36 ± 1.61	58.41 ± 1.77
HF-3	1801	52.60 ± 3.17	38.10 ± 2.06	0.08 ± 0.01	0.04 ± 0.01	0.49 ± 0.10	8.71 ± 1.75	57.99 ± 2.68
HF-2	1833	48.02 ± 0.25	42.42 ± 0.03	0.09 ± 0.01	0.04 ± 0.00	0.58 ± 0.07	8.85 ± 0.18	53.10 ± 0.13

* O values by difference

TABLE 3.4

IMAGE ANALYSIS RESULTS FOR THE 2100°C TEST SERIES

Test No	Wall dissolution mm^3	Bottom dissolution mm^3	V_{diss}/V_{Zry}	Cruc. wall thickness µm	H_{diss}/h_{Zry}	O_{dif}/O_{melt} %
HF-13	784	164	0.57	3831	1.67	31
HF-6	481	170	0.39	4236	1.51	18
HF-12	766	153	0.55	3947	1.72	38
HF-7	846	179	0.61	3760	1.69	24
HF-11	1232	270	0.89	3531	1.86	22
HF-8	804	164	0.58	3970	1.68	23
HF-9	799	217	0.61	3977	1.76	28
HF-1	971	264	0.74	3726	1.77	16
HF-4	792	215	0.61	3905	1.72	23
HF-10	1021	247	0.76	3636	1.75	19
HF-3	890	239	0.68	3843	1.75	27
HF-2	763	199	0.58	3993	1.64	34

TABLE 3.5

MEAN PHASE COMPOSITIONS FROM EDX ANALYSES
OF CERAMIC, ZR-ALLOY AND U-ALLOY PHASES,

Test, (time, s)	$(U_xZr_y)O_z$ stoichiometry ± 2SD			Zr-alloy composition (atom %) ± 2SD			
	x	y	Z	Zr	Sn	U	O
HF-13 (125 s)	0.93 ± 0.02	0.07 ± 0.02	1.56 ± 0.21	72.1 ± 4.3	0.7 ± 0.7	0.8 ± 0.5	26.3 ± 4.4
HF-6 (223 s)	0.94 ± 0.02	0.06 ± 0.02	1.63 ± 0.33	71.6 ± 3.2	0.5 ± 0.4	0.8 ± 0.8	27.1 ± 3.2
HF-12 (303 s)	0.92 ± 0.04	0.08 ± 0.04	1.53 ± 0.22	74.4 ± 5.1	0.7 ± 0.7	0.8 ± 0.4	24.2 ± 5.4
HF-7 (383 s)	0.92 ± 0.03	0.08 ± 0.03	1.40 ± 0.11	67.2 ± 2.2	0.7 ± 0.7	1.0 ± 0.6	31.1 ± 2.3
HF-11 (413 s)	0.88 ± 0.09	0.12 ± 0.09	1.69 ± 0.27	70.5 ± 3.3	0.6 ± 0.7	1.1 ± 1.6	27.7 ± 2.7
HF-8 (623 s)	0.83 ± 0.05	0.17 ± 0.05	1.69 ± 0.10	68.0 ± 1.8	0.6 ± 0.3	0.8 ± 0.7	30.6 ± 1.7
*HF-9 (634 s)	0.82 ± 0.06	0.18 ± 0.06	1.88 ± 0.34	68.5 ± 9.3	0.7 ± 0.8	1.0 ± 0.6	29.9 ± 10.1
HF-1 (916 s)	0.79 ± 0.08	0.21 ± 0.08	1.65 ± 0.23	67.6 ± 3.4	0.7 ± 0.7	1.0 ± 0.8	30.8 ± 3.6
*HF-4 (1217 s)	0.79 ± 0.04	0.21 ± 0.04	1.80 ± 0.35	73.6 ± 12.6	1.1 ± 1.0	1.2 ± 0.7	24.0 ± 14.0
HF-10 (1236 s)	0.74 ± 0.14	0.30 ± 0.14	1.66 ± 0.13	74.9 ± 3.2	0.3 ± 0.2	0.4 ± 0.2	24.4 ± 3.2
HF-3 (1801 s)	0.76 ± 0.06	0.24 ± 0.06	1.87 ± 0.14	66.3 ± 3.9	0.6 ± 0.5	0.9 ± 1.8	32.2 ± 4.0
*HF-2 (1833 s)	0.72 ± 0.09	0.28 ± 0.09	1.94 ± 0.17	68.3 ± 7.7	0.5 ± 0.8	1.0 ± 1.1	30.2 ± 7.7

Test (Time, s)	U-alloy composition (atom %) ± 2SD			
	Zr at.%	Sn at.%	U at.%	O at.%
HF-13 (125 s)	1.93 ± 1.50	0.09 ± 0.49	67.41 ± 9.06	31.28 ± 9.34
*HF-6 (223 s)	2.27 ± 1.57	0.00 ± 0.00	84.25 ± 12.43	13.48 ± 12.75
HF-12 (303 s)	2.58 ± 2.85	0.33 ± 0.63	66.05 ± 13.93	31.17 ± 14.11

SD = standard deviation. All analyses made with the Link-Isis EDX system, except for those marked *, which were made with the TN-2000 EDX system.

TABLE 3.6

SUMMARY OF MEAN PHASE AREA ANALYSES FOR THE 2100°C MELTS

Test (time)	Mean Area % ± 2SD		
	U(O) Alloy	$(U,Zr)O_{2-x}$	Zr(O) Alloy
HF-13 (125 s)	5.8 ± 0.9	23.4 ± 7.0	70.8 ± 7.3
HF-6 (223 s)	4.5 ± 1.7	28.6 ± 5.0	66.9 ± 5.2
HF-12 (303 s)	2.8 ± 0.9	32.2 ± 6.8	65.0 ± 6.3
HF-7 (383 s)	2.6 ± 1.3	37.7 ± 7.6	59.7 ± 6.5
HF-11 (413 s)	2.0 ± 1.6	45.5 ± 2.0	52.5 ± 1.2
HF-8 (623 s)	1.8 ± 1.6	41.1 ± 6.0	57.1 ± 5.5
HF-9 (634 s)	3.2 ± 3.8	41.4 ± 4.6	55.3 ± 3.4
HF-1 (916 s)	1.7 ± 1.1	45.1 ± 10.4	53.2 ± 9.6
HF-4 (1217 s)	1.1 ± 0.9	52.2 ± 16.8	46.7 ± 16.7
HF-10 (1236 s)	0.8 ± 0.2	50.8 ± 4.0	48.4 ± 3.8
HF-3 (1801 s)	1.2 ± 0.8	53.2 ± 14.3	45.6 ± 14.5
HF-2 (1833 s)	3.3 ± 3.6	49.1 ± 14.2	47.6 ± 11.9

TABLE 4.1

MATERIAL DIMENSIONS AND WEIGHTS, 2200°C TESTS WITH BOTTOM ISOLATION

Crucible, Test No.	[1]I.D. (mm)	[2]O.D. (mm)	Height mm	[3]Depth (mm)	Post-Test O.D. (mm)	Crucible Wt. (g)	Zircaloy Wt. (g)	Mass Ratio
HF-15	16.70	26.83	27.44	16.87	[4]n.m.	124.923	6.941	18.00
HF-17	16.82	26.88	27.41	16.72	n.m.	124.154	6.900	17.99
HF-18	16.86	26.84	27.45	16.82	n.m.	123.638	6.855	18.04
HF-19	16.79	26.84	27.44	16.95	n.m.	123.639	6.856	18.03
*HF-26	16.86	27.47	27.43	16.60	n.m.	123.814	6.911	17.92
*HF-30	16.85	26.89	27.48	16.56	26.70	123.863	6.889	17.98

[1]Inner diameter; [2]outer diameter; [3]cavity depth, [4]not measured. * Failed tests.

TABLE 4.2

DISSOLUTION TEST PARAMETERS, 2200°C TESTS WITH BOTTOM ISOLATION

Test No.	Target Time (s)	[1] Discontinuity temp. (°C)	Total time Molten (s)	Main part of isotherm
HF-15	400	1869	428	2202 ± 6°C for 217 s
HF-17	200	1869	213	2199 ± 6°C for 25 s
HF-18	300	2019	339	2205 ± 11°C for 164 s
HF-19	100	2034	138	2200 ± 3°C for 4 s
HF-26	800	1908	*854	2199 ± 9°C for 673 s
HF-30	800	1966	*610	peak artifacts (see text)

[1]Observed in the Zircaloy time/temperature curve from melting and/or emissivity change.
*Estimated from the time/temperature traces for the failed tests.

TABLE 4.3

MEAN ICP RESULTS (± 2SD) FOR 2200°C MELTS WITH BOTTOM ISOLATION

Test Number	Melt time (s)	U wt.%	Zr wt.%	Fe wt.%	Cr wt.%	Sn wt.%	Y wt.%	[1]O wt.%	U/(U+Zr) wt.% ratio
HF-19	138	53.17 ± 1.17	38.38 ± 0.98	0.09 ± 0.01	0.05 ± 0.00	0.64 ± 0.04	0.14 ± 0.22	7.53 ± 1.08	58.08 ± 1.05
HF-17	213	56.98 ± 1.63	33.25 ± 0.43	0.09 ± 0.00	0.04 ± 0.00	0.58 ± 0.03	0.08 ± 0.04	8.98 ± 1.44	63.15 ± 0.84
HF-18	339	65.42 ± 0.88	24.55 ± 0.17	0.06 ± 0.00	0.03 ± 0.00	0.41 ± 0.02	0.07 ± 0.01	9.47 ± 0.69	72.71 ± 0.40
HF-15	428	66.33 ± 1.29	22.44 ± 1.02	0.05 ± 0.01	0.02 ± 0.00	0.37 ± 0.04	0.05 ± 0.03	10.74 ± 1.55	74.72 ± 0.98
*HF-30	610	63.75 ± 0.14	21.90 ± 0.85	0.04 ± 0.01	0.02 ± 0.00	0.30 ± 0.03	0.13 ± 0.02	13.86 ± 0.73	74.43 ± 0.78
*HF-26	853	62.55 ± 0.14	23.00 ± 0.28	0.04 ± 0.00	0.02 ± 0.00	0.31 ± 0.03	0.15 ± 0.05	13.93 ± 0.12	73.12 ± 0.12

*Failed tests, melt times estimated from the time/temperature traces.
[1]O values by difference.

TABLE 4.4

IMAGE ANALYSIS RESULTS FOR 2200°C MELTS WITH BOTTOM ISOLATION

Test No	Wall dissolution mm^3	Bottom dissolution mm^3	V_{diss}/V_{Zry}	Cruc. wall thickness µm	H_{diss}/h_{Zry}	O_{dif}/O_{melt} %
HF-19	970	-	0.82	3555	2.12	6
HF-17	1237	-	1.04	3282	2.22	15
HF-18	1785	-	1.51	2725	2.44	9
HF-15	1969	-	1.65	2572	2.37	19

TABLE 4.5

MEAN PHASE COMPOSITIONS IN 2200°C TEST SPECIMENS WITH YTTRIA DISCS

Test (Time)	Dark-Toned Central Ceramic $(U_xZr_y)O_z$ stoichiometry ± 2SD			Light-Toned Outer Ceramic $(U_xZr_y)O_z$ stoichiometry ± 2SD		
	x	y	Z	x	y	z
HF-19 (138 s)	0.64 ± 0.03	0.36 ± 0.03	2.17 ± 0.34	0.88 ± 0.06	0.12 ± 0.06	2.18 ± 0.44
HF-17 (213 s)	0.66 ± 0.03	0.34 ± 0.03	1.86 ± 0.36	0.89 ± 0.03	0.11 ± 0.03	1.84 ± 0.43
HF-18 (339 s)	0.71 ± 0.03	0.29 ± 0.03	2.14 ± 0.24	0.90 ± 0.03	0.10 ± 0.03	2.20 ±0.24
HF-15 (428 s)	0.75 ± 0.05	0.25 ± 0.05	1.96 ± 0.45	0.89 ± 0.06	0.11 ± 0.06	1.95 ± 0.24
HF-30 (610 s)	0.73 ± 0.06	0.27 ± 0.06	1.66 ± 0.17	0.91 ± 0.06	0.09 ± 0.06	1.71 ± 0.04
HF-26 (854 s)	0.66 ± 0.05	0.34 ± 0.05	2.08 ± 0.22	0.89 ± 0.03	0.11 ± 0.03	2.25 ±0.32

Test	Zr(O) alloy (atom %) ± 2SD				U(O) alloy (atom %) ± 2SD			
(Time)	Zr	Sn	U	O	Zr	Sn	U	O
HF-19 (138 s)	66.2 ± 12.9	0.7 ± 0.8	0.8 ± 0.7	32.3 ± 13.45	1.8 ± 1.9	1.3 ± 2.7	61.0 ± 17.2	36.0 ±19.1
HF-17 (213 s)	74.1 ± 10.5	0.9 ± 0.8	0.8 ± 0.5	24.3 ± 11.0	1.9 ± 2.1	0.0 ± 0.1	62.5 ± 18.0	37.4 ± 15.7
HF-18 (339 s)	61.2 ± 2.5	0.8 ± 0.5	0.8 ± 0.5	37.2 ± 2.5	1.5 ± 1.6	1.7 ± 3.3	51.2 ± 6.9	45.8 ± 7.1
HF-15 (428 s)	68.3 ± 7.1	0.5 ± 0.4	0.7 ± 0.5	30.4 ± 7.0	2.4 ± 3.0	0.1 ± 0.6	65.0 ± 12.9	32.8 ± 11.1
HF-30 (610 s)	70.1 ± 3.4	0.9 ± 0.8	1.0 ± 1.1	28.1 ± 2.5	2.3 ± 2.3	0.0 ± 0.0	64.7 ± 7.3	33.0 ± 7.8
HF-26 (854 s)	68.0 ± 3.4	1.0 ± 0.8	1.4 ± 2.1	29.6 ± 4.8	n.a.	n.a.	n.a.	n.a.

n.a. = not analysed
SD = standard deviation

TABLE 4.6

COMPARISON OF MEAN ANALYSES BY LARGE-AREA EDX AND ICP FOR THE 2200°C TEST SPECIMENS WITH YTTRIA DISCS

Test No.	Analysis Method	Zr at.% ± 2SD	Sn at.% ± 2SD	U at.% ± 2SD	O at.% ± 2SD	U/(U+Zr) wt.% ± 2SD
HF-19 (138 s)	EDX	39.49 ± 3.06	0.34 ± 0.59	16.08 ± 1.10	44.17 ± 3.38	0.29 ± 0.00
	ICP	37.44 ± 2.45	0.48 ± 0.05	19.88 ± 1.33	41.84 ± 3.81	0.35 ± 0.01
HF-17 (213 s)	EDX	36.26 ± 10.29	0.08 ± 0.29	17.22 ± 3.15	46.62 ± 14.25	0.32 ± 0.02
	ICP	31.09 ± 2.20	0.41 ± 0.02	20.43 ± 2.08	47.79 ± 4.27	0.40 ± 0.01
HF-18 (339 s)	EDX	25.38 ± 6.52	1.46 ± 0.26	21.09 ± 3.38	52.08 ± 9.63	0.45 ± 0.03
	ICP	23.58 ± 0.71	0.30 ± 0.01	24.08 ± 1.21	51.83 ± 1.92	0.51 ± 0.01
HF-15 (428 s)	EDX	22.23 ± 4.58	0.29 ± 0.64	22.16 ± 2.80	55.32 ± 6.73	0.50 ± 0.02
	ICP	20.51 ± 2.16	0.26 ± 0.04	23.23 ± 2.11	55.84 ± 4.19	0.53 ± 0.01

TABLE 4.7

SUMMARY (MEAN ± 2SD) OF AREA ANALYSES, 2200°C MELTS WITH YTTRIA

Test (Time)	Inner (Dark) Ceramic	Outer (Light) Ceramic	*Total Ceramic*	Zr(O) Alloy	U-Rich Alloy
HF-19 (138 s)	13.6 ± 5.9	25.4 ± 12.5	*39.0 ± 8.0*	55.2 ± 9.6	5.8 ± 1.7
HF-17 (213 s)	20.4 ± 10.5	27.2 ± 5.0	*47.6 ± 8.8*	48.4 ± 7.8	4.0 ± 2.0
HF-18 (339 s)	24.0 ± 6.3	35.4 ± 6.7	*59.4 ± 4.1*	38.0 ± 4.7	2.6 ± 1.1
HF-15 (428 s)	23.5 ± 10.1	40.5 ± 9.3	*64.0 ± 4.3*	33.3 ± 3.8	2.8 ± 1.0
*HF-30 (610 s)	21.7 ± 9.5	47.0 ± 14.0	*68.7 ± 5.8*	29.0 ± 5.3	2.3 ± 1.2
*HF-26 (854 s)	28.0 ± 8.7	40.0 ± 5.3	*68.0 ± 9.2*	30.3 ± 9.5	1.7 ± 1.2

* Failed tests, melt times estimated from the time/temperature traces.

TABLE 5.1

MATERIAL DIMENSIONS AND WEIGHTS, 2200°C TESTS WITHOUT BOTTOM ISOLATION

Crucible, Test No.	[1]I.D. (mm)	[2]O.D. (mm)	Height mm	[3]Depth (mm)	Post-Test O.D. (mm)	Crucible Wt. (g)	Zircaloy Wt. (g)	Mass Ratio
HF-28	15.82	26.44	31.41	14.06	26.45	144.514	8.0400	17.98
HF-24	15.72	26.48	31.48	16.18	26.47	140.530	7.791	18.04
HF-27	15.73	26.49	31.40	16.37	26.43	140.323	7.786	18.03
HF-29	15.88	26.49	31.43	15.46	26.41	140.834	7.807	18.04
HF-22	16.06	26.54	31.43	16.83	26.47	139.782	7.745	18.05
HF-21	15.75	26.49	31.43	16.07	26.43	141.424	7.855	18.00
HF-20	15.71	26.47	31.42	16.11	26.45	141.777	7.891	17.97

[1]Inner diameter; [2]outer diameter; [3]cavity depth.

TABLE 5.2

DISSOLUTION TEST PARAMETERS

Test No.	Target time, Temp.(°C)	[1] Discontinuity temp. (°C)	Total time molten (s)	Main part of isotherm
HF-28	100 s, 2200	1952	150	2198 ± 8°C for 32 s
HF-24	100 s, 2200	1926	150	uncertain (see text)
HF-27	200 s, 2200	1915	216	2199 ± 12°C for 66 s
HF-29	300 s, 2200	1946	324	2201 ± 6°C for 153 s
HF-22	400 s, 2200	1941	433	2202 ± 7°C for 273 s
HF-21	600 s, 2200	1995	612	2199 ± 6°C for 413 s
HF-20	600 s, 2200	1939	613	2201 ± 6°C for 330 s

[1]Observed in the Zircaloy time/temperature curve from melting and/or emissivity change.

TABLE 5.3

MEAN ICP RESULTS (± 2SD) FOR 2200°C MELTS WITHOUT BOTTOM ISOLATION

Test Number	Melt time (s)	U Wt.%	Zr wt.%	Fe wt.%	Cr wt.%	Sn wt.%	*O wt.%	U/(U+Zr) wt.% ratio
HF-28	150	53.40 ± 0.00	36.25 ± 0.42	0.07 ± 0.01	0.04 ± 0.00	0.48 ± 0.04	9.75 ± 0.42	59.60 ± 0.28
HF-24	150	60.55 ± 0.71	28.60 ± 0.57	0.05 ± 0.00	0.03 ± 0.00	0.36 ± 0.01	10.40 ± 1.41	67.95 ± 0.14
HF-27	216	62.40 ± 0.28	25.85 ± 0.14	0.04 ± 0.00	0.02 ± 0.00	0.31 ± 0.00	11.35 ± 0.42	70.70 ± 0.00
HF-29	324	65.90 ± 0.00	22.65 ± 0.14	0.04 ± 0.00	0.02 ± 0.00	0.27 ± 0.01	11.15 ± 0.14	74.45 ± 0.14
HF-22	433	65.45 ± 1.50	22.80 ± 0.28	0.04 ± 0.00	0.02 ± 0.00	0.29 ± 0.01	11.40 ± 1.70	74.15 ± 0.14
HF-21	612	64.55 ± 0.71	23.85 ± 0.14	0.04 ± 0.00	0.02 ± 0.00	0.29 ± 0.00	11.30 ± 0.57	73.00 ± 0.28
HF-20	613	65.35 ± 0.14	23.00 ± 1.13	0.04 ± 0.00	0.02 ± 0.00	0.28 ± 0.03	11.35 ± 0.99	73.95 ± 0.99

*O values by difference

TABLE 5.4

IMAGE ANALYSIS RESULTS FOR 2200°C MELTS WITHOUT BOTTOM ISOLATION

Test No	Wall Dissolution V_W , mm³	Bottom dissolution V_B, mm³	Volume ratio $(V_W + V_B)/V_{Zry}$	V_H, mm³ (*)	Cruc. wall thickness µm	Height ratio H_{diss}/h_{Zry}	O_{dif}/O_{melt} %
HF-28	1523	371	1.37	2764	3396	2.00	17
HF-24	977	280	0.94	2426	3971	1.85	32
HF-27	1704	276	1.47	2592	3143	1.98	28
HF-29	2399	439	2.11	2805	2537	2.19	18
HF-22	2163	291	1.84	2770	2584	2.11	23
HF-21	2009	336	1.73	2617	2853	2.00	23
HF-20	2151	238	1.76	2920	2925	2.15	23

(*) V_H - melt volume without account of dissolved crucible space

TABLE 5.5

MEAN CERAMIC AND ZR-ALLOY PHASE COMPOSITIONS FROM 2200°C TESTS WITOUT YTTRIA DISCS: LINK-ISIS EDX ANALYSES

Test	$(U_xZr_y)O_z$ stoichiometry ± 2SD			Zr(O) alloy (atom %) ± 2SD			
(Time)	X	y	z	Zr	Sn	U	O
HF-28 (150 s)	0.93 ± 0.03	0.07 ± 0.03	2.10 ±0.42	67.9 ± 3.1	0.4 ± 0.2	0.6 ± 0.2	31.1 ± 3.2
HF-27 (216 s)	0.92 ± 0.04	0.08 ± 0.04	1.81 ± 0.19	69.2 ± 4.3	0.6 ± 0.4	1.0 ± 1.7	29.1 ± 4.8
HF-29 (324 s)	0.91 ± 0.03	0.09 ± 0.03	1.61 ± 0.15	71.0 ± 7.8	0.7 0.4	1.2 ± 2.4	27.1 ± 7.7
HF-22 (433 s)	0.89 ± 0.03	0.11 ± 0.03	1.92 ± 0.27	69.0 ± 4.5	0.9 0.5	0.8 ± 0.4	29.2 ± 4.7
HF-21 (612 s)	0.86 ± 0.05	0.14 ± 0.05	2.14 ± 0.13	68.4 ± 5.6	1.0 1.0	0.6 ± 0.3	30.0 ± 5.9

SD = standard deviation

TABLE 5.6

PERCENT PHASE-AREA ANALYSES (MEAN ± 2SD) IN THE 2200°C MELTS WITHOUT YTTRIA

Specimen (time)	Ceramic Phase	U(O) Alloy	Zr(O) Alloy
HF-28 (150 s)	48.6 ± 7.0	3.8 ± 0.9	47.6 ± 7.2
HF-27 (216 s)	51.0 ± 11.6	2.6 ± 1.1	46.4 ± 10.5
HF-29 (324 s)	57.0 ± 11.6	1.2 ± 0.9	41.8 ± 11.8
HF-22 (433 s)	61.1 ± 7.6	1.5 ± 0.5	37.4 ± 7.8
HF-21 (612 s)	63.8 ± 11.6	1.0 ± 0.0	35.2 ± 11.6

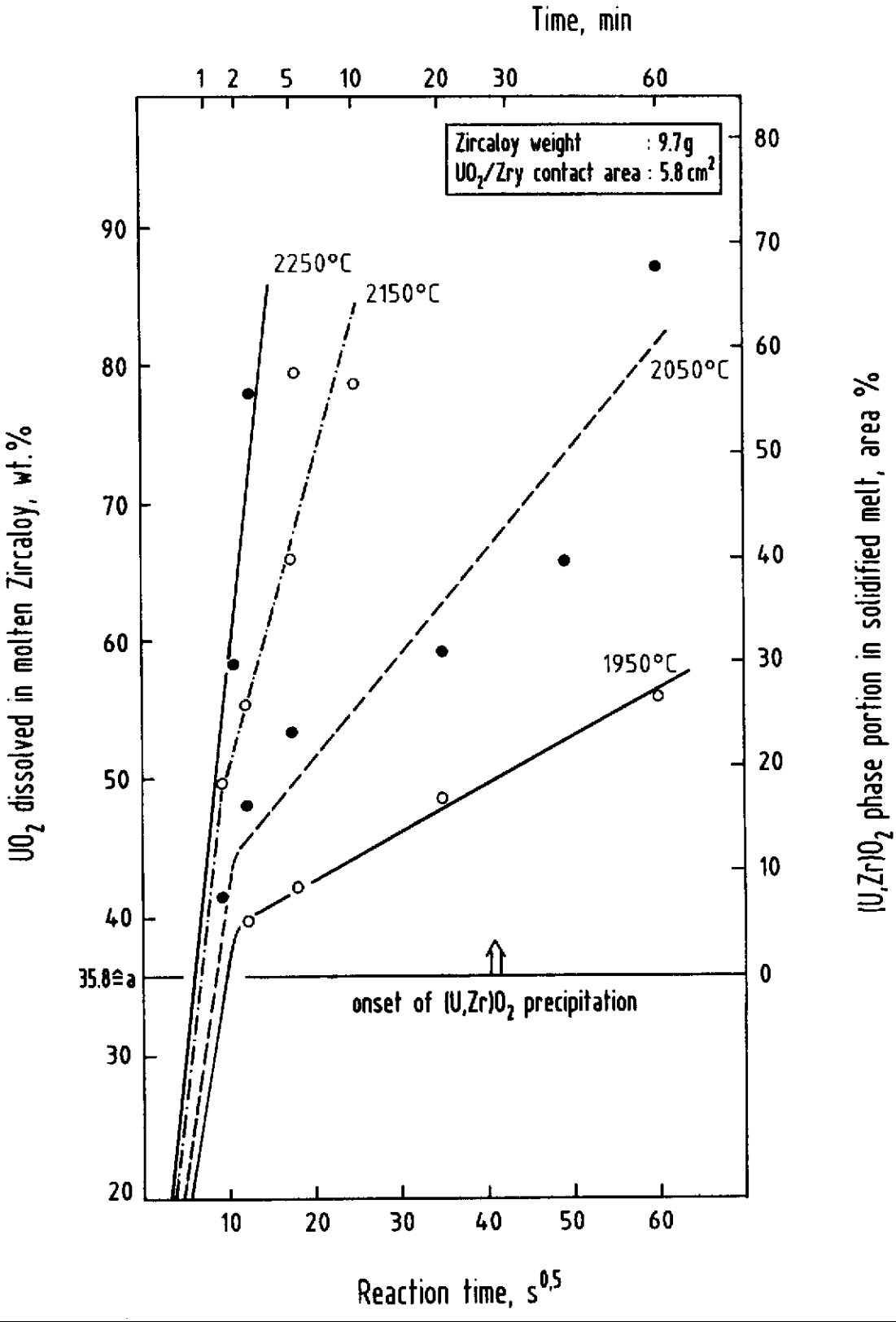

Fig. 1.1: $(U,Zr)O_2$ ceramic phase portion in solidified (Zr,U,O) melts and UO2 content in molten Zircaloy as a function of square root of time for different reaction temperatures

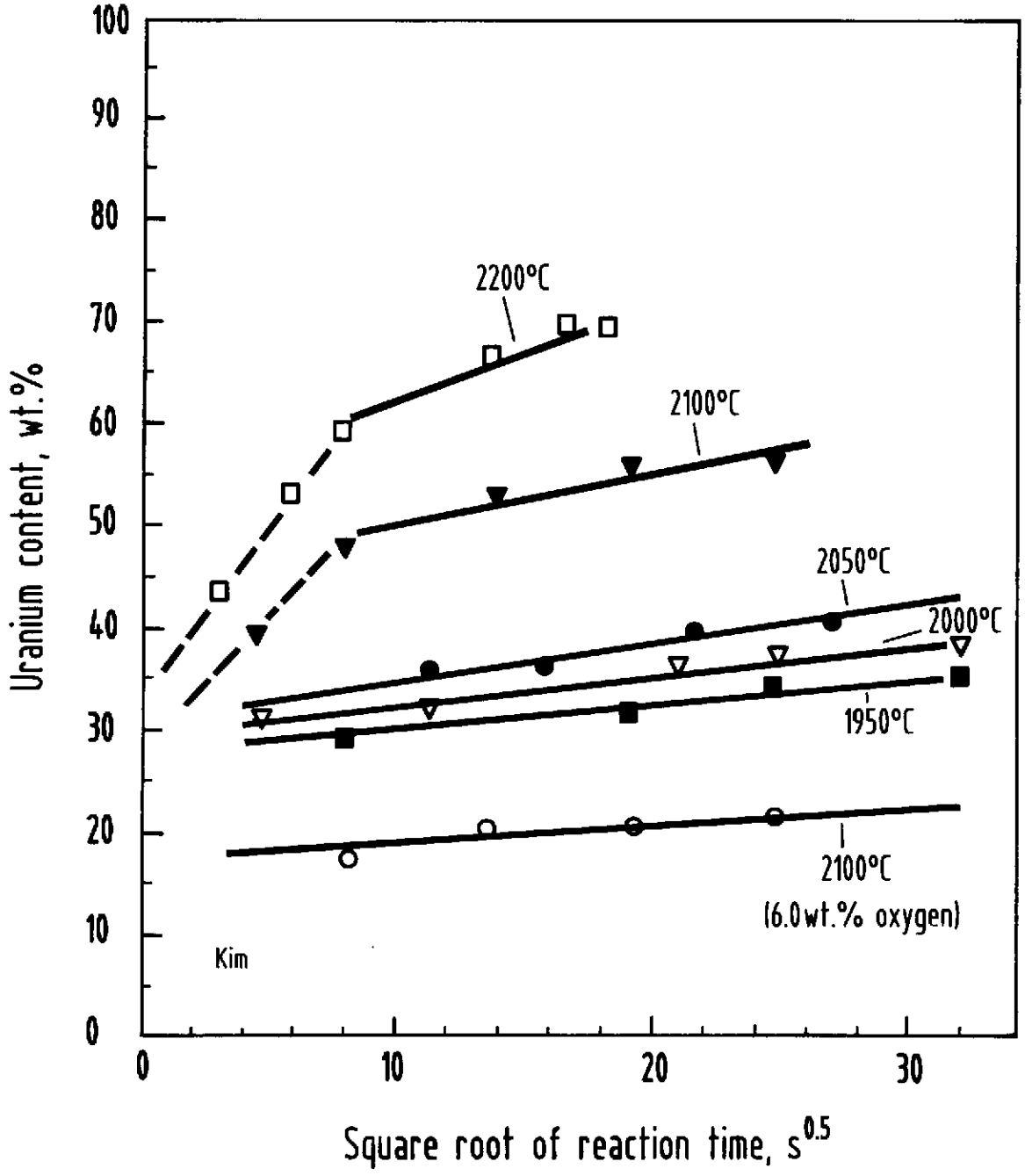

Fig.1.2: Uranium content in region II [liquid+$(U,Zr)O_{2-x}$ precipitates] versus square root of reaction time for various reaction temperatures

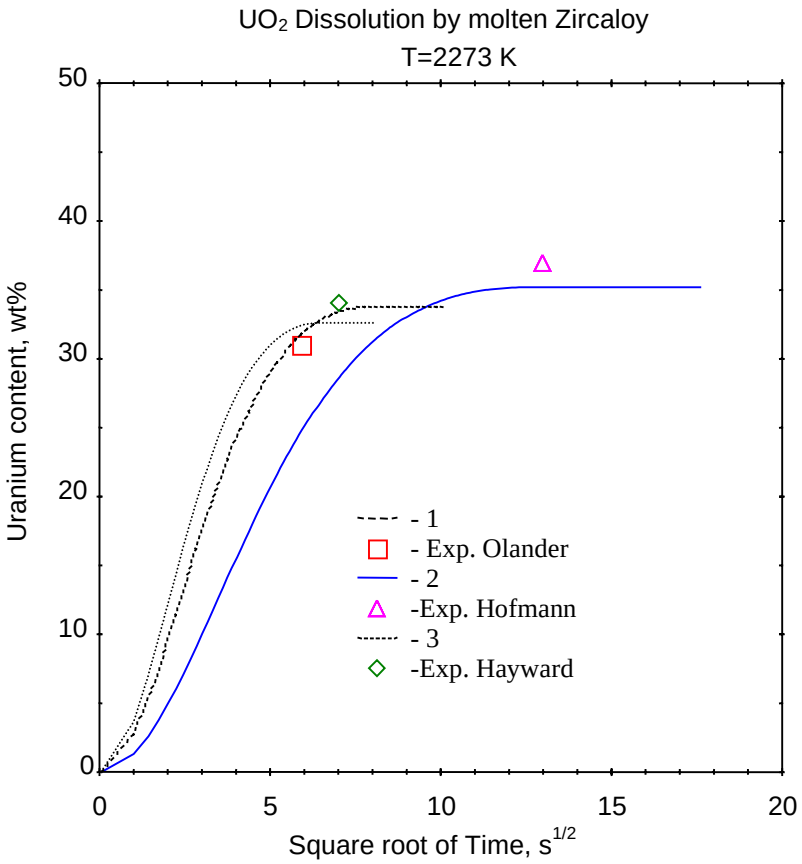

Fig. 1.3: Uranium weight content in the melt in the first, saturation stage of the dissolution process. Calculated by the model [11,12] curves 1,2,3 correspond to the experimental data [2,4,6].

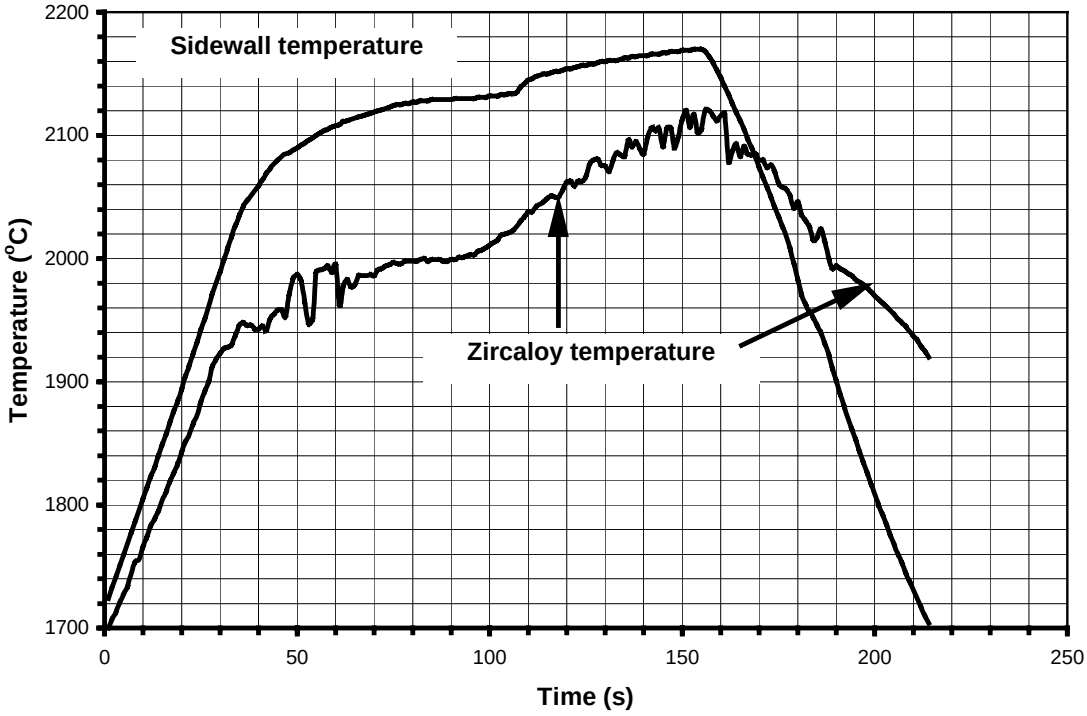

Fig. 3.1: Pyrometer Traces for Test HF-13 (Target 100 s at 2100°C).

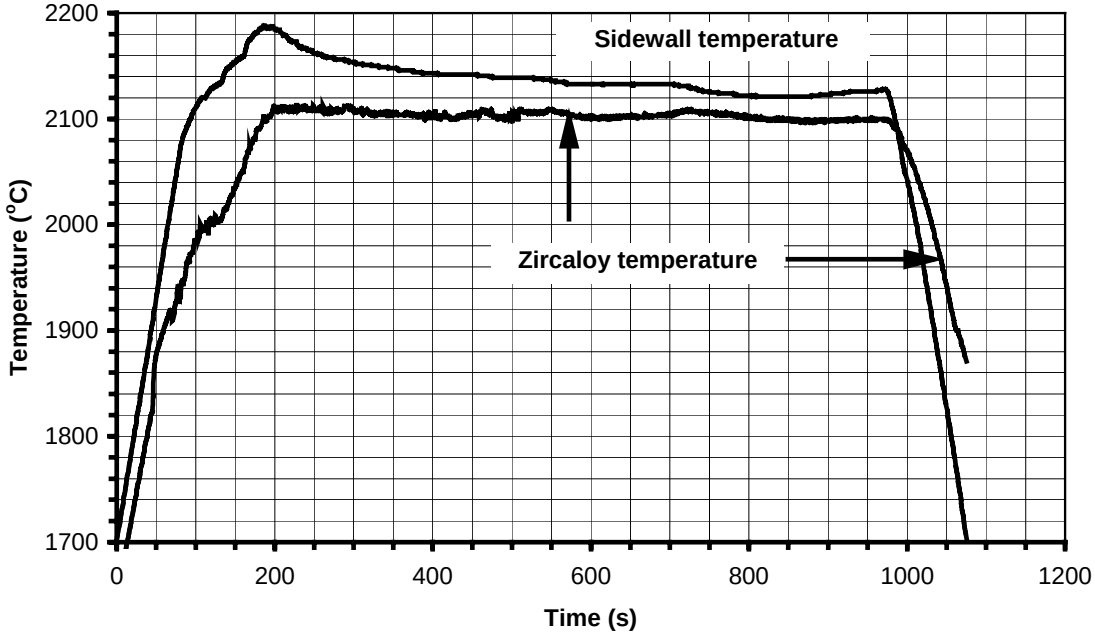

Fig. 3.2: Pyrometer Traces for Test HF-1 (Target 900 s at 2100°C).

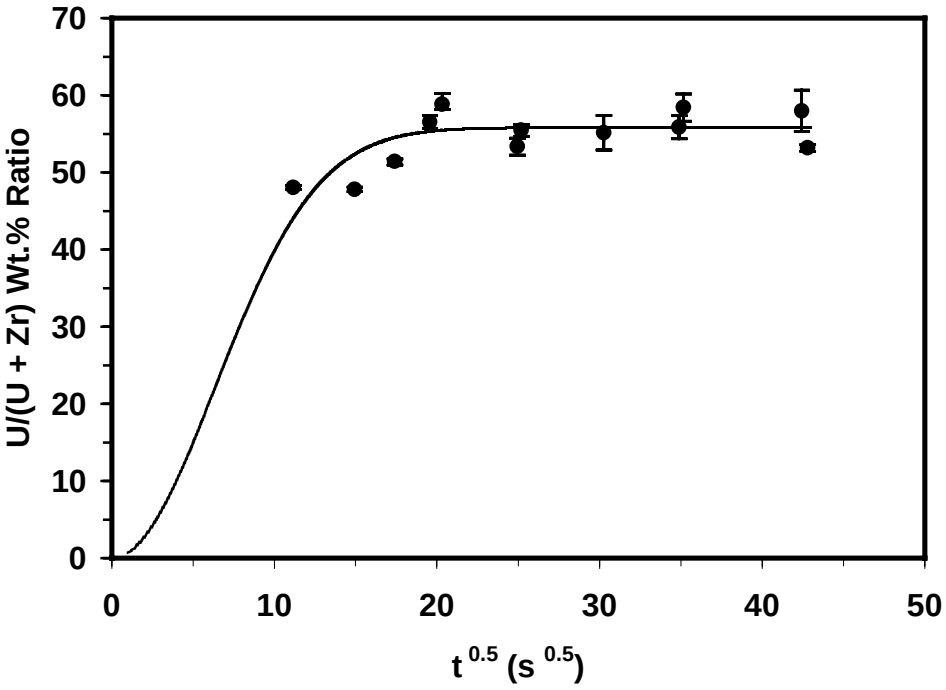

Fig. 3.3: ICP Results for 2100°C Test Series (No Yttria Discs), with Visual Best Fit Curve. Error Bars = ±2SD.

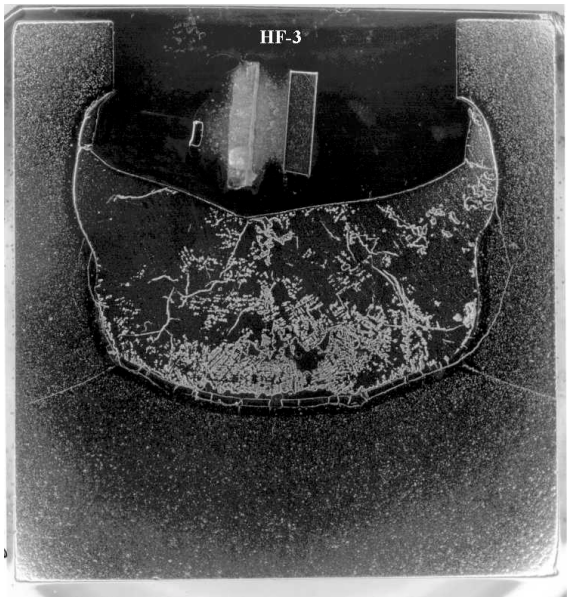

Fig. 3.4: Cross section of UO_2 crucible, as-polished

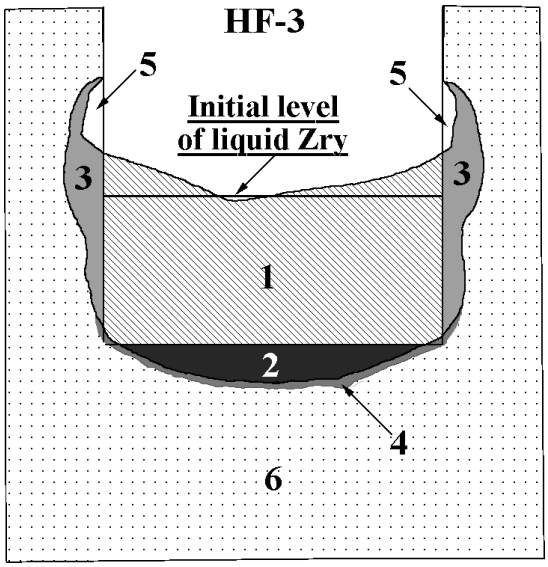

Fig. 3.5: Typical interaction zones in UO_2 crucible

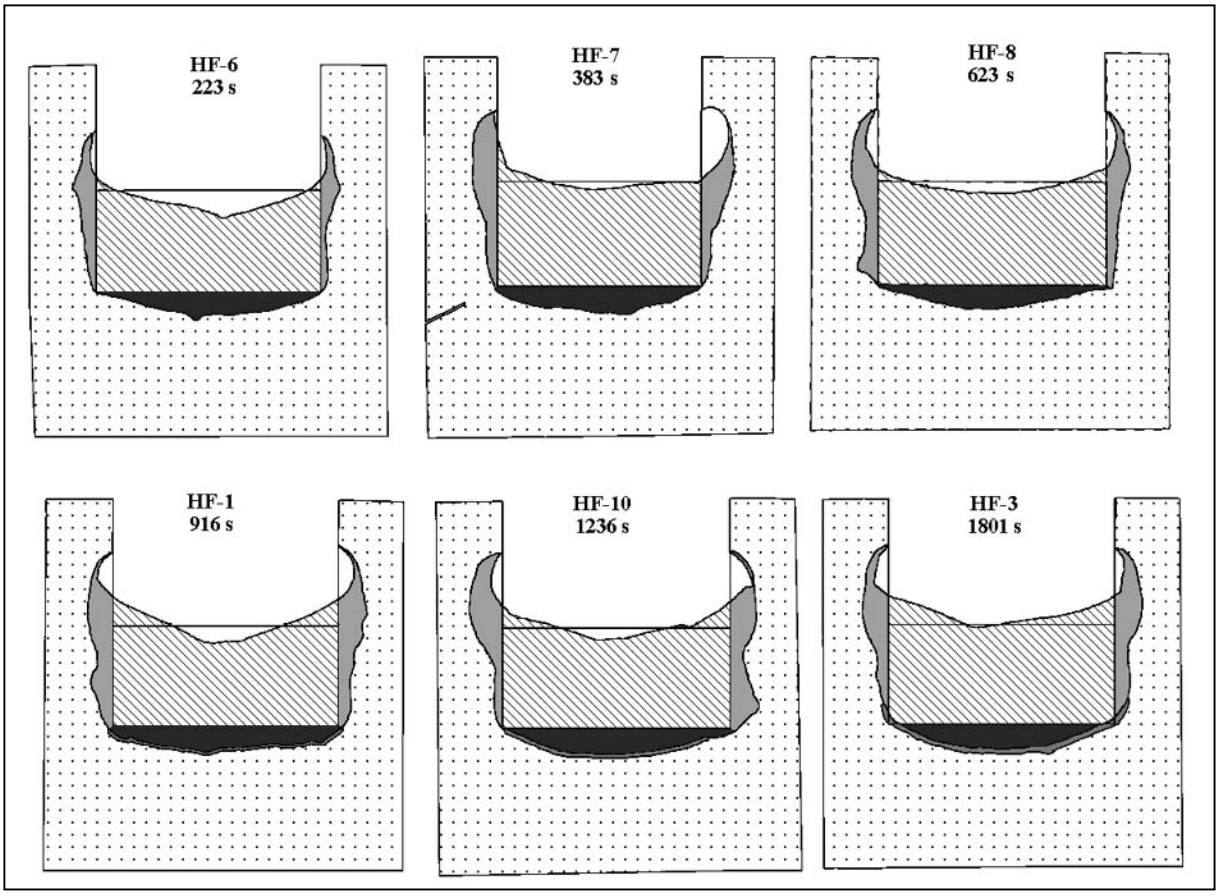

Fig. 3.6: Image analysis of interactions between liquid Zry and solid UO_2 at 2100°C after different reaction times

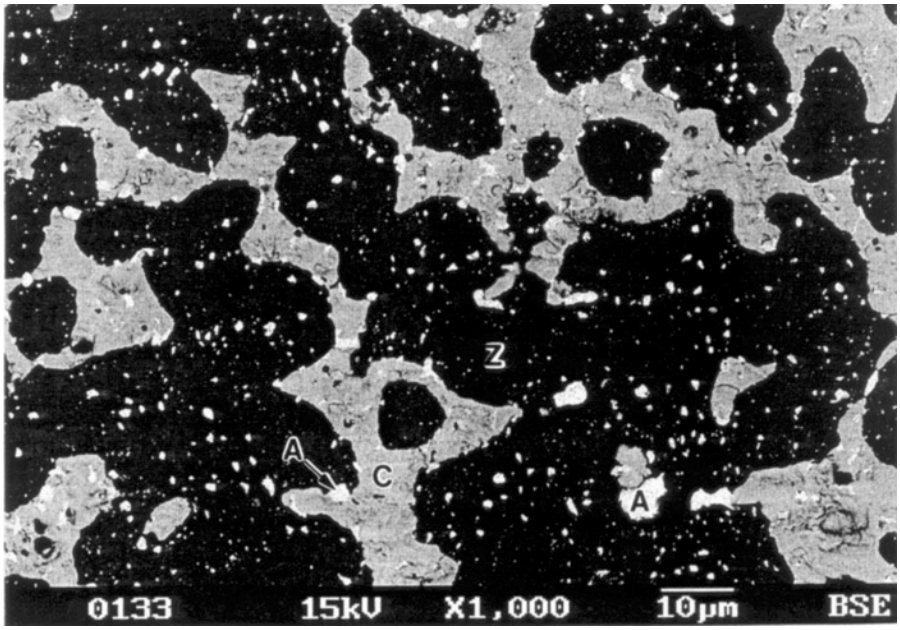

Fig. 3.7: BSE Micrograph of the Top-Left Region of the HF-6 Specimen (2100^{o}C, 223 s) Showing the Three Phase Types: a (U,Zr)O_{2-x} Ceramic Phase (C); a Zr(O) Alloy Phase (Z); and a U-Rich Alloy Phase (A).

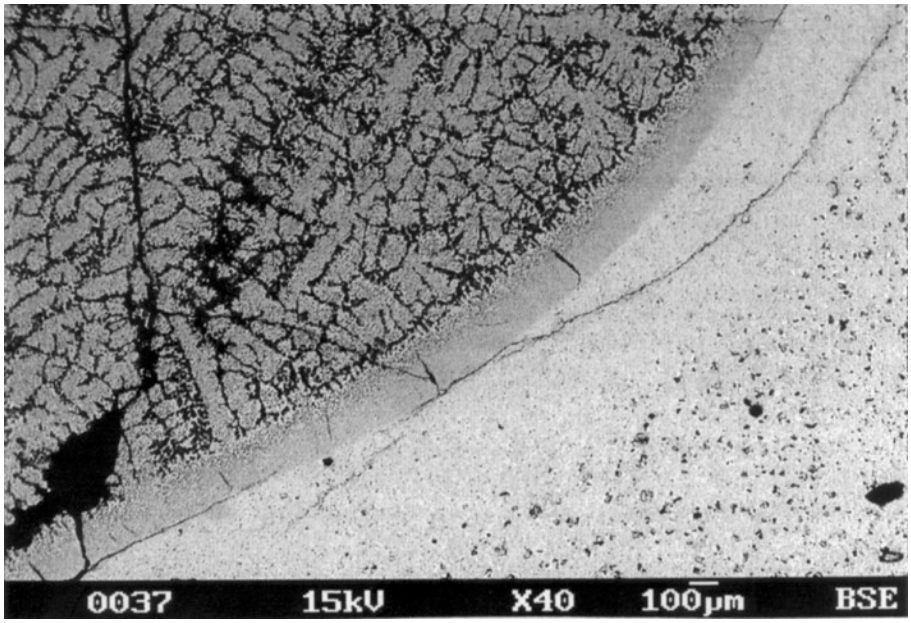

Fig. 3.8: BSE Micrograph of the Crucible/Melt Interface at the Right Corner of the HF-10 Specimen (2100^{o}C, 1236 s), Showing Formation of a ≤350-µm-Wide Transition Zone Along the Base and Lower Sidewalls.

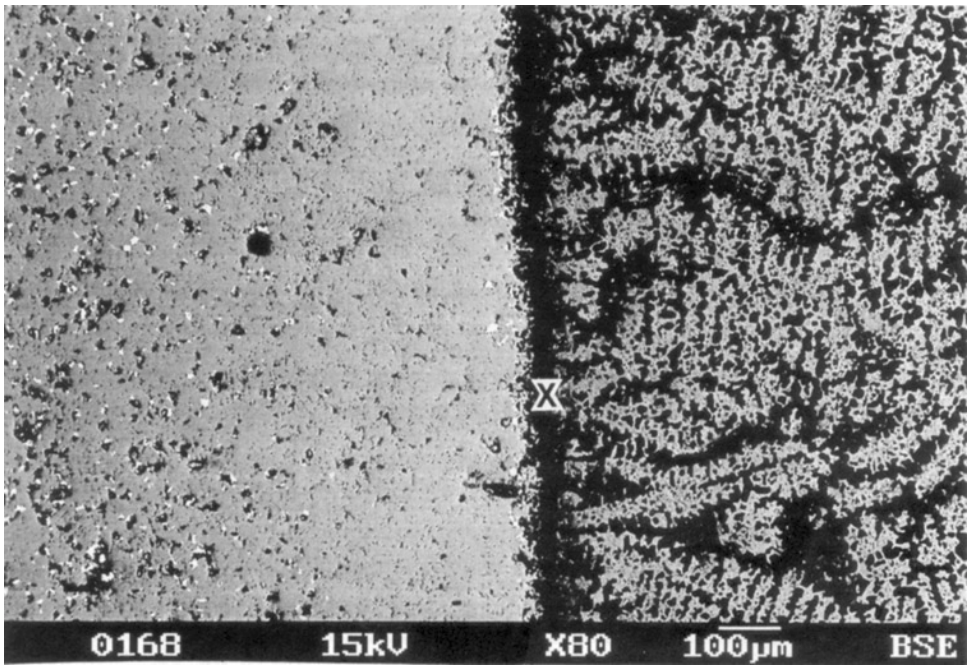

Fig. 3.9: BSE Micrograph of the Crucible/Melt Interface at the Left Sidewall of the HF-7 Specimen (2100^{o}C, 383 s), Showing U-Metal Precipitates in the Residual Crucible, a ~300-µm-wide U-Metal-Free Zone and U-Metal Precipitates at Regions of Direct Contact with the Melt. X = Cooling Crack.

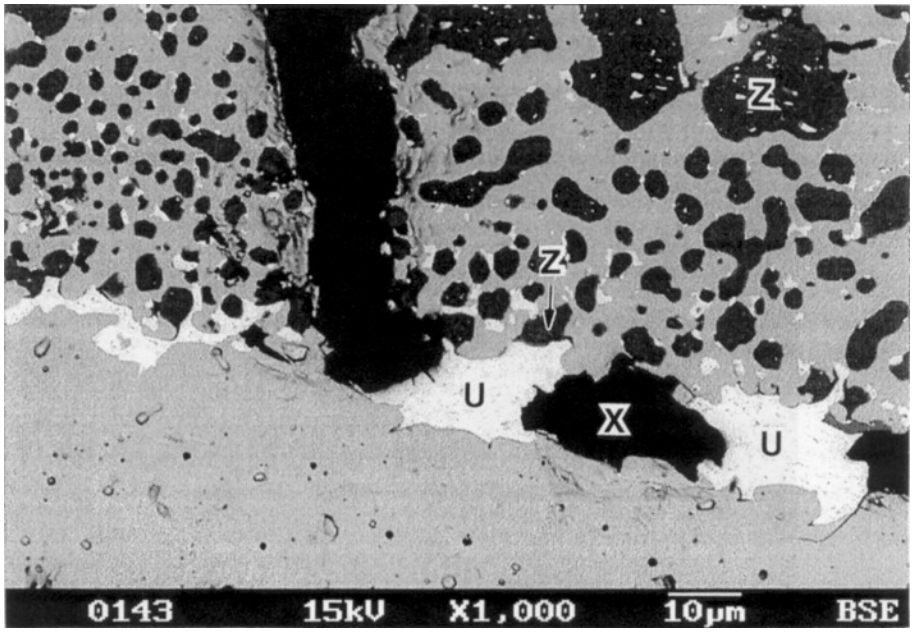

Fig. 3.10: U-Metal Precipitates (U) in Sharp Contact with Zr(O) Alloy Phase (Z) at the Melt/Crucible Interface from the Bottom of the HF-6 Specimen (2100^{o}C, 223 s). X = Cooling Crack.

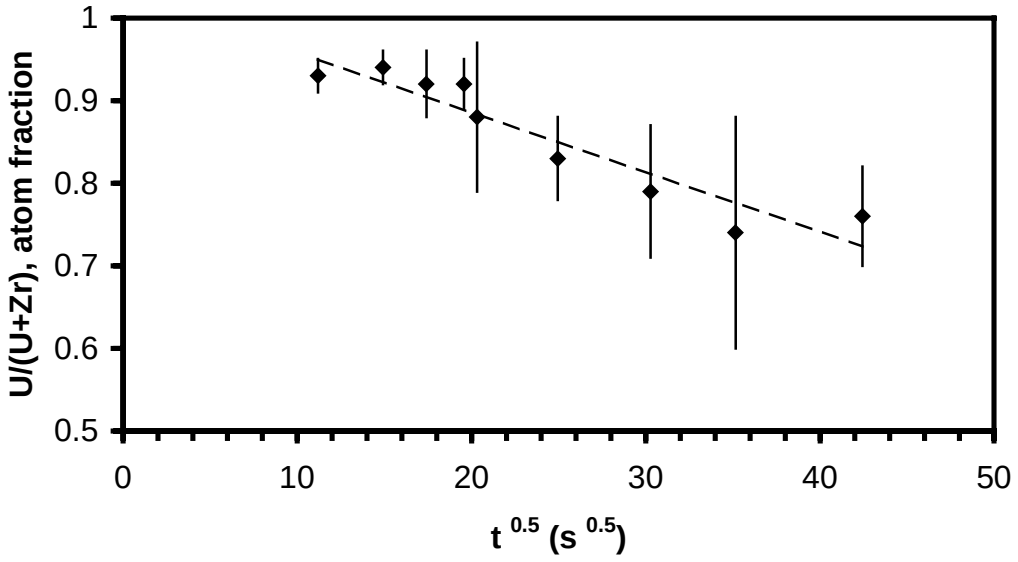

Fig 3.11: EDX Analyses (Mean ± 2SD) for U/(U + Zr) Atomic Fractions in the $(U,Zr)O_{2-x}$ Ceramic Phase from 2100°C Melts (Without Yttria Discs), Plotted against $t^{0.5}$

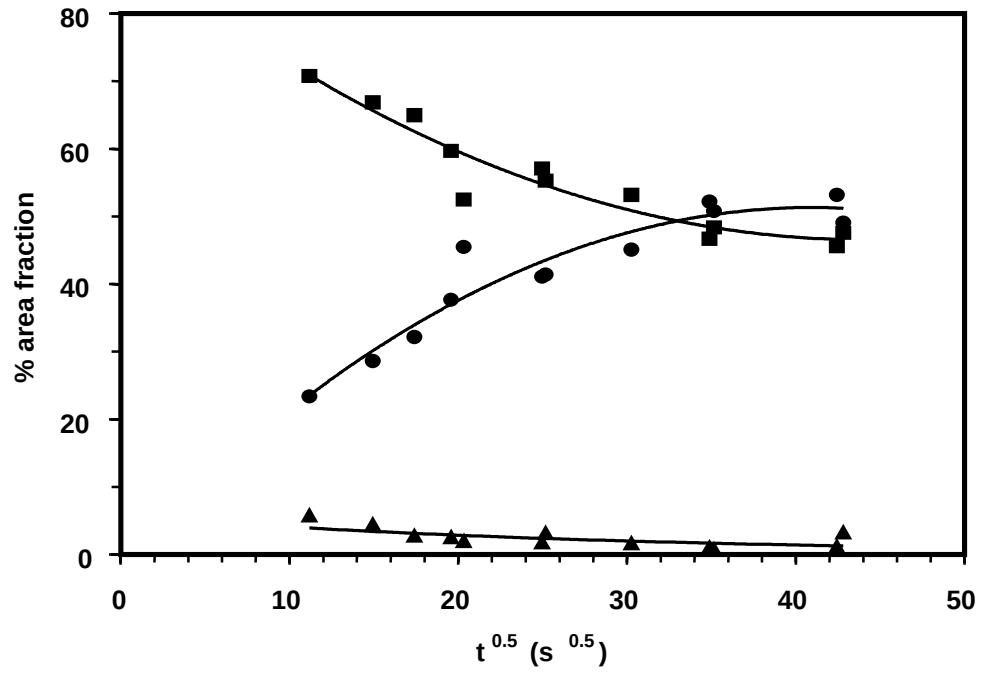

Fig 3.11: Mean Phase-Area Fractions Versus $t^{0.5}$ for 2100°C Series (No Yttria Discs). Triangles = U(O) Alloy; Circles = $(U,Zr)O_{2-x}$ Ceramic; Squares = Zr(O) Alloy

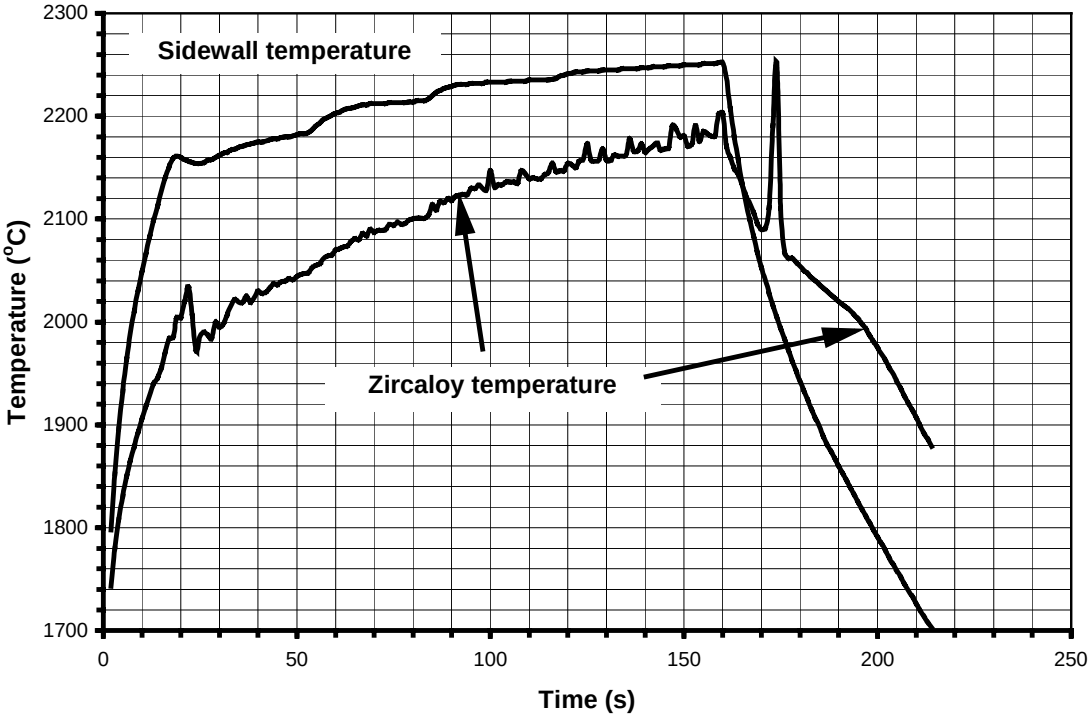

Fig. 4.1: Pyrometer Traces for Test HF-19 (Target 100 s at 2200°C).

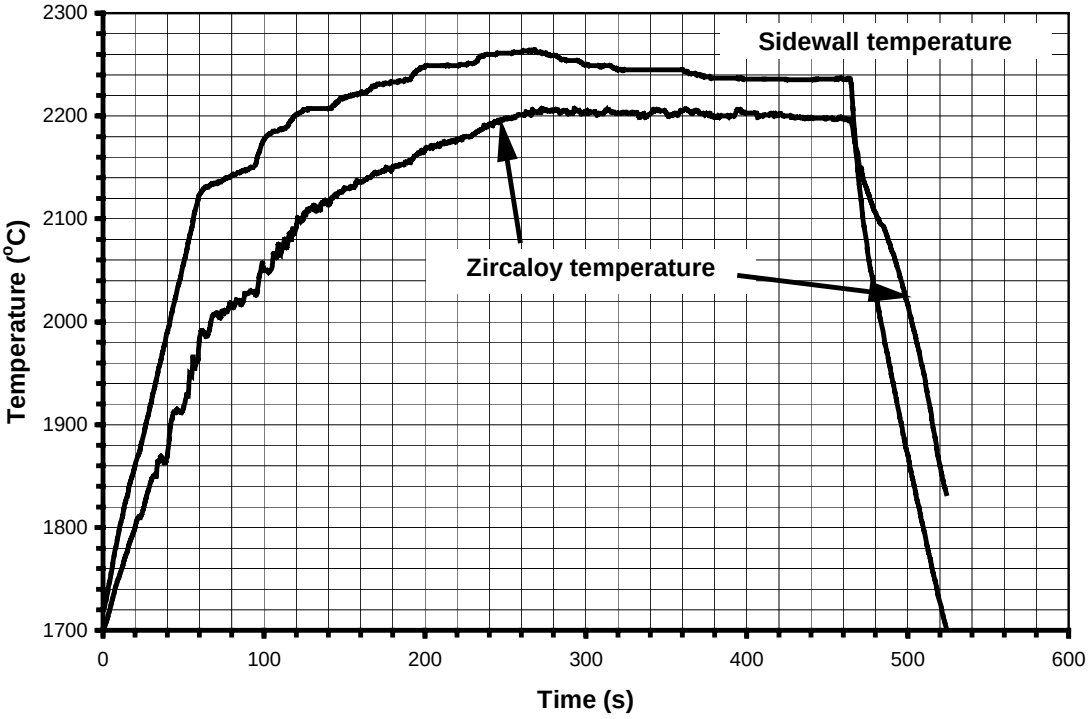

Fig. 4.2: Pyrometer Traces for Test HF-15 (Target 400 s at 2200°C).

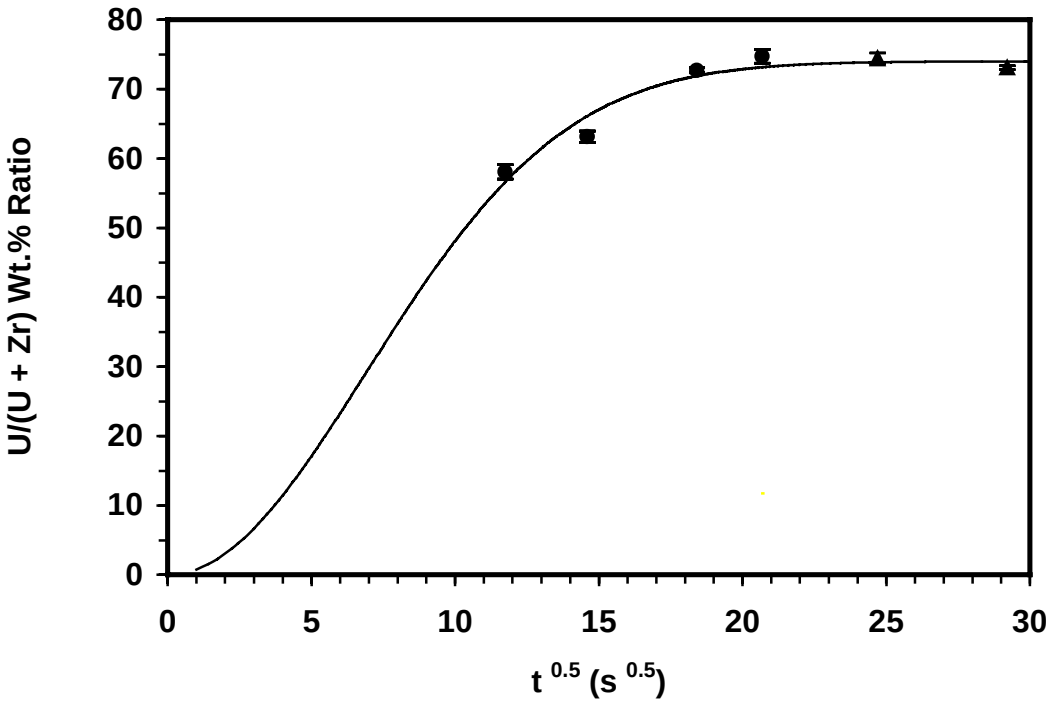

Fig. 4.3: ICP Results for 2200^{o}C Test Series with Bottom Isolation. Error Bars are ±2SD. Visual Best Fit Curve also Shown.

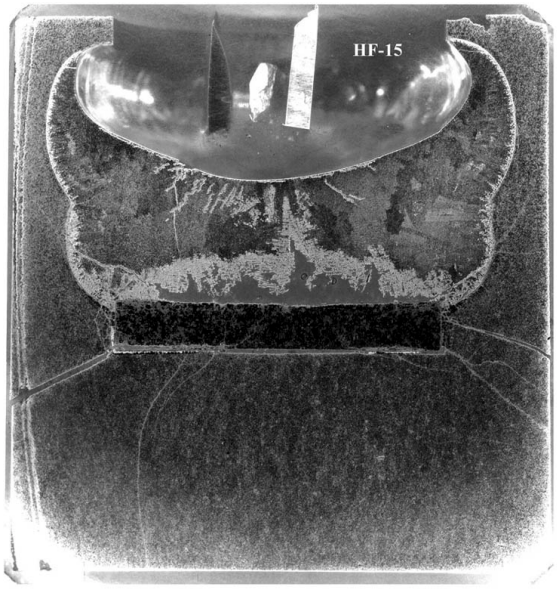

Fig. 4.4: Cross section of UO_2 crucible, zones as-polished

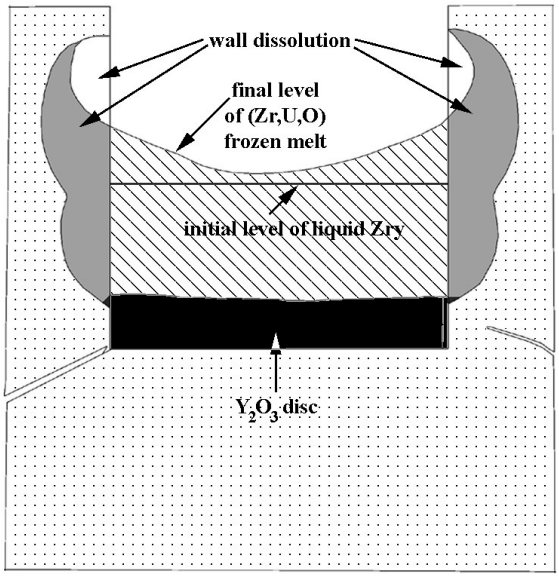

Fig. 4.5:Typical interaction in UO_2 crucible

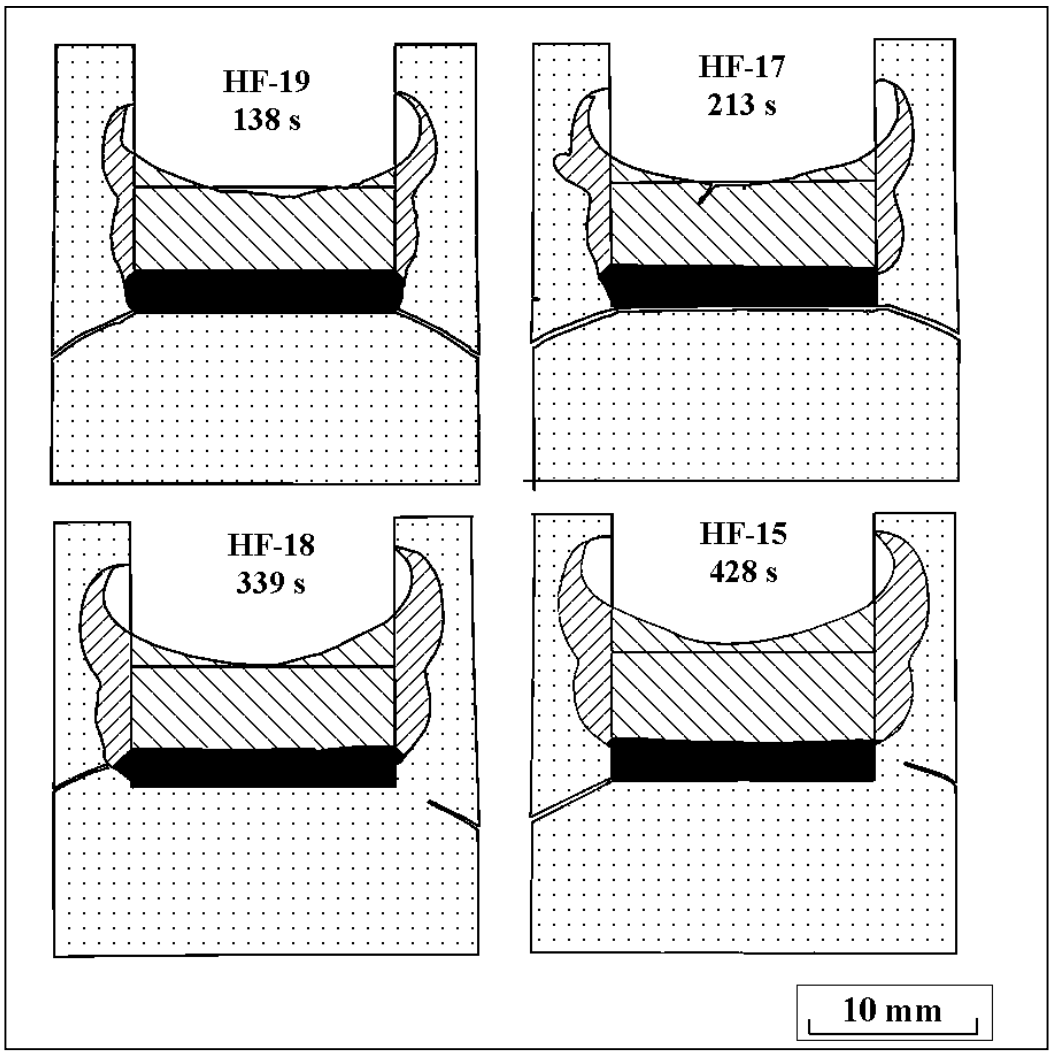

Fig. 4.6: Image analysis of interactions between liquid Zry and solid UO_2 at 2200°C after different reaction times

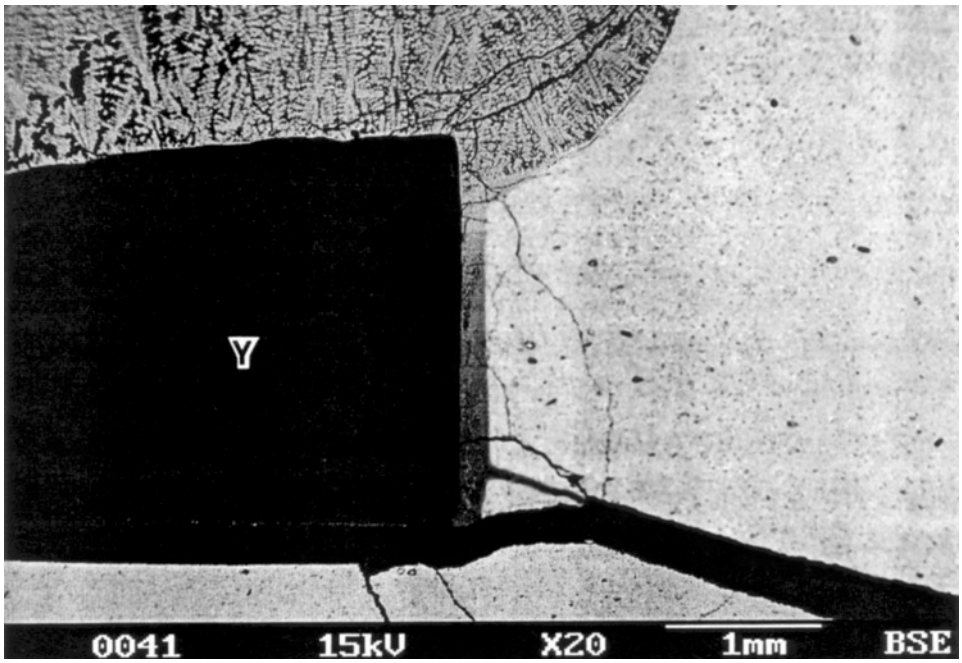

Fig. 4.7: BSE Micrograph of the Bottom Right Corner of the HF-17 Specimen (2200^{o}C, 213 s), Showing Dendritic Microstructure of the Melt. Y = Yttria Disc.

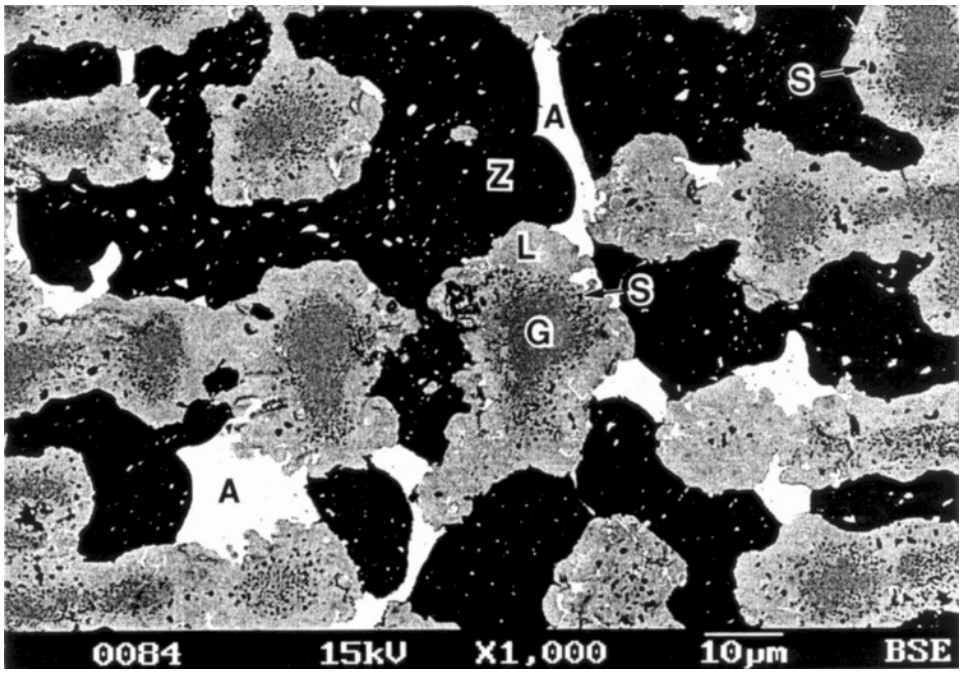

Fig. 4.8: BSE Micrograph of the Central Melt Region in the HF-19 Specimen (2200^{o}C, 138 s). G = Zr-rich Inner Ceramic Zone; L = Outer Ceramic Zone; Z = Zr(O) Alloy; A = U(O) Alloy; S = Inclusions of Zr(O) in the Ceramic Phase.

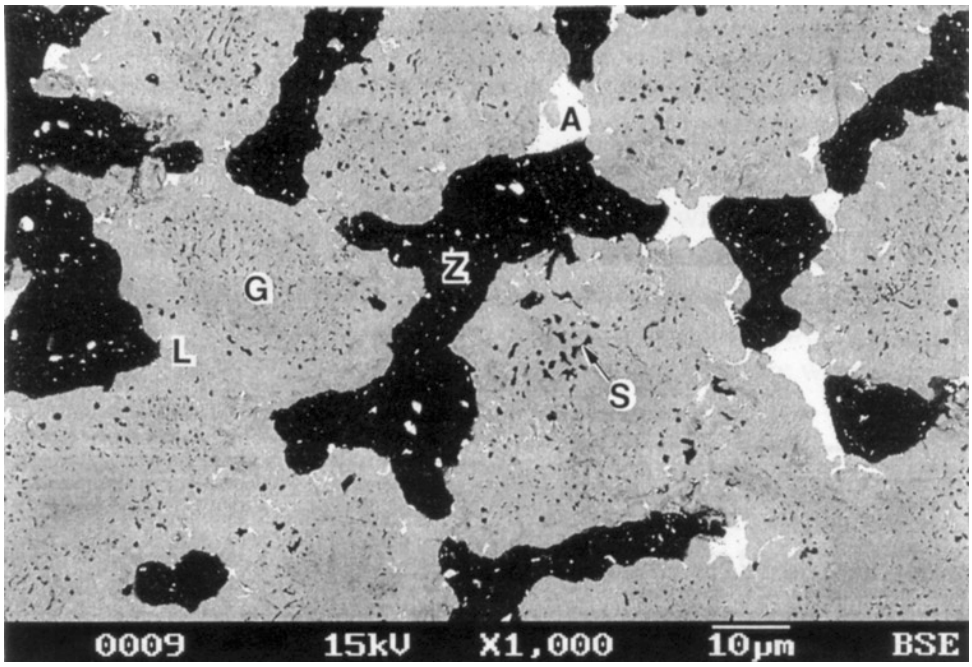

Fig. 4.9: BSE Micrograph of the Central Melt Region in the HF-15 Specimen (2200^{o}C, 428 s). G = Zr-rich Inner Ceramic Zone; L = Outer Ceramic Zone; Z = Zr(O) Alloy; A = U(O) Alloy; S = Inclusions of Zr(O) in the Ceramic Phase.

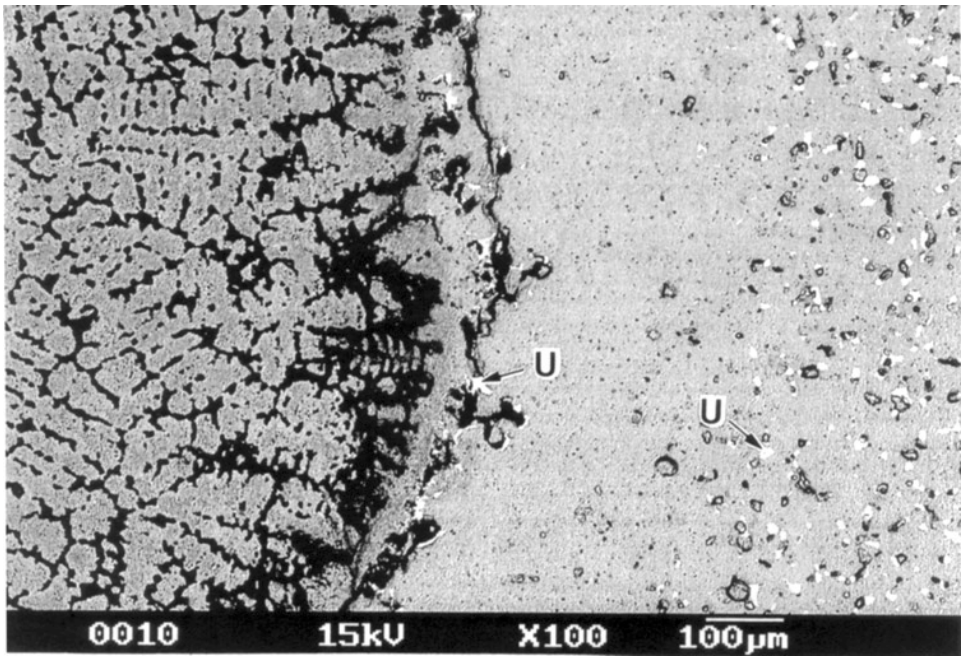

Fig. 4.10: BSE Micrograph of the Right Melt/Crucible Interface in the HF-26 Specimen (2200^{o}C, 853 s), Showing U-Metal Precipitates (U) at the Interface and in the Residual Crucible, Separated by a ~300-µm U-Free Zone.

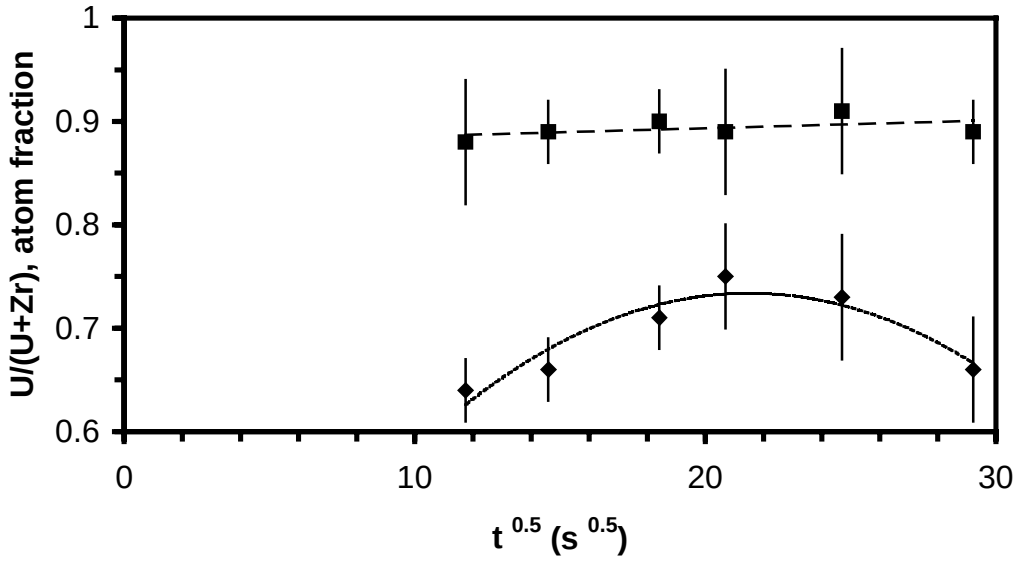

Fig. 4.11: EDX Analyses (Mean ± 2SD) for U/(U + Zr) Atomic Ratios in the Zoned Ceramic Phase from 2200°C Melts with Bottom Isolation, Plotted Against $t^{0.5}$. Squares = Outer (U-Rich) Zone; Diamonds = Inner (Zr-Rich) Zone

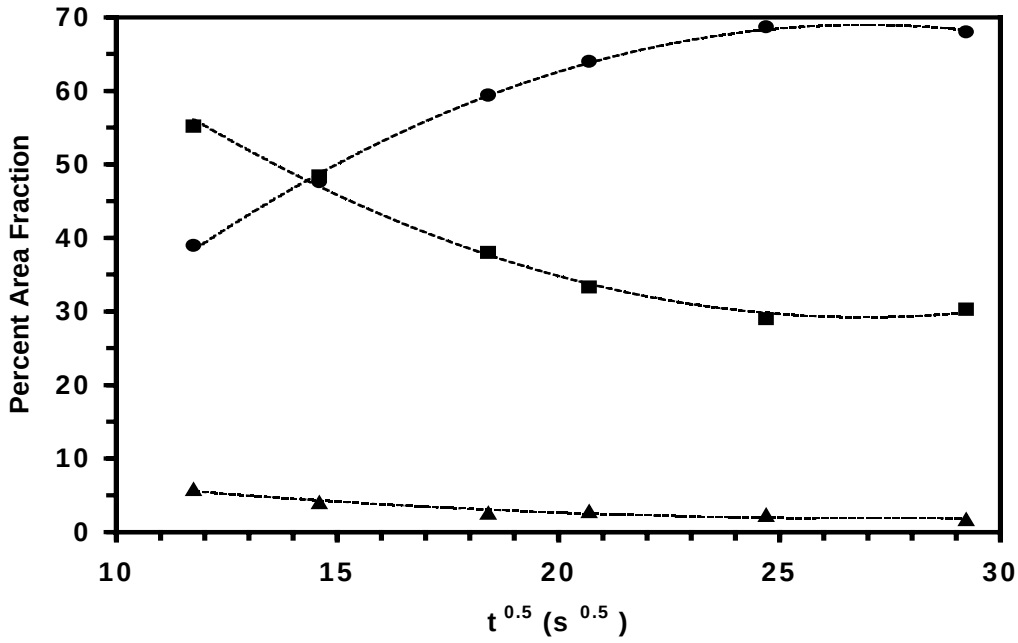

Fig. 4.12: Mean Phase-Area Fractions for 2200°C Series with Bottom Isolation, Plotted Against $t^{0.5}$. Triangles = U(O) Alloy; Circles = $(U,Zr)O_{2-x}$ Ceramic Squares = Zr(O) Alloy

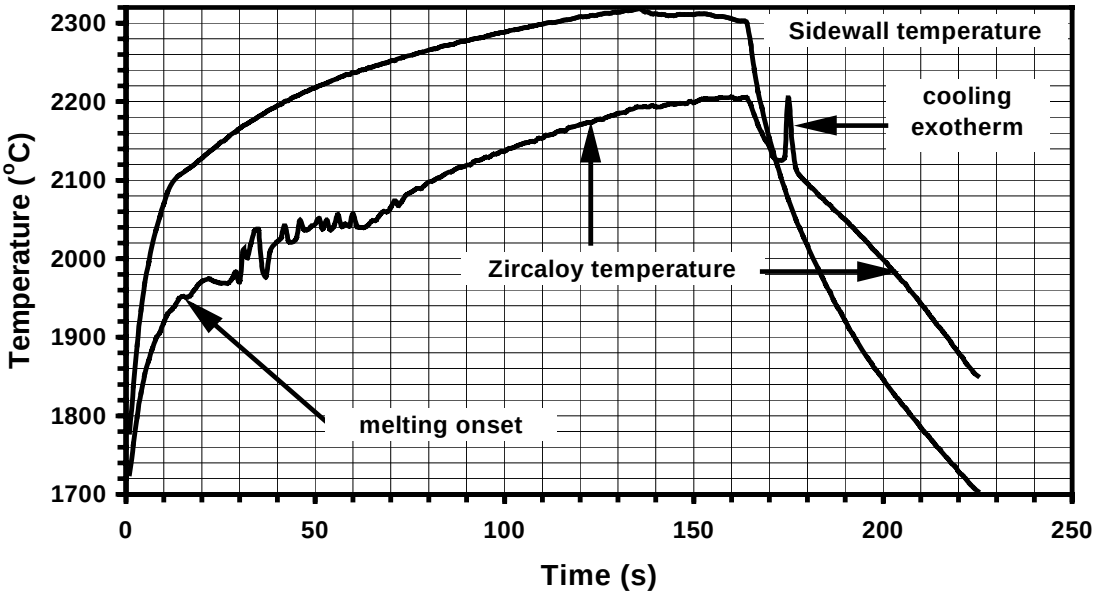

Fig. 5.1: Pyrometer Traces for Test HF-28 (150 s at 2200°C).

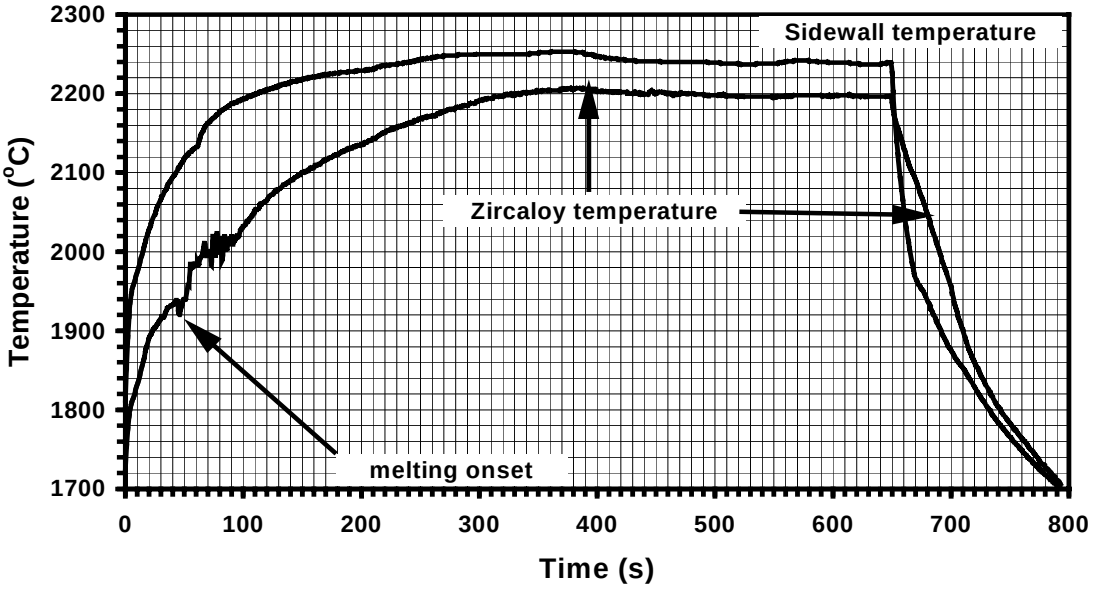

Fig. 5.2: Pyrometer Traces for Test HF-20 (613 s at 2200°C).

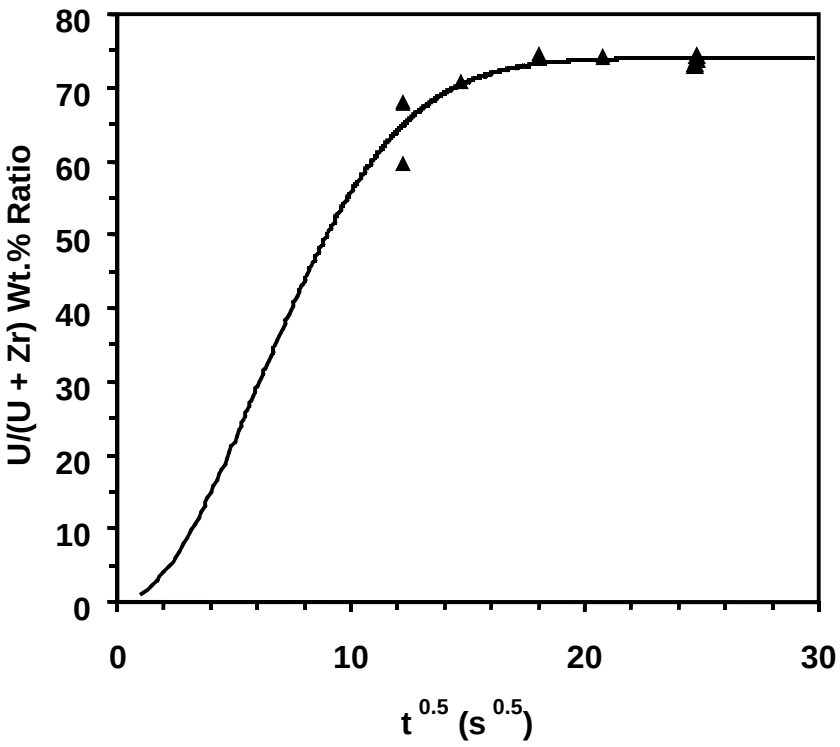

Fig. 5.3: ICP Results for 2200^{o}C Test Series (No Yttria Discs), also Showing Visual Best Fit Curve

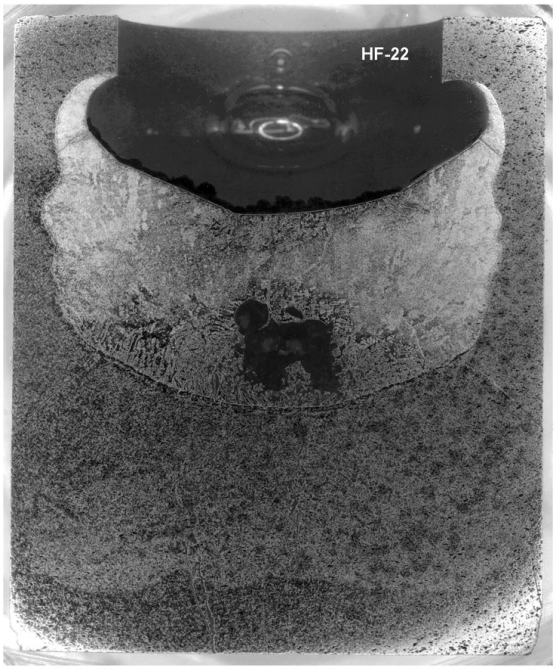

Fig. 5.4: Cross section of UO_2 crucible, zones as-polished

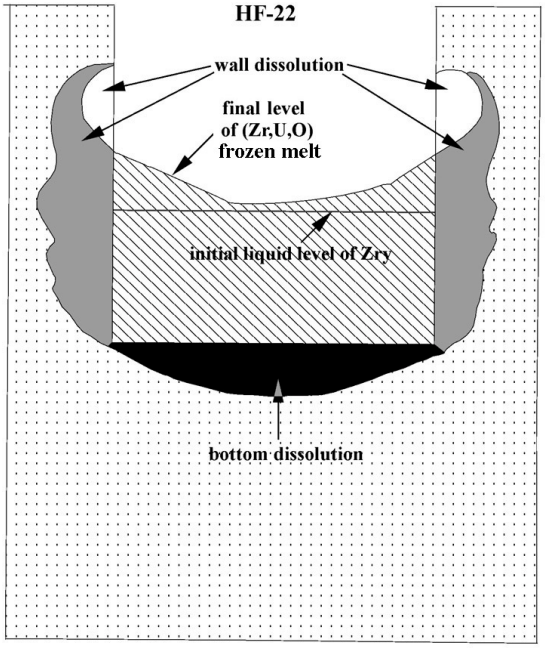

Fig. 5.5:Typical interaction in UO_2 crucible

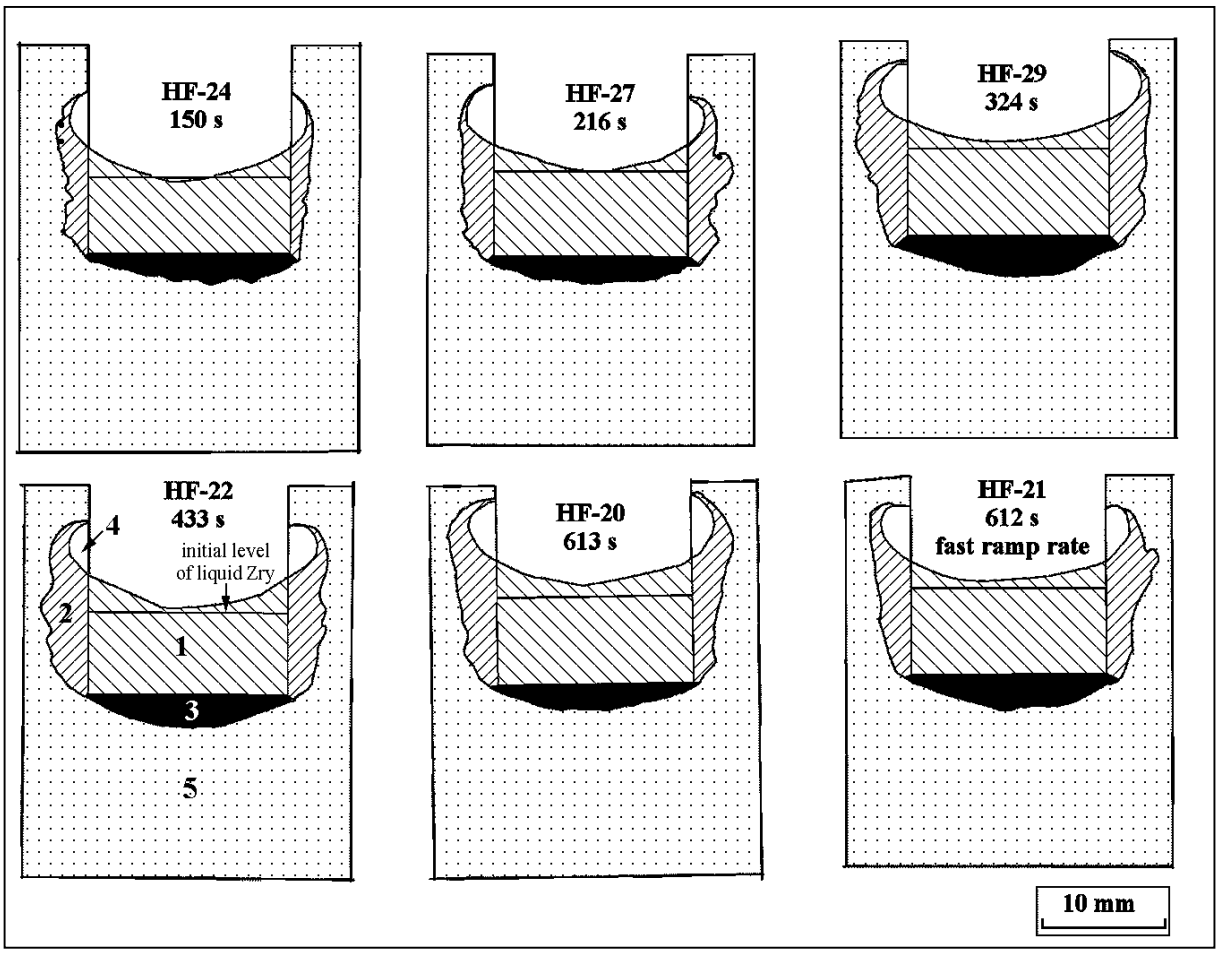

Fig. 5.6: Image analysis of interactions between liquid Zry and solid UO_2 at 2200°C after different reaction times

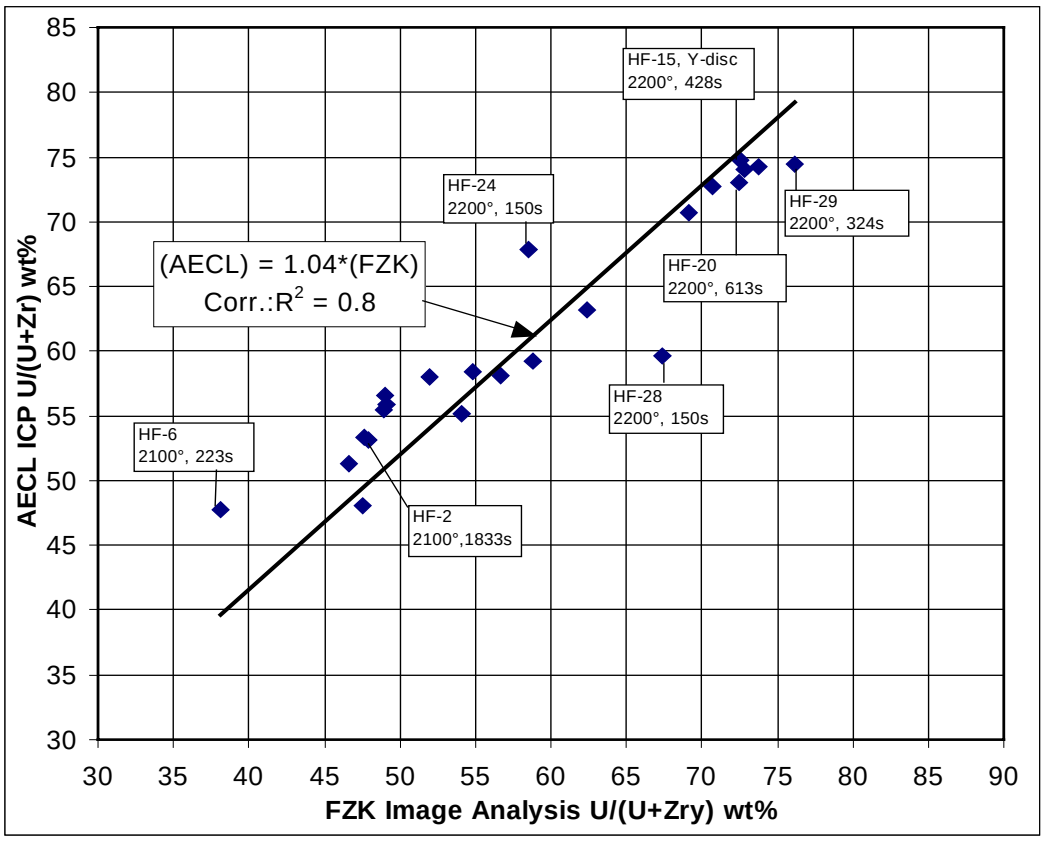

Fig. 5.7: Comparison between the chemical analysis results and the image analysis estimation of uranium content in the melt for UO_2 dissolution tests

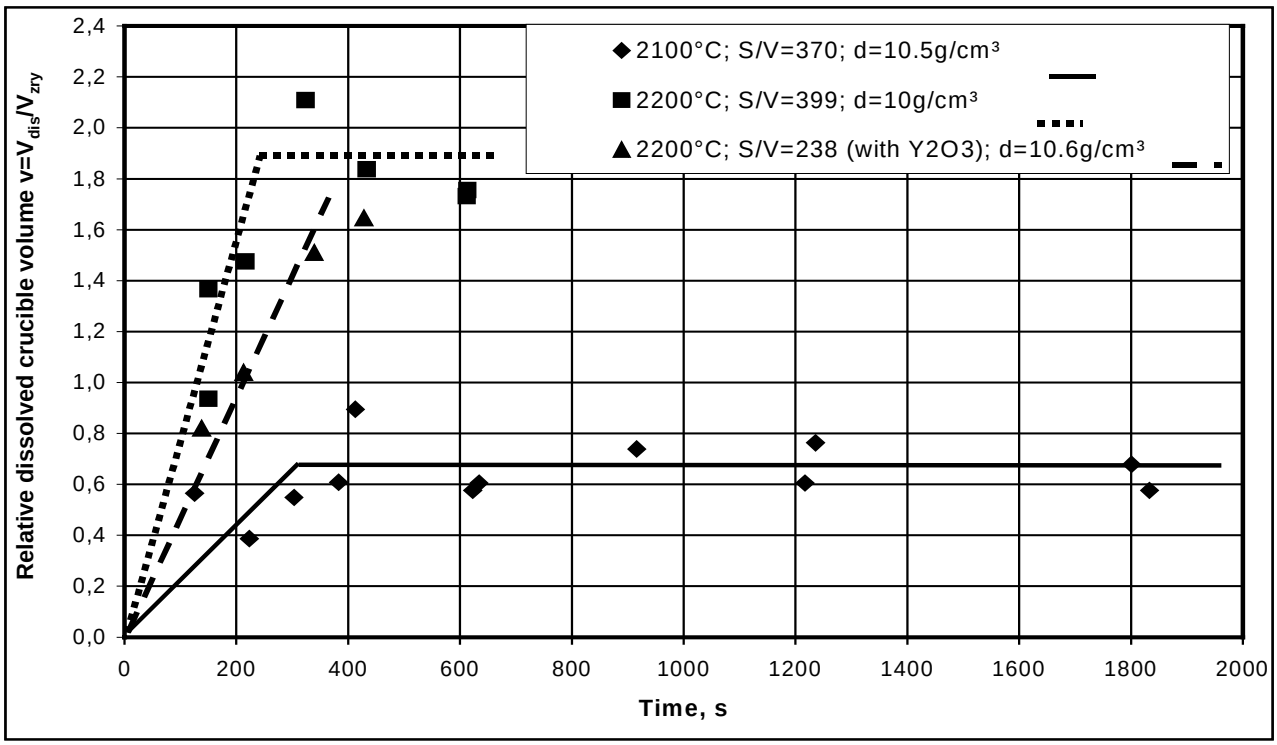

Fig. 5.8: Comparison of the results of dissolution tests.

Data of image analysis

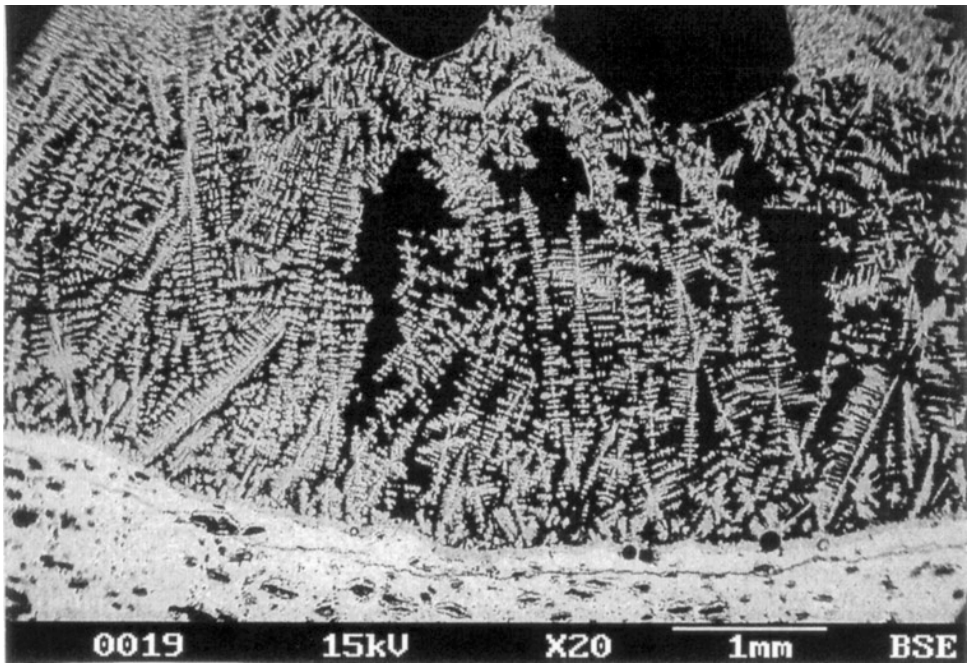

Fig. 5.9: BSE Micrograph of the Bottom Centre Region of the HF-28 (2200^{o}C, 150 s) Specimen, Showing Dendritic Microstructure.

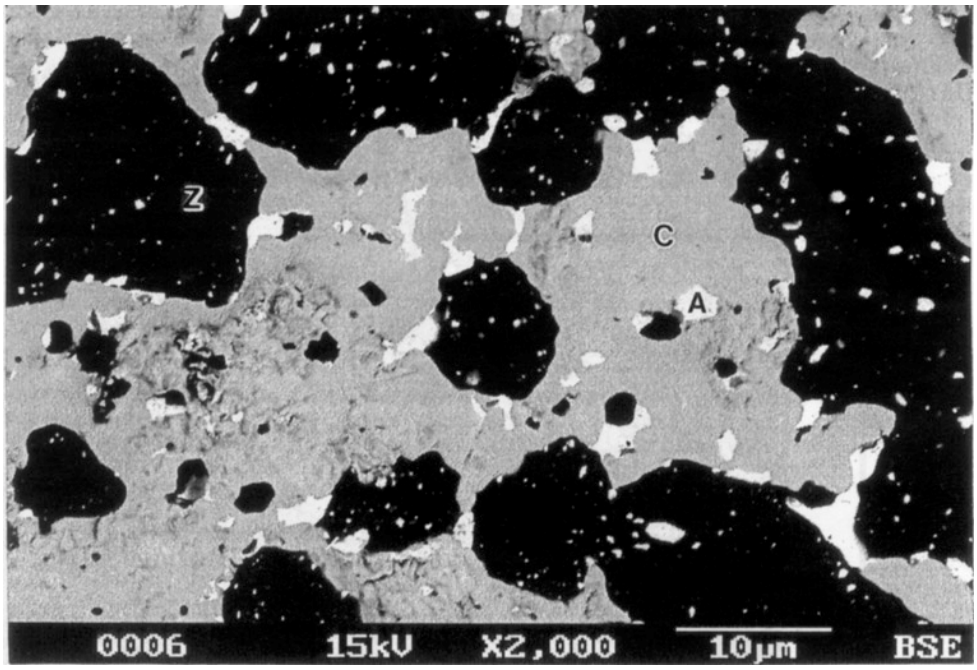

Fig. 5.10: BSE Micrograph of the Top-Right Region of the HF-28 Specimen Showing the Three Phase Types: a $(U,Zr)O_{2-x}$ Ceramic Phase (C); a Zr(O) Alloy Phase (Z); and a U(O) Alloy Phase (A).

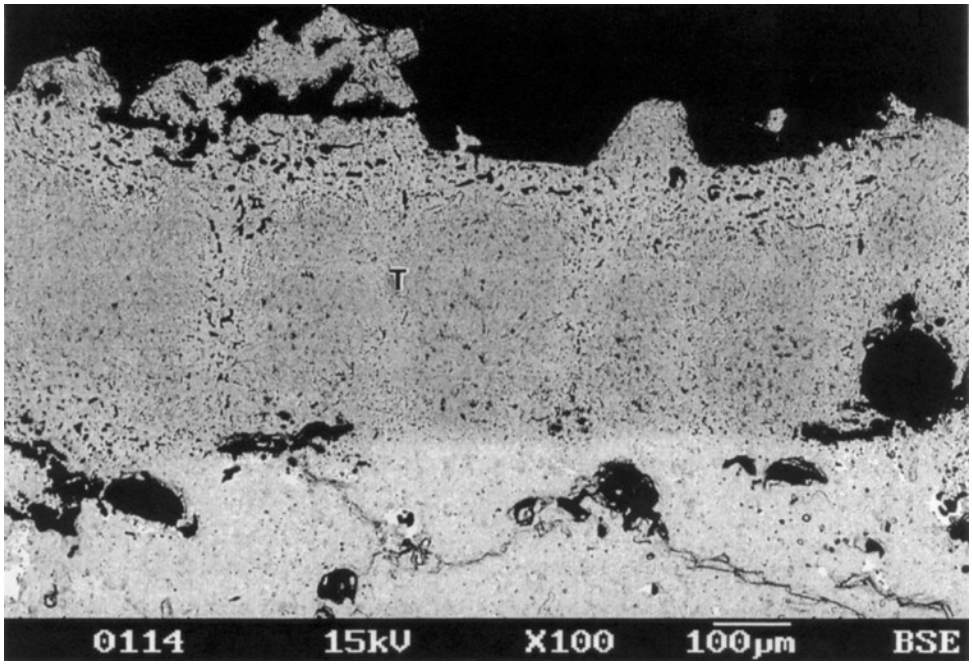

Fig. 5.11: BSE Micrograph Showing a ~400-µm-thick Transition Zone at the Bottom-Centre Region of the HF-21 (2200°C, 612 s) Specimen.

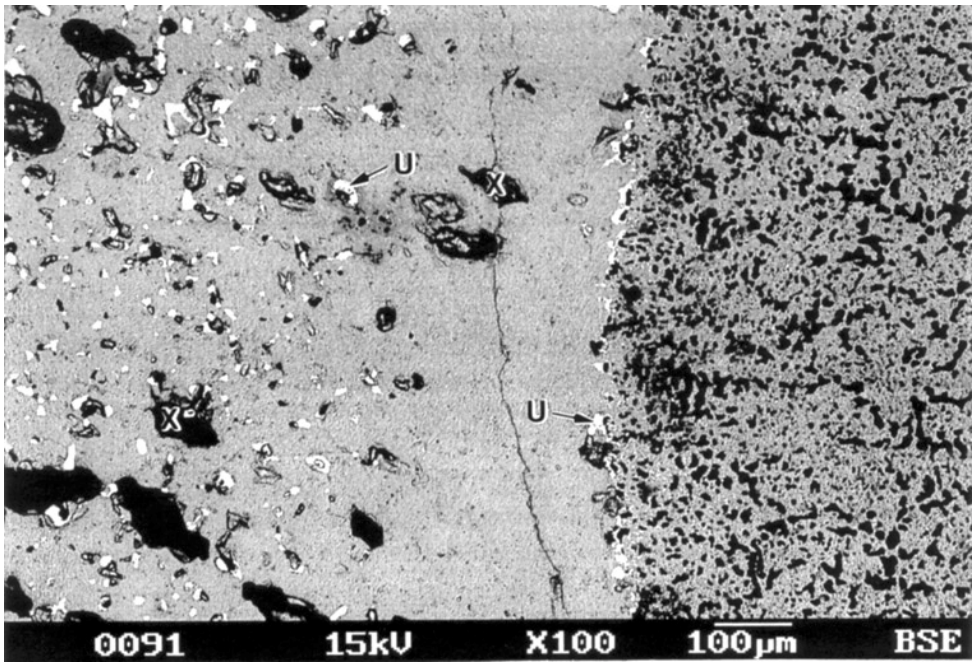

Fig. 5.12: BSE Micrograph of the Crucible/Melt Interface at the HF-22 Left Sidewall, Showing U-Metal Precipitates (U) in the Residual Crucible and at the Melt/Crucible Interface, Separated by a ~300-µm-wide U-Metal-Free Zone.
X = Pores Present in Pre-Test Crucible.

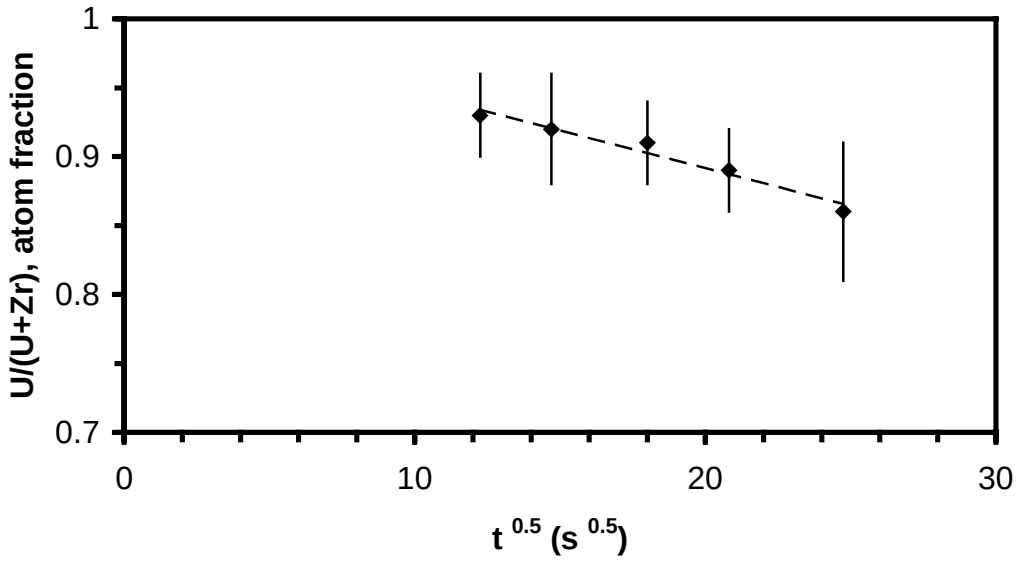

Fig. 5.13: EDX Analyses (Mean ± 2SD) for U/(U + Zr) Atomic Fractions in the $(U,Zr)O_{2-x}$ Ceramic Phase from 2200°C Melts Without Yttria Discs, Plotted against $t^{0.5}$

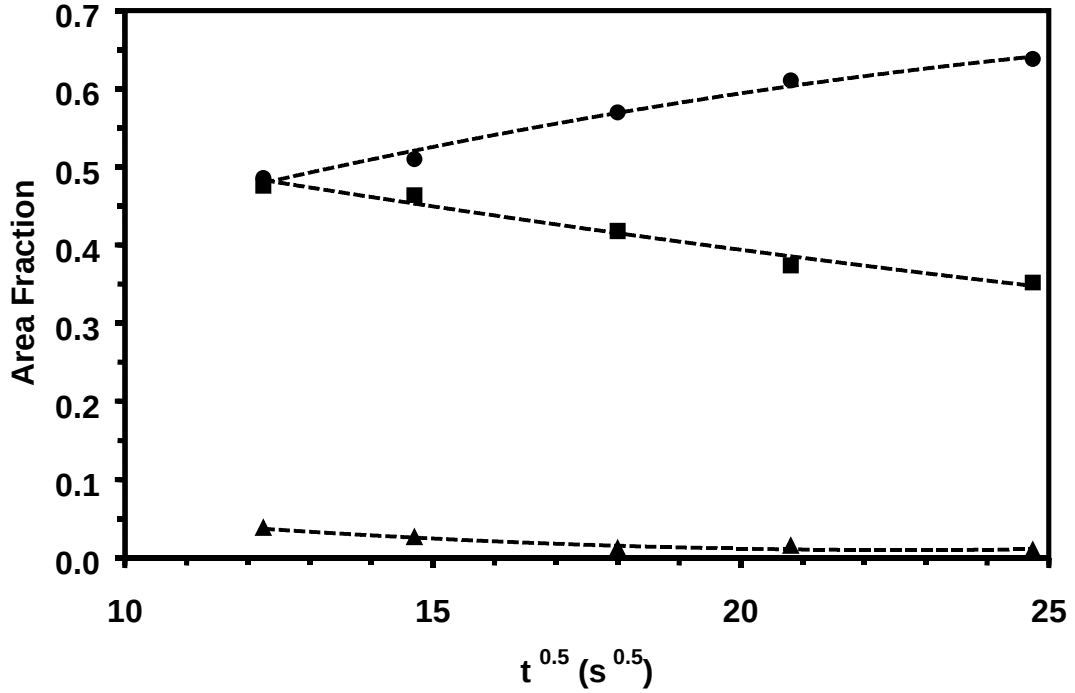

Fig. 5.14: Mean Phase-Area Fractions Versus $t^{0.5}$ for 2200°C Series (No Yttria Discs). Triangles = U(O) Alloy; Circles = $(U,Zr)O_{2-x}$ Ceramic; Squares = Zr(O) Alloy

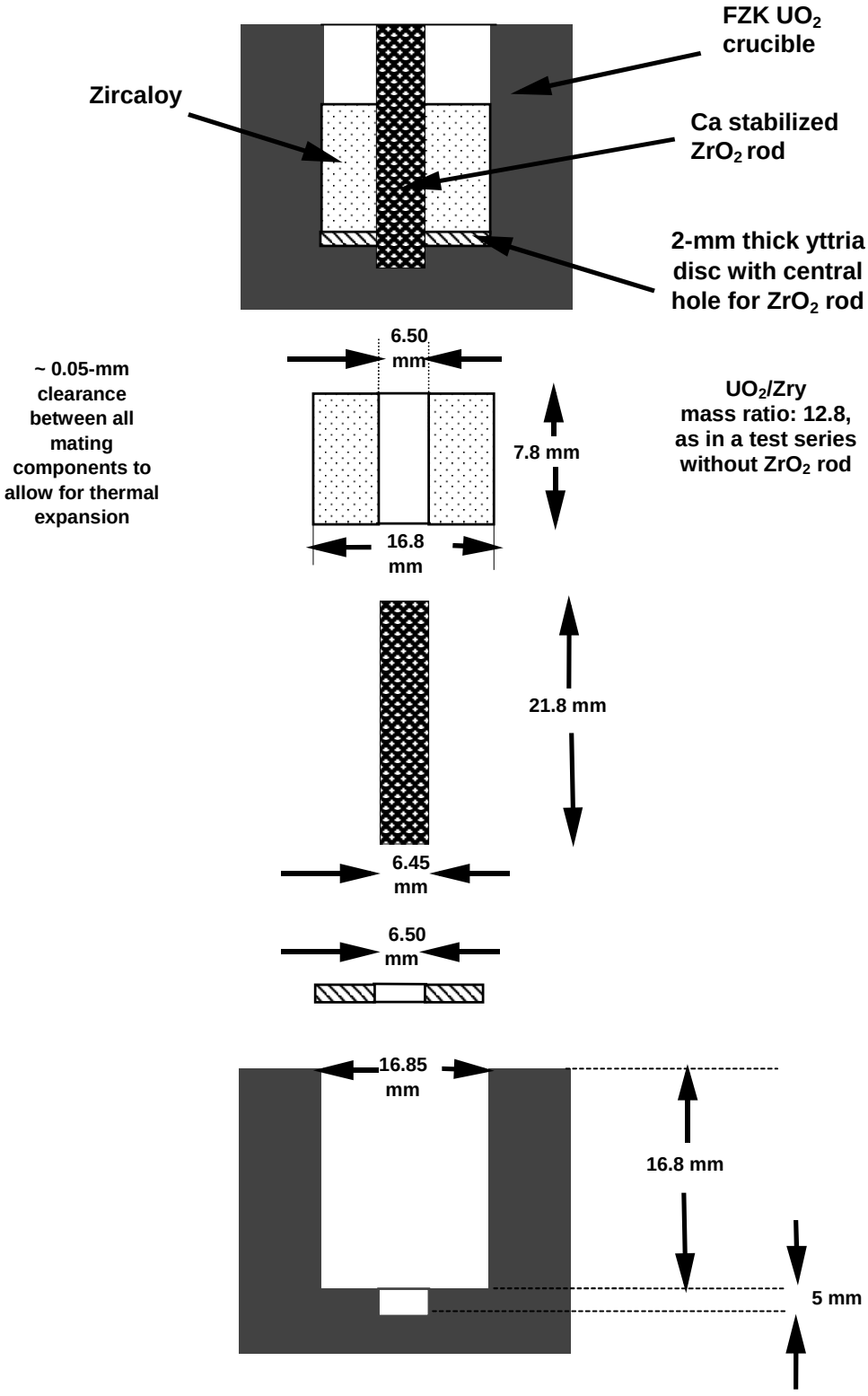

Fig. 6.1: Schematic Diagram of Simultaneous Dissolution Test Configuration.

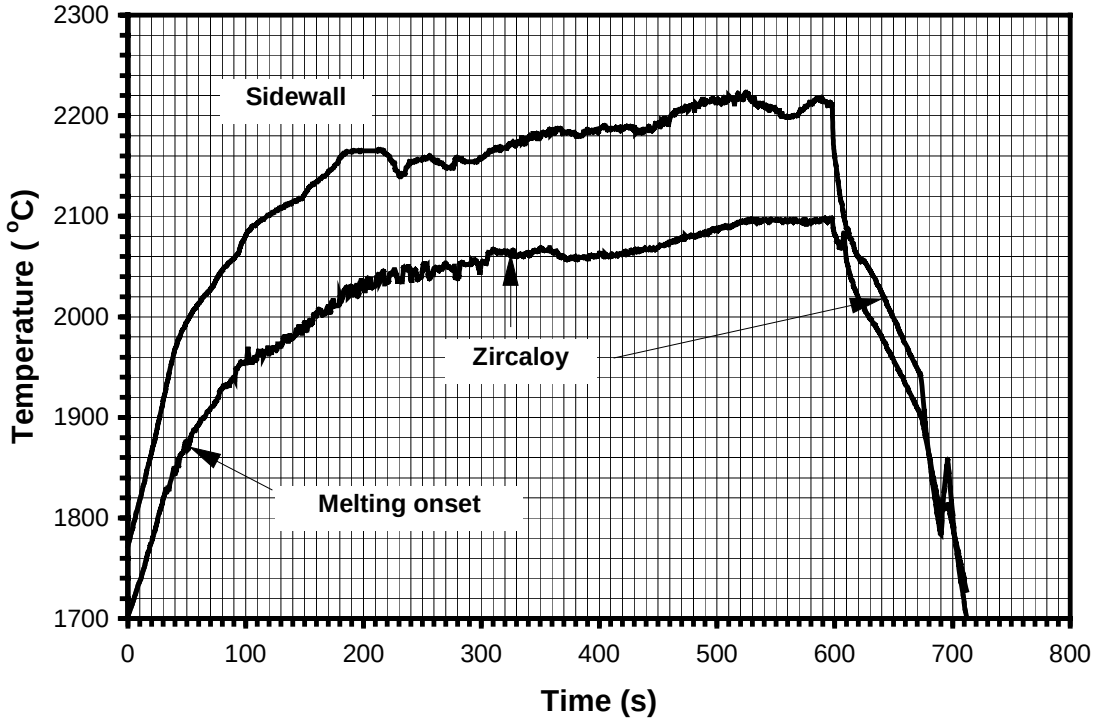

Fig. 6.2: Pyrometer Traces for Test HF-31 (target 500 s at 2100°C).

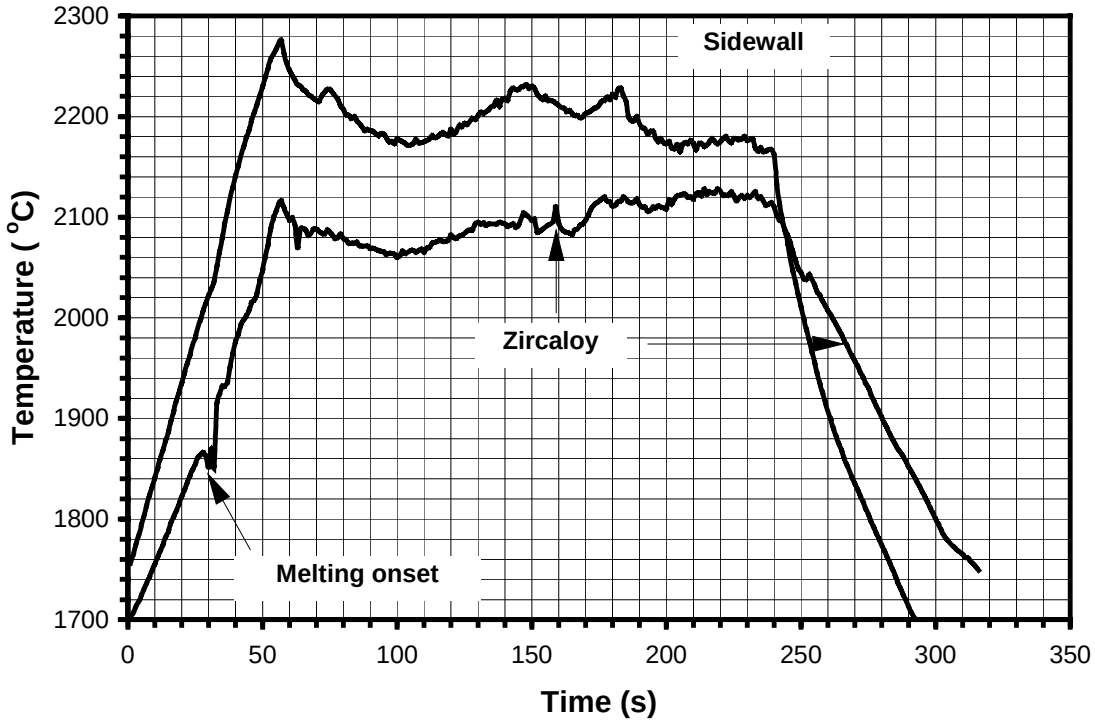

Fig. 6.3: Pyrometer Traces for Test HF-34 (target 200 s at 2100°C).

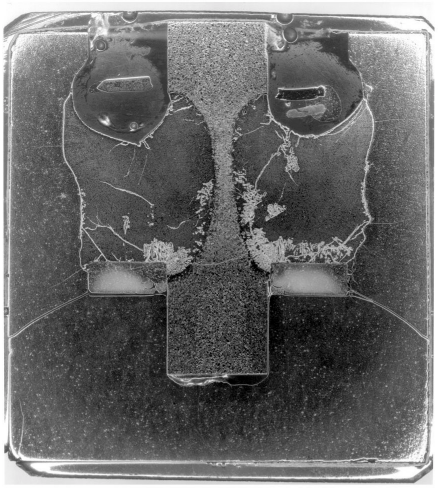

HF-33 (melt duration 108s)

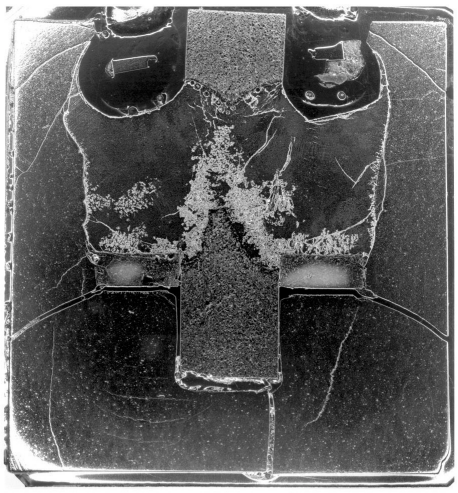

HF-32 (melt duration 206s)

HF-34 (melt duration 216s)

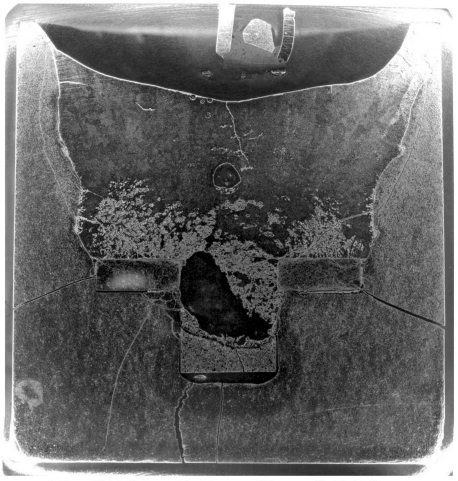

HF-35 (melt duration 315s)

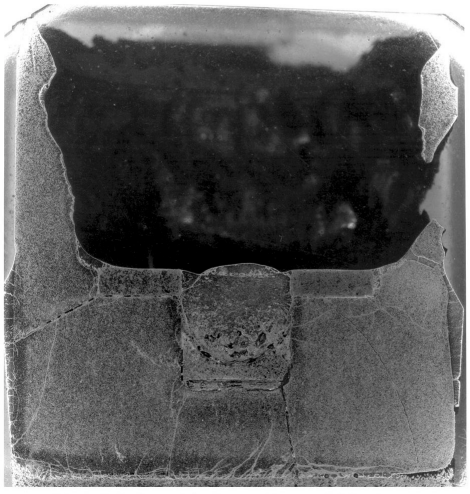

HF-36 (melt duration 423s)

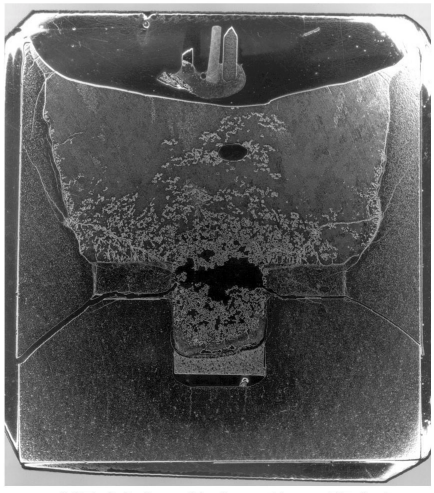

HF-31 (melt duration 554s)

Fig. 6.4.Simultaneous UO_2/ZrO_2 dissolution by molten Zircaloy

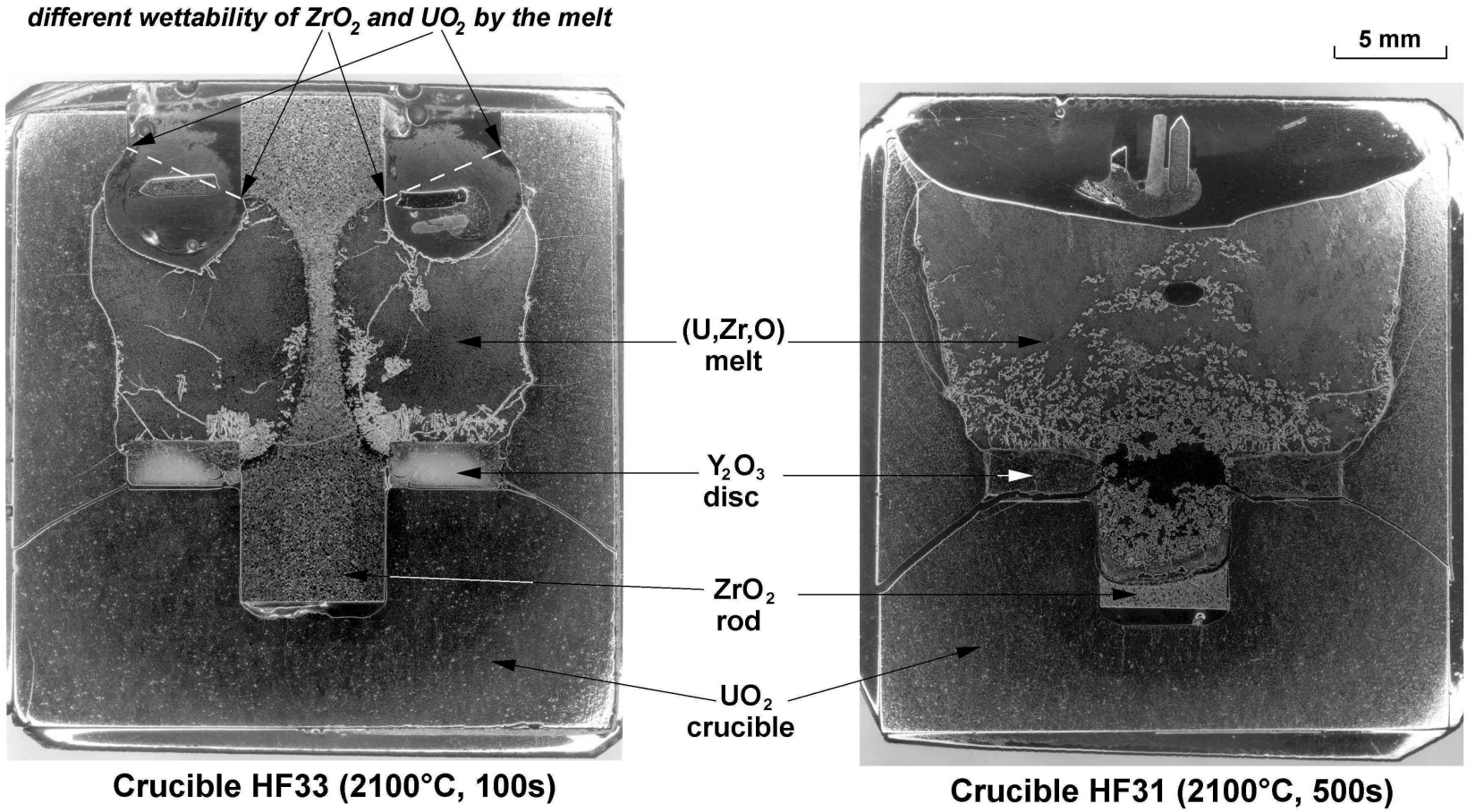

Fig. 6.5. Interaction zones by simultaneous UO_2/ZrO_2 dissolution

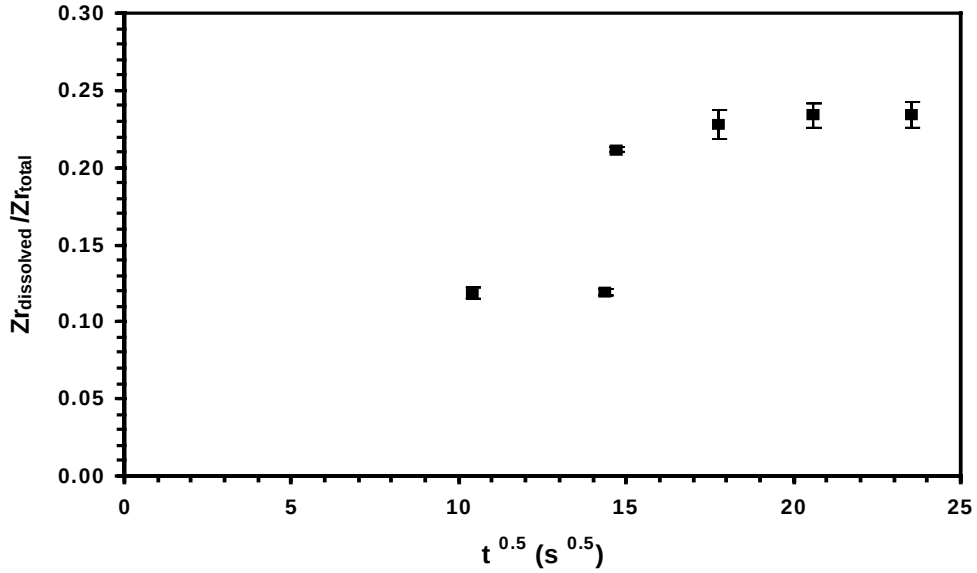

Fig. 6.6: Plot of ICP Data for $Zr_{crucible}/Zr_{total}$ (Wt. Ratio) Versus $Time^{0.5}$ for Specimens from 2100°C Simultaneous Dissolution Tests. Error Bars Represent ± 2SD.

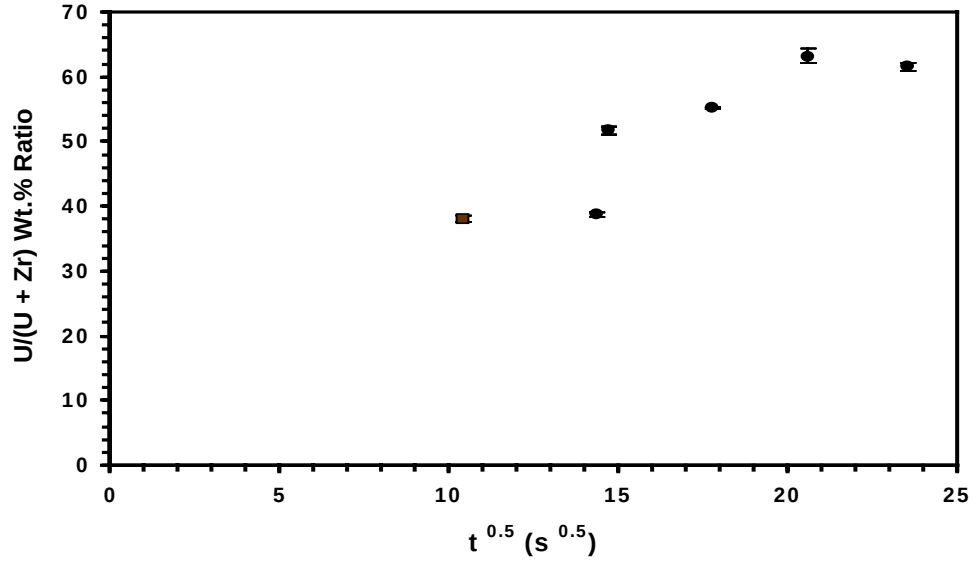

Fig. 6.7: Plot of ICP Data for U/(U+Zr) Wt.% Ratio Versus $Time^{0.5}$ for Specimens from 2100°C Simultaneous Dissolution Tests. Error Bars Represent ± 2SD

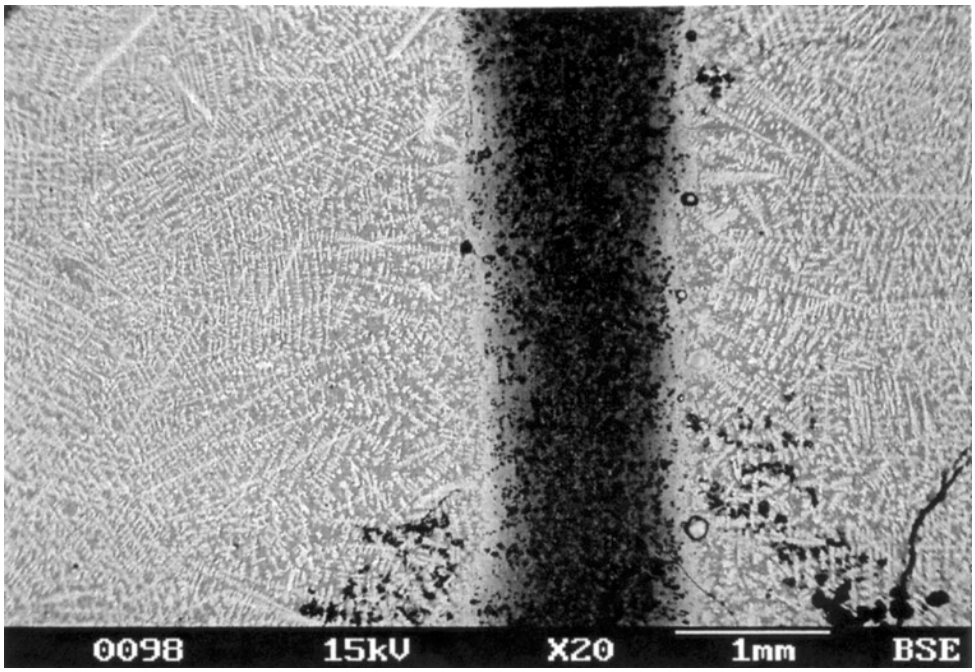

Fig. 6.8: BSE Micrograph of the Dendritic Central Melt Region around the Undissolved Zirconia Rod in the HF-33 Specimen

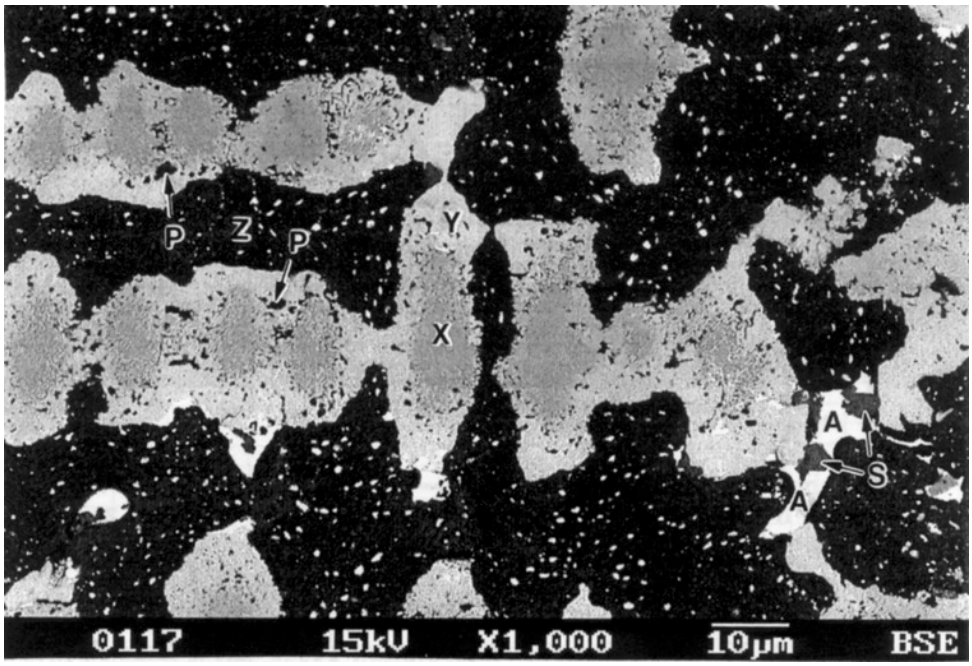

Fig. 6.9: BSE Micrograph of the Bottom Left Region of the HF-32 Specimen Showing the Following Phases: X = Zr-rich Inner Ceramic Zone; Y = Outer U-rich Ceramic Zone; Z = Zr(O) Alloy Matrix; A = U(O) Alloy Regions; P = Inclusions of Zr(O) Material in the Ceramic Phases; S = Zr-Sn-O Phase

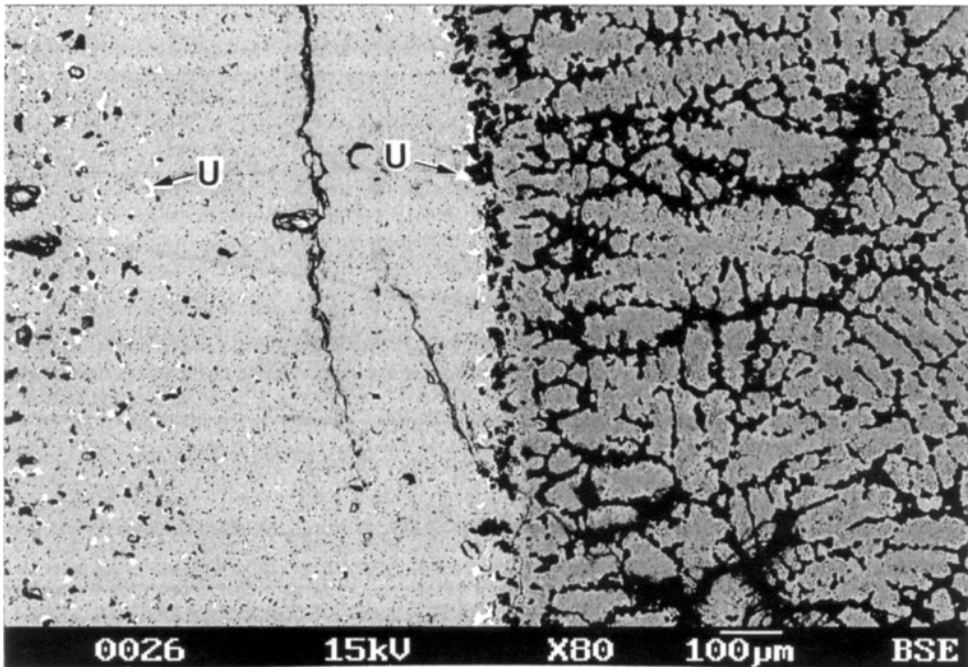

Fig. 6.10: BSE Micrograph of the Crucible/Melt Interface at the Left Sidewall of the HF-31 Specimen, Showing U-Metal Precipitates (U) in the Residual Crucible, a ~450-µm-wide U-Metal-Free Zone and U-Metal Precipitates at the Melt/Crucible Interface.

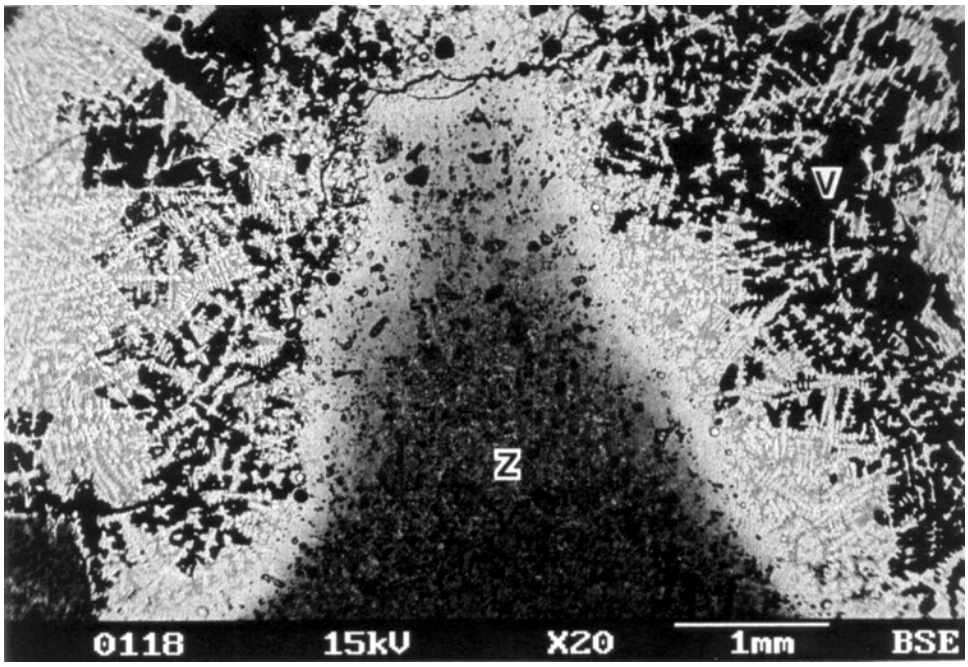

Fig. 6.11: BSE Micrograph of the Bottom Central Region of the HF-32 Specimen just above the Conical Melt/ZrO_2 Interface. Z = ZrO_2, V = Void Regions Formed During Cooling.

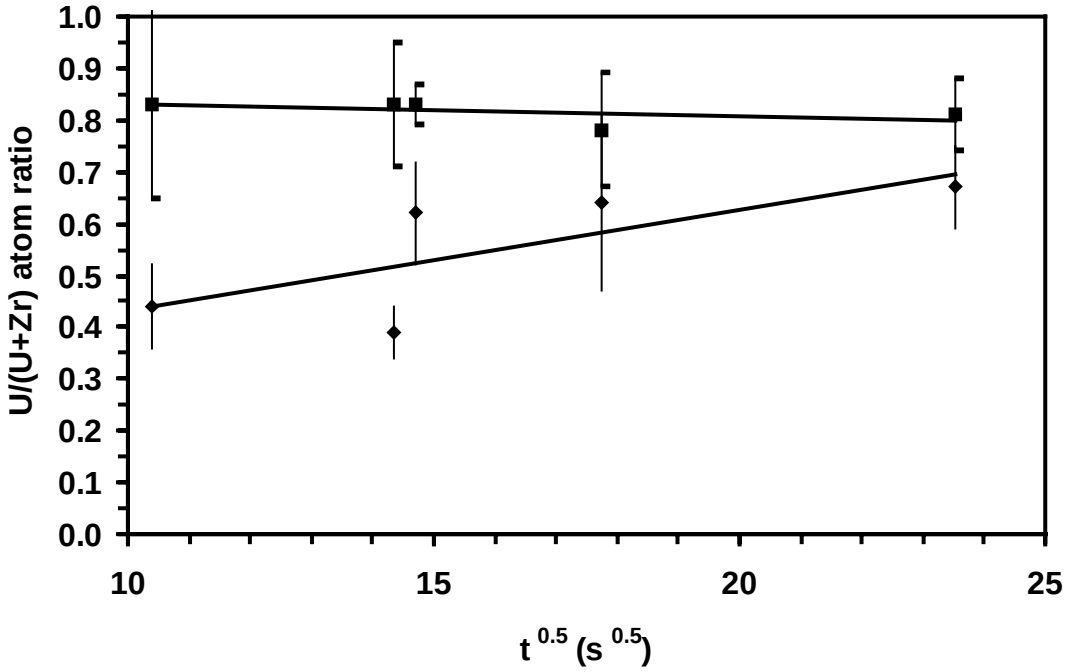

Fig. 6.12: Plot of the EDX Results for the U/(U+Zr) Atom Ratio in the Zoned Ceramic Phases Versus Time$^{0.5}$. Squares = U-Rich Outer Ceramic Zone; Diamonds = Zr-Rich Inner Ceramic Zone. Error Bars are ±2SD.

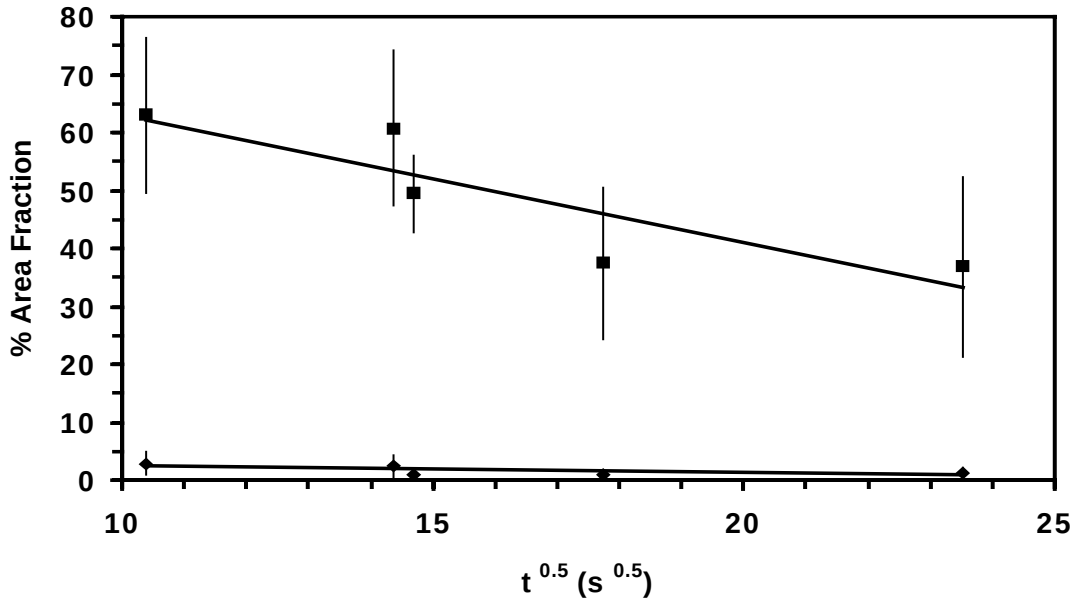

Fig. 6.13: Plot of Mean Area Fractions Versus Time$^{0.5}$ for Specimens from 2100^{o}C Simultaneous Dissolution Tests. Diamonds = U(O) Alloy Phase; Squares = Zr(O) Alloy Phase. Error Bars are ±2SD.

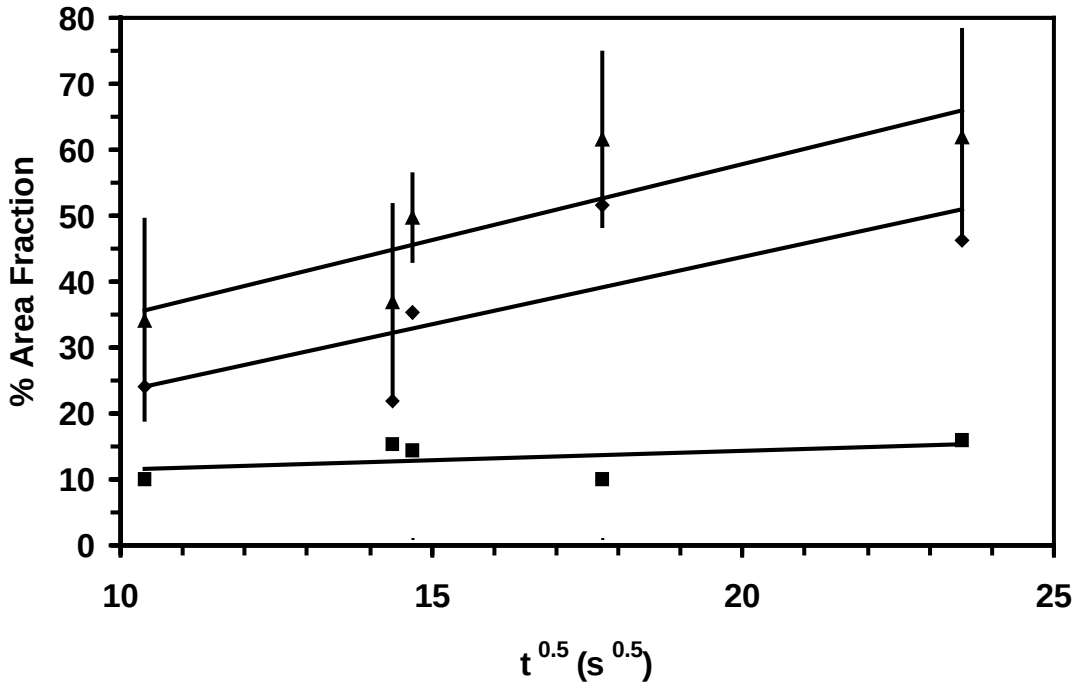

Fig. 6.14: Plot of Mean Area Fractions Versus Time$^{0.5}$ for the Zoned Ceramic Phases in Specimens from 2100^{o}C Simultaneous Dissolution Tests. Diamonds = U-rich Outer Ceramic Zone; Squares = Zr-rich Inner Ceramic Zone. Triangles = Total (i.e., Inner + Outer Zones) Ceramic Phase, with ±2SD Error Bars Shown.

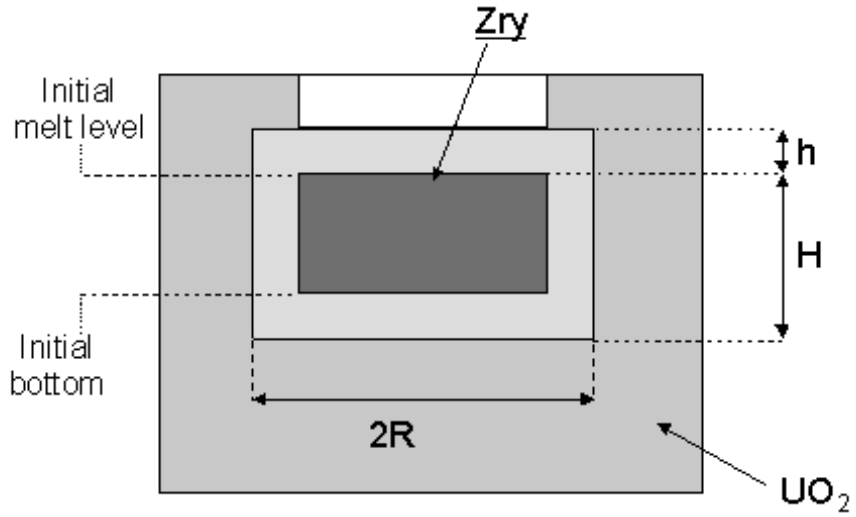

Fig. 7.1: Linear dimensions of the melt in the UO_2 crucible at different moments (schematic)

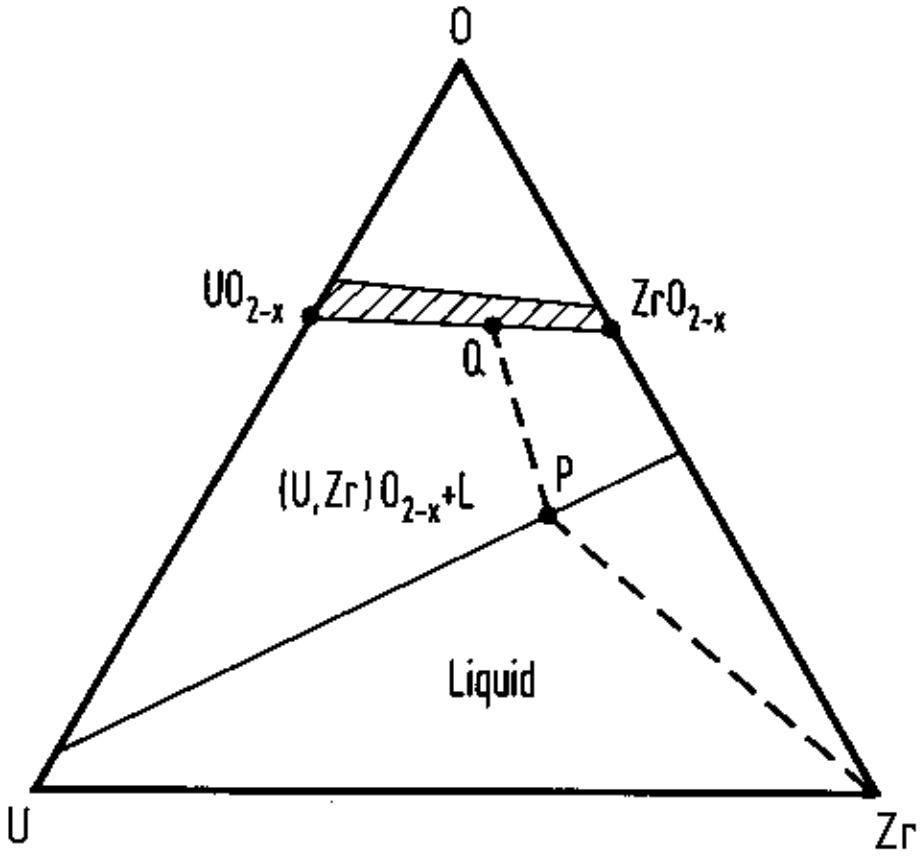

Fig. 7.2: Schematic isothermal section of the U-Zr-O system at 2000°C

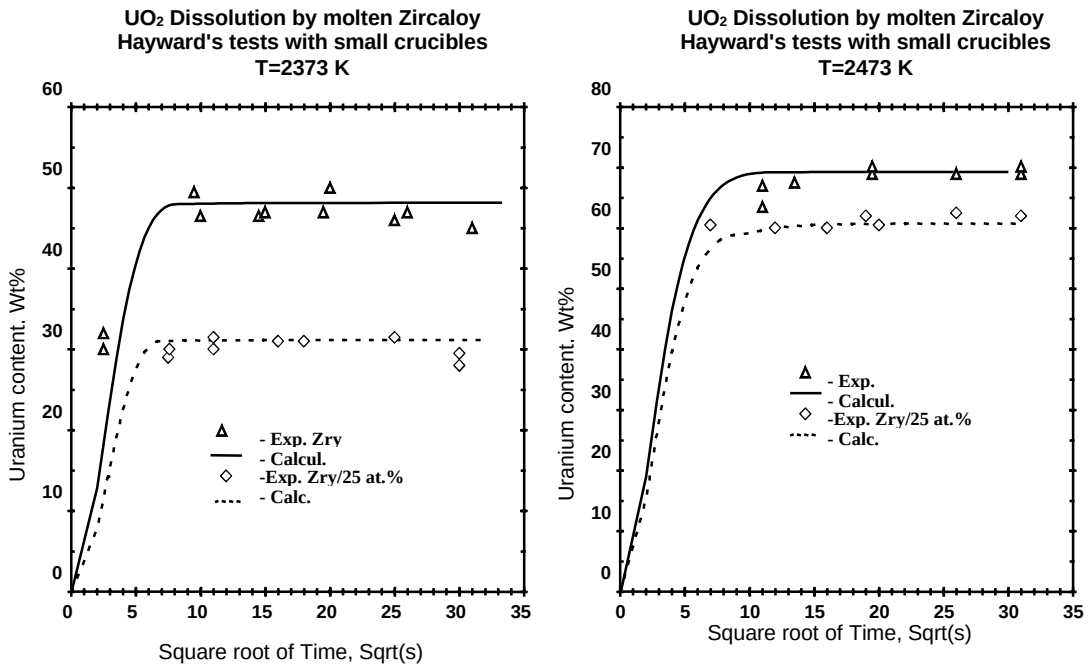

Fig. 7.3: Uranium weight content in the melt in the first, saturation stage in the two tests at 2373 K and 2473 K with pure and pre-oxidised Zry charges

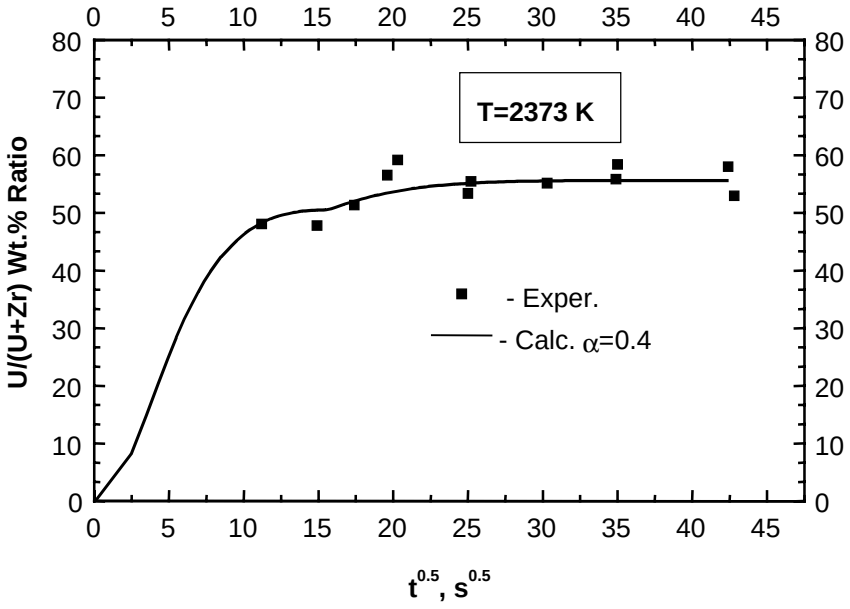

Fig. 7.4: Time evolution of uranium weight content in the melt at T=2373 K (tests without bottom isolation)

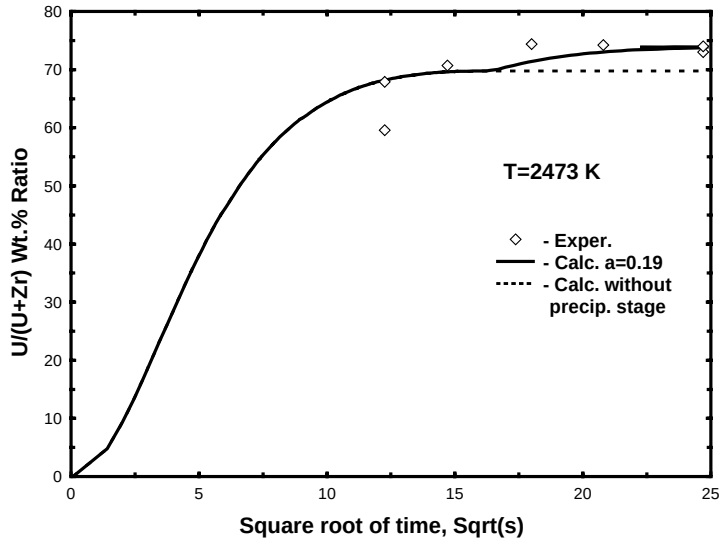

(a)

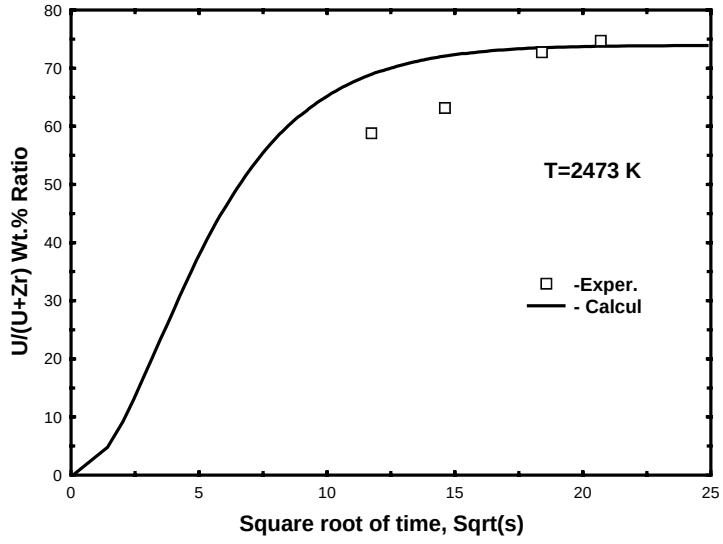

(b)

Fig. 7.5: Time evolution of uranium weight content in the melt at T=2473 K (tests without (a) and with (b) bottom isolation)

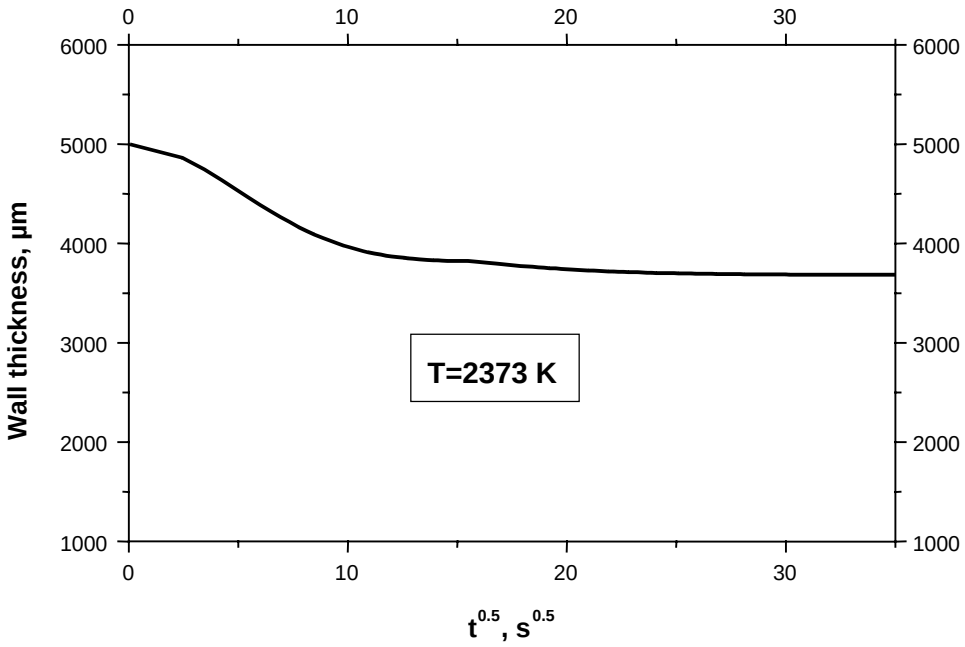

(a)

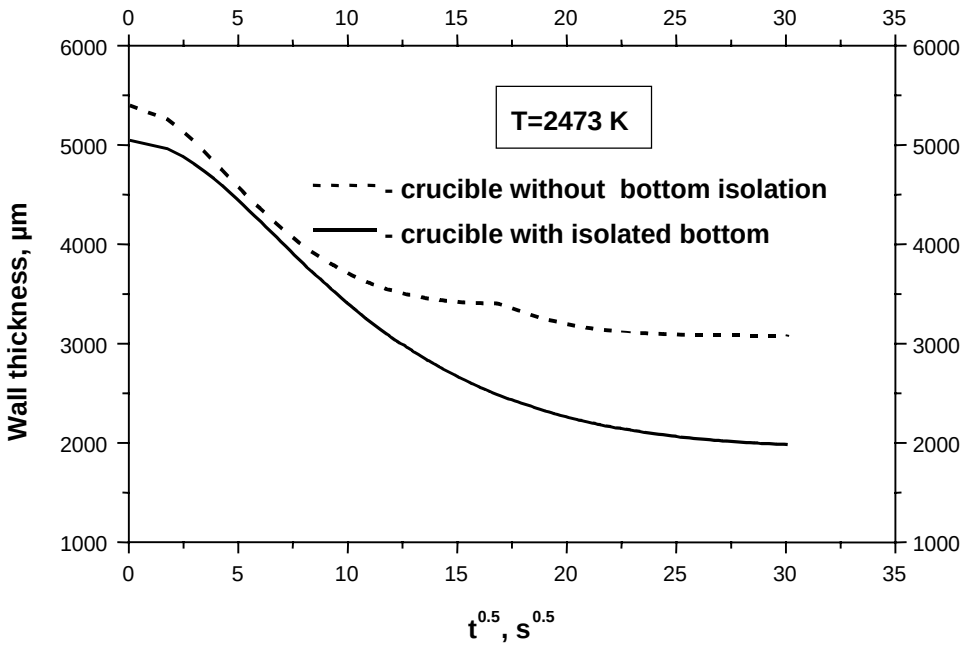

(b)

Fig. 7.6: Time evolution of crucible wall thickness at (a)T=2373 K and (b) T=2473 K (tests with and without bottom isolation)

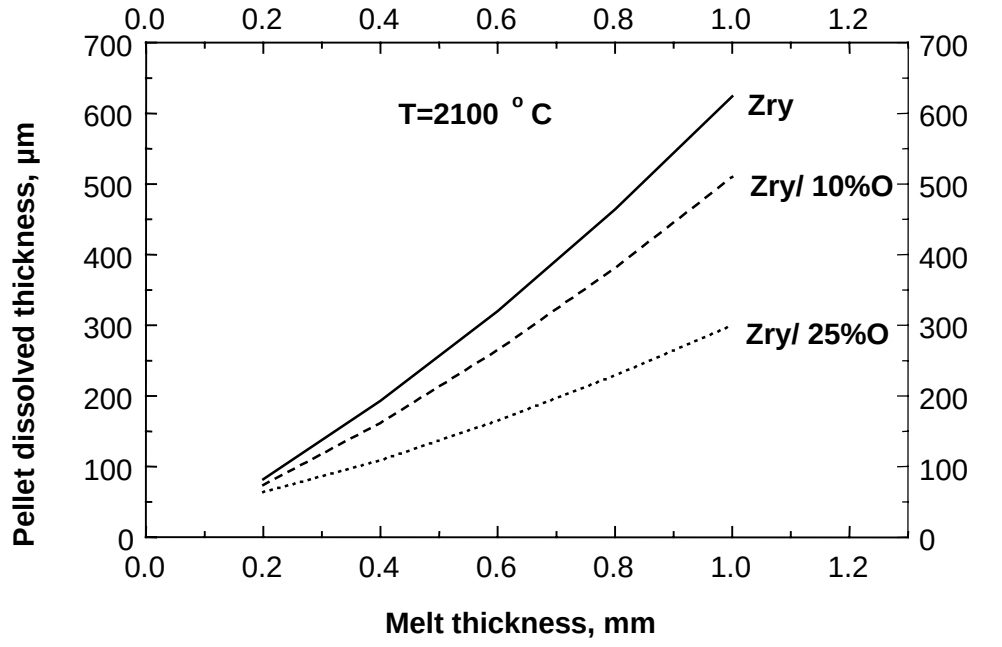

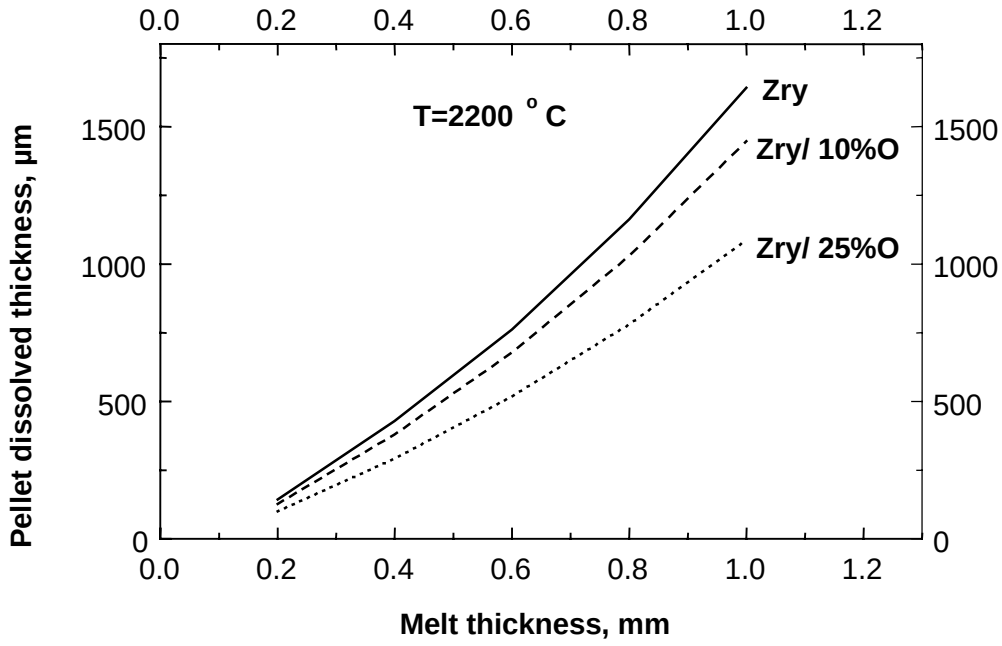

Fig. 7.7: Application of the model to the fuel rod configuration: dependence of the fuel pellet dissolved thickness on the melt thickness at various oxygen contents in the melt

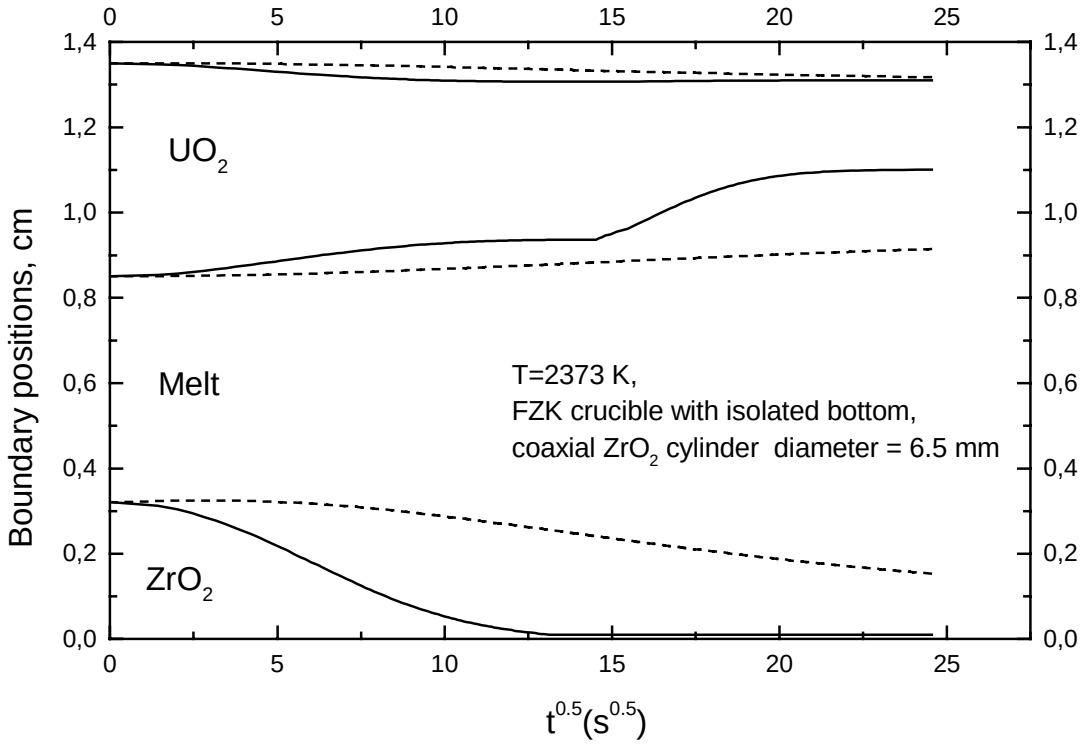

Fig. 8.1: Simulations of the AECL/FZK scoping tests on simultaneous UO_2 and ZrO_2 dissolution by molten Zry: evolution of the interaction layers.

Dotted lines correspond to the low oxygen mass transfer coefficient in the melt (10^{-3} cm/s), typical for the ZrO_2 crucible dissolution tests;

Solid lines correspond to the high oxygen mass transfer coefficient (10^{-2} cm/s), typical for the UO_2 crucible dissolution tests.

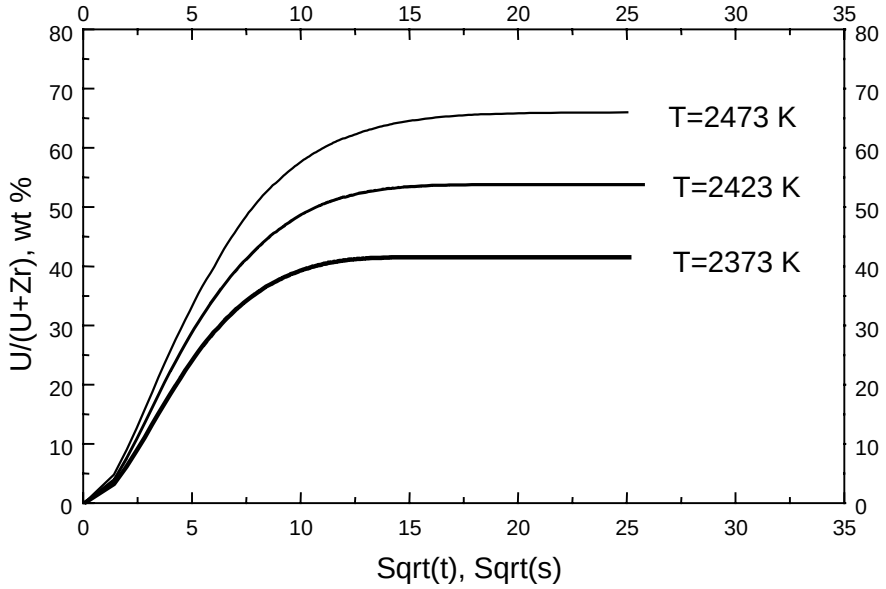

Fig. 8.2: Calculation of the saturation limit of the uranium melt content attained during the first, saturation stage at three different temperatures under conditions of the AECL/FZK scoping tests on simultaneous UO_2 and ZrO_2 dissolution by molten Zry

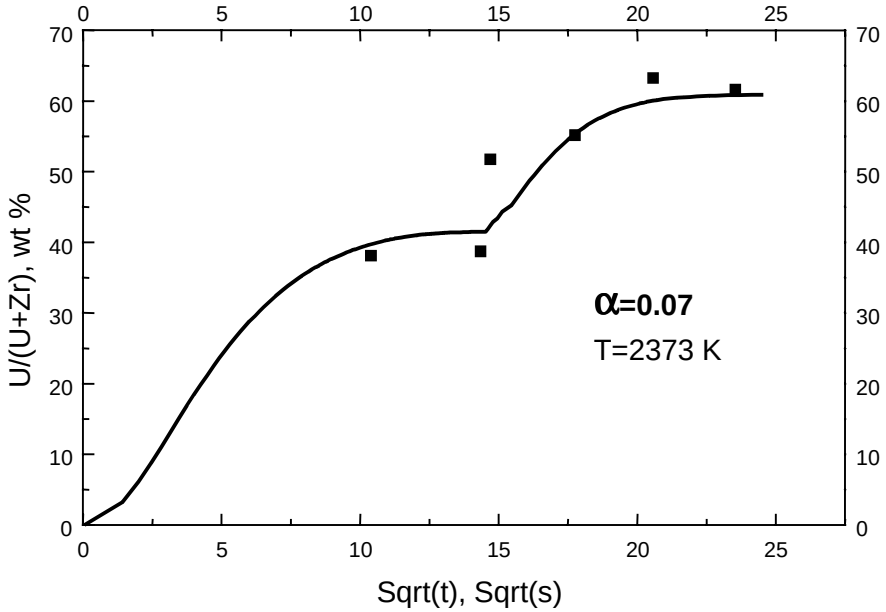

Fig. 8.3: Simulations of the AECL/FZK scoping tests on simultaneous UO_2 and ZrO_2 dissolution by molten Zry: evolution of the uranium content in the melt during the two periods: saturation (up to ≈ 200 s) and precipitation (up to ≈400 s).

The model parameter α determines the U/Zr ratio in the ceramic $(U_{1-\alpha},Zr_{\alpha})O_{2-x}$ precipitates (formed at temperature).